

# Study of Open Charm Production in p+p Collisions at $\sqrt{s} = 200$ GeV

A Dissertation Presented

by

Sergey Butsyk

to

The Graduate School

in Partial Fulfillment of the Requirements

for the Degree of

Doctor of Philosophy

in

Physics

Stony Brook University

May 2005

Copyright © by  
Sergey Butsyk  
2005

Stony Brook University

The Graduate School

Sergey Butsyk

We, the dissertation committee for the above candidate for the Doctor of Philosophy degree, hereby recommend acceptance of this dissertation.

---

Thomas Hemmick (Advisor)

Professor, Department of Physics and Astronomy

---

Edward Shuryak (Chair)

Professor, Department of Astronomy and Physics

---

Michael Marx

Professor, Department of Astronomy and Physics

---

Ralf Averbeck

Assistant Professor, Department of Astronomy and Physics

---

Yasuyuki Akiba

Senior Scientist, RIKEN Institution

This dissertation is accepted by the Graduate School.

---

Graduate School

**Abstract of the Dissertation**  
**Study of Open Charm Production in p+p**  
**Collisions at  $\sqrt{s} = 200$  GeV**

by

Sergey Butsyk

Doctor of Philosophy

in

Physics

Stony Brook University

2005

The PHENIX experiment at the Relativistic Heavy Ion Collider (RHIC) with its unique electron identification system enables us to perform high precision measurements of electron yields. By measuring electron production at high transverse momentum, we can disentangle the contribution of electrons originating from semi-leptonic decays of heavy quarks (charm or bottom) from the less interesting “photonic” decay modes of light mesons.  $D/B$  mesons carry single heavy valence quarks and are usually referred to as “Open Charm” and “Open Bottom” particles, differentiating them from Closed Flavor particles such as  $J/\psi$  and  $Y$  mesons. Due to the large mass of the heavy quarks, their production mechanisms can be adequately explained by perturbative QCD (pQCD) theory.

This dissertation presents the measurement of electrons from heavy flavor decays in proton + proton collisions at RHIC at collision energy  $\sqrt{s} = 200$  GeV over a wide range of transverse moment ( $0.4 < p_T < 5$  GeV/c). Two independent analysis techniques of signal extraction were performed. The “Cocktail” subtraction is



based on the calculation and subtraction of the expected “photon - related” electron background based upon measured yields of light mesons. The “Converter” subtraction is based upon a direct measurement of photon yields achieved introducing additional material in the PHENIX acceptance and deducing the photon abundance by measuring the increase in electron yield. This is the first measurement of the Open Charm crosssection at this collision energy and it is an important baseline measurement for comparison with nucleus + nucleus collisions. The modification of Open Charm production in heavy ion collisions compared to the presented  $p + p$  result can be used to study the final state interaction of the heavy quarks with hot dense matter inside the collisions. The results of the Open Charm measurements are compared to current pQCD predictions both in Leading Order (LO)  $O(\alpha_s^2)$  and Next-to-Leading Order (NLO)  $O(\alpha_s^3)$ . The final result for the total Open Charm crosssection is  $\sigma_{c\bar{c}} = (0.920 \pm 0.148(stat) \pm 0.524(sys))$  mb, in good agreement with the published STAR experiment measurements of Open Charm crosssection in  $d + Au$  colliding system.

To my mom, my dad and Julia

# Contents

|                                       |             |
|---------------------------------------|-------------|
| <b>List of Figures</b>                | <b>xvii</b> |
| <b>List of Tables</b>                 | <b>xix</b>  |
| <b>Acknowledgements</b>               | <b>xix</b>  |
| <b>1 Introduction</b>                 | <b>1</b>    |
| <b>2 Theory</b>                       | <b>4</b>    |
| 2.1 Quantum Chromodynamics            | 4           |
| 2.2 Renormalization of QCD            | 7           |
| 2.3 Heavy quark production in QCD     | 10          |
| 2.4 Hard scattering processes         | 10          |
| 2.5 $Q\bar{Q}$ fragmentation          | 13          |
| 2.6 Heavy Flavor meson decay          | 15          |
| <b>3 PHENIX Experiment</b>            | <b>17</b>   |
| 3.1 PHENIX Detector                   | 17          |
| 3.2 Global Detectors                  | 20          |
| 3.2.1 Beam-Beam Counter-BBC           | 20          |
| 3.2.2 Zero Degree Calorimeter         | 22          |
| 3.3 Central Arm Detectors             | 23          |
| 3.3.1 Central Magnet                  | 23          |
| 3.3.2 Drift Chamber                   | 26          |
| 3.3.3 Pad Chambers                    | 40          |
| 3.3.4 Ring Imaging Cerenkov Detectors | 42          |
| 3.3.5 Electromagnetic Calorimeters    | 45          |

|          |  |            |
|----------|--|------------|
| <b>4</b> | <b>Data Analysis</b>   | <b>48</b>  |
| 4.1      | Quality Assurance and run selection  | 48         |
| 4.1.1    | Acceptance cuts  | 49         |
| 4.1.2    | Event selection  | 52         |
| 4.1.3    | Run selection and event counting   | 54         |
| 4.2      | Electron identification cuts   | 56         |
| 4.2.1    | n0 cut optimization  | 56         |
| 4.2.2    | EMC matching cut optimization  | 57         |
| 4.2.3    | $E/p$ cut parametrization  | 58         |
| 4.3      | Inclusive electron invariant crosssection  | 61         |
| 4.3.1    | "Raw" electron yield   | 61         |
| 4.3.2    | ERT trigger efficiency   | 63         |
| 4.3.3    | Hadronic background  | 65         |
| 4.3.4    | $\delta$ -electron background  | 67         |
| 4.3.5    | Acceptance Correction function   | 70         |
| 4.3.6    | BBC Trigger Bias   | 77         |
| 4.3.7    | Combining statistics   | 81         |
| 4.3.8    | Bin width corrections  | 86         |
| 4.4      | Cocktail Estimation of the "Photonic" Electron Component                           | 88         |
| 4.4.1    | Cocktail input   | 88         |
| 4.4.2    | Final Electron Cocktail  | 96         |
| 4.5      | "Non-photonic" Electron Crosssection   | 97         |
| 4.6      | Converter Subtraction Method   | 99         |
| 4.6.1    | Converter and Non-converter run group acceptance comparison                        | 100        |
| 4.6.2    | Inclusive electron crosssection in Converter run                                   | 101        |
| 4.6.3    | Calculation of $R$   | 102        |
| 4.6.4    | "Photonic" and "Non-photonic" electron component from Converter subtraction method | 103        |
| 4.7      | Systematic error analysis  | 108        |
| 4.7.1    | Systematic error of the inclusive crosssection                                     | 108        |
| 4.7.2    | Systematic error of the Cocktail   | 120        |
| 4.7.3    | Systematic error of the subtracted crosssection                                    | 123        |
| <b>5</b> | <b>Results</b>   | <b>124</b> |
| 5.1      | Comparison with Theory   | 124        |
| 5.1.1    | Comparison with PYTHIA   | 125        |
| 5.1.2    | Comparison with NLO pQCD   | 130        |
| 5.2      | Estimation of total Open Charm crosssection  | 136        |

|          |                |            |
|----------|----------------|------------|
| <b>6</b> | <b>Summary</b> | <b>143</b> |
|----------|----------------|------------|

# List of Figures

|      |  |    |
|------|--|----|
| 1.1  | Invariant crosssection for "Non-photonic" electrons at $\sqrt{s} = 130$ GeV at PHENIX [50]. . . . .  | 3  |
| 1.2  | Mass spectrum of $K\pi$ pairs in $d + Au$ collisions with clear $D^0$ peak [72] . . . . .  | 3  |
| 2.1  | Deep Inelastic $e^-p \rightarrow e^-X$ scattering. [1] . . . . .   | 5  |
| 2.2  | Tree-level Feynman diagrams contributing to $q\bar{q} \rightarrow gg$ . [1] . . .  | 6  |
| 2.3  | Photon self-energy contribution to $e^-e^-$ scattering. [1] . . . .  | 7  |
| 2.4  | Feynman diagrams contributing to the renormalization of the strong coupling. [1] . . . . .   | 8  |
| 2.5  | Measurements of $\alpha_s$ as a function of energy scale [15]. . . . .   | 9  |
| 2.6  | LO and most important NLO heavy quark production diagrams. LO - a) "gluon fusion" b) "quark-antiquark annihilation" NLO - c) Pair creation with gluon emission in output channel d) "flavor excitation" e) "gluon splitting" f) "gluon splitting but of "flavor excitation" character [18] . . . . .                 | 11 |
| 2.7  | Comparison of the photon and direct- $\gamma$ measured by $E706$ experiment in $p + Be$ collisions at $\sqrt{s} = 38.8$ GeV with pQCD predictions for different values of $\langle k_T \rangle$ smearing (left panel). Comparison of gluon structure function for most recent PDF sets (right panel). [26] . . . . . | 13 |
| 2.8  | Momenta of measured B meson fragmentation function compared with pQCD NLL calculations with different assumptions for $D(z)$ . The solid line is one-parameter fit to the second momentum [34]. . . . .  | 15 |
| 2.9  | Semi-leptonic decay diagrams for Open Charm and Open Bottom meson semi-leptonic decay. . . . .   | 16 |
| 2.10 | Semi-leptonic decay rate as a function of $2E_e/M_Q$ for Open Charm (left panel) and Open Bottom (right panel) [36]. . . . .   | 16 |
| 3.1  | Layout for PHENIX Experiment. . . . .  | 19 |
| 3.2  | Picture of BBC barrel before the installation. . . . .   | 21 |

|      |   |    |
|------|---|----|
| 3.3  | Structural drawing of one BBC (beam view). Each box corresponds to one PMT. . . . .   | 21 |
| 3.4  | Schematic view of ZDC detector. A) Top view of interaction region. B) Projected proton and neutron deflection area at ZDC placement plane. . . . .  | 22 |
| 3.5  | Central Magnet during assembly (Izhorskyi plant, St. Petersburg, Russia). . . . .   | 24 |
| 3.6  | Crossection view of Central Magnet coils and yolk. . . . .  | 24 |
| 3.7  | Magnetic field lines in PHENIX Magnet System. Drift Chamber location is shown by dashed box. . . . .  | 24 |
| 3.8  | Magnetic field strength as function of radius for three different configurations of the magnetic coil polarizations. . . . .  | 25 |
| 3.9  | Schematic drawing of one Drift Chamber Arm. . . . .   | 27 |
| 3.10 | Wire structure of DCH Keystone. . . . .   | 27 |
| 3.11 | Layout of the wire structure of X1 cell. . . . .  | 27 |
| 3.12 | GARFIELD simulation of electric field lines inside X1 cell of the DCH. Marked region display the charge collection zone of each anode wire. Circles represents charge clusters drifting towards the anode wire. . . . . | 29 |
| 3.13 | Drift velocity as a function of electric field. . . . .   | 30 |
| 3.14 | Single wire efficiency as a function of charge per unit length $Q$ . . . . .  | 30 |
| 3.15 | Time distribution for two DCH planes. Left and right edges fitted with error function [42]. . . . .   | 31 |
| 3.16 | Residual distribution as a function of hit width before (left) and after (right) the slewing corrections. . . . .   | 32 |
| 3.17 | Residual as a function of time fitted with linear function. . . . .   | 32 |
| 3.18 | Comparison of $v_{dr}$ for East X1 wires obtained from the data residual slope (circles) and GARFIELD simulation (squares). . . . .   | 32 |
| 3.19 | Distribution of the residual distribution slopes (see Fig. 3.17) for all the DCH wires before and after drift velocity corrections. . . . .   | 32 |
| 3.20 | Determination of $t_0$ from the slope of timing distribution at constant height for one DCH plane. Slope is fitted by Error function. . . . .   | 34 |
| 3.21 | Comparison of plane-by-plane $t_0$ corrections for different DCH arms and different height cut. . . . .   | 34 |
| 3.22 | Residual distribution of the hit to the track for East (left panel) and West (right panel) DCH arm fitted with double-gaussian [42]. . . . .  | 34 |
| 3.23 | Single wire efficiency map for $p + p$ Run02. . . . .   | 36 |

|      |  |    |
|------|--|----|
| 3.24 | Tracking efficiency as a function of single wire efficiency for different requirement on the number of hits in X1 and X2 DCH plane. . . . .  | 37 |
| 3.25 | Single wire efficiency map for $p + p$ Run02. . . . .  | 37 |
| 3.26 | Event display snapshot with track candidates after the initial hit fitting. . . . .  | 39 |
| 3.27 | Event display snapshot with tracks on the final stage of track-finding. Same event as for Fig. 3.26 . . . . .  | 39 |
| 3.28 | Schematic view of PHENIX Pad Chamber set. Several sectors of PC2 and PC3 in the west arm are removed for clarity of the picture. [44]. . . . .   | 41 |
| 3.29 | A cutaway view of the RICH detector [45]. . . . .  | 43 |
| 3.30 | Top view of the RICH and its optics. The tracks of the electrons and the emitted Cherenkov light cone are shown. Courtesy of Takashi Hachiya. . . . .  | 43 |
| 3.31 | Profile of the ring around the projected charged track intersection point. Courtesy of T. Kajihara. . . . .  | 44 |
| 3.32 | Structural design of EMC sector [37]. . . . .  | 46 |
| 3.33 | Design of PbSc EMC tower [37]. . . . .   | 46 |
| 3.34 | Energy deposited in PbSc EMC by the pion, proton and electron of $E = 0.5, 1.0$ and $2.0$ GeV. . . . .   | 47 |
| 4.1  | Density of the electrons in $\alpha$ vs. $\phi$ space for East Arm. The area indicated by red arrows is the acceptance region used in the analysis. The various acceptance holes and additional photon conversion "shadows" indicated on the plot. . . . . | 50 |
| 4.2  | Density of the electrons in $Z$ vs. $\phi_{PC}$ space. . . . .   | 51 |
| 4.3  | Dead/noisy EMC tower map for E2, E3 EMC sectors. . . . .   | 52 |
| 4.4  | BBC $Z_{vtx}$ distribution for electron candidates ( $n0 > 3$ ). Bold line shows the vertex region used in the analysis. . . . .   | 54 |
| 4.5  | Run-by-run variation of charged particle yield. . . . .  | 55 |
| 4.6  | a) $E/p$ distribution for the electron candidates for different $n0$ cuts b) Rejection power of eID cut $n0 > 2$ in comparison with $n0 > 1$ cut. . . . .  | 57 |
| 4.7  | $E/p$ distribution for the electron candidates and rejection power for different $d_{EMC}$ cuts a) $d_{EMC} < 2\sigma$ b) $d_{EMC} < 3\sigma$ c) $d_{EMC} < 5\sigma$ . . . . .   | 57 |
| 4.8  | Fits to $E/p$ distribution of electron candidates for different $p_T$ bins. . . . .  | 59 |



|      |   |    |
|------|---|----|
| 4.9  | a) Mean and b) Sigma of $E/p$ Gaussian fit to electron signal as a function of $p_T$ (Sigma is fitted with Eq. 4.2 function). . . . .   | 60 |
| 4.10 | "Raw" electron count in $p_T$ bin for Minimum Bias and ERT trigger sample. . . . .  | 62 |
| 4.11 | ERT trigger efficiency for E2, E3 EMC sector. The systematic error band to the efficiency from trigger simulation. . . . .  | 64 |
| 4.12 | $E/p$ distribution for electron candidates (solid curve) and random association tracks $sn0 > 1$ (dashed curve) for Minimum Bias events $p_T > 0.4$ GeV/c. . . . .  | 66 |
| 4.13 | $E/p$ distribution for electron candidates (solid curve), random association tracks (dashed curve) and charged hadron tracks scaled by $\epsilon_{rand} = 3 \cdot 10^{-4}$ (thick solid curve) for Minimum Bias events $p_T > 0.4$ GeV/c. . . . . | 66 |
| 4.14 | Rejection power of $ E/p  < 3\sigma$ for charged hadrons. . . . .   | 66 |
| 4.15 | Total $\delta$ -electron rate as a function of incident pion momentum. . . . .  | 68 |
| 4.16 | The range of $\delta$ -electron kinetic energy that can be reconstructed by RICH, $T_{min}$ (solid) and $T_{max}$ (dashed). . . . .   | 69 |
| 4.17 | Rate of $\delta$ -electrons reconstructible by RICH as a function of incident pion momentum. . . . .  | 69 |
| 4.18 | Mean and sigma of difference between reconstructed and ideal $p_T$ in Simulation for electrons (left) and positrons (right). Linear fit is shown for mean distribution, sigma is fitted with Eq. 4.1 functional form. . . . .                     | 71 |
| 4.19 | Comparison of $\frac{dN_e}{dp_T}$ distribution for weighted PISA simulation (circles) and MB data (squares). Ratio of $\frac{dN_e}{dp_T}$ in MB data to simulation (right). . . . .   | 73 |
| 4.20 | Comparison of acceptance in $\phi$ , $\phi_{EMC}$ , $Z$ , $Z_{EMC}$ for MB data (thin line) and weighted PISA simulation (thick line) for $0.5 < p_T < 2.0$ GeV/c. . . . .  | 73 |
| 4.21 | Comparison of acceptance in $\phi$ , $\phi_{EMC}$ , $Z$ , $Z_{EMC}$ for ERT data (thin line) and weighted PISA simulation (thick line) for $1.5 < p_T < 5.0$ GeV/c. . . . .   | 74 |
| 4.22 | Correction function $\epsilon_{reco}(p_T)$ for $e^+ + e^-$ (full electron ID cuts). . . . .   | 75 |
| 4.23 | Correction function $\epsilon_{reco}(p_T)$ for $e^-$ . Total correction function (dashed curve) shown for comparison. . . . .   | 76 |
| 4.24 | Correction function $\epsilon_{reco}(p_T)$ for $e^+$ . Total correction function (dashed curve) shown for comparison. . . . .   | 76 |
| 4.25 | BBC trigger bias for neutral pions as a function of $\pi^0 p_T$ with the constant fit to the data [47]. . . . .   | 78 |

|      |   |    |
|------|---|----|
| 4.26 | PYTHIA+PISA calculations for BBC efficiency as function of $Z_{vtx}$ for different physical processes. . . . .  | 78 |
| 4.27 | BBC trigger bias for charged hadrons as a function of $p_T$ with fits to the data in two intervals [52]. . . . .  | 79 |
| 4.28 | BBC trigger bias for EXODUS Cocktail electrons as a function of $p_T$ with fits to the data in two $p_T$ intervals. . . . .   | 80 |
| 4.29 | Initial inclusive electron invariant crosssection for Minimum Bias (circles) , ERT trigger (squares). Random Hadronic background level (asterisk) is <b>not</b> subtracted from the data. . . . .   | 81 |
| 4.30 | Systematic error band on the ERT inclusive electron crosssection due to uncertainty of ERT trigger efficiency (Table 4.3). Asymmetric error band (solid) uses the exact variations. Symmetric error band (dashed) is used in the analysis. . . . .  | 83 |
| 4.31 | Inclusive electron invariant crosssection for Minimum Bias (circle) and ERT data sample (squares) (ERT statistical errors includes the systematic error due to ERT trigger efficiency). Combined by Eq. 4.9 inclusive electron invariant crosssection (large circle). Hadronic background is subtracted from both data samples (see Table 4.5). . . . . | 83 |
| 4.32 | Ratio of MB electron inclusive crosssection to ERT crosssection as a function of $p_T$ . . . . .  | 85 |
| 4.33 | Final bin-width corrected inclusive electron invariant crosssection fitted with modified power law function $\frac{p^0}{(p+1+p_T)^{p^3}}$ . . . . .   | 87 |
| 4.34 | Invariant crosssection of charge averaged pions $(\pi^+ + \pi^-)/2$ measured in Run03 $p + p$ collisions [58] (blue) and Run02 $p + p$ $\pi^0$ crosssection [47] (red) fitted with a modified power law function (Eq. 4.13). . . . .  | 89 |
| 4.35 | Ratio of data to fit from Fig. 4.34. . . . .  | 89 |
| 4.36 | Ratio of $\eta$ to $\pi^0$ as function of $p_T$ in Cocktail. . . . .  | 91 |
| 4.37 | (Left panel) $\eta$ -meson invariant crosssection (points) compared with the parameterization used in the current cocktail (statistical errors only). (Right panel) Ratio of data to Cocktail parameterization is shown in the lower panel (error bars are the quadratic sum of statistical and systematic errors). . . . .                             | 91 |
| 4.38 | Electron rate as a function of vertex displacement $d_e$ for $\pi^0$ decay electrons with (blue curve) and without (red curve) the electron ID cut. Contributions from Dalitz, Beam pipe and air conversions indicated by arrows. . . . .   | 93 |
| 4.39 | Ratio of $\pi^0$ conversion electrons to $\pi^0$ Dalitz electrons as a function of electron $p_T$ fitted with a constant. . . . .   | 93 |

|      |  |     |
|------|--|-----|
| 4.40 | Modified power law fit to direct photon yield NLO prediction [65].   | 94  |
| 4.41 | Ratio of $K_{e3}$ decay electrons from simulation to inclusive electrons.  | 95  |
| 4.42 | Final electron "Cocktail" broken into separate contributions overlaid with the inclusive electron data. Bottom plot shows the relative contributions of each Cocktail component to the total. . . . .  | 96  |
| 4.43 | Final bin-width corrected "Non-photonic" electron invariant cross-section fitted with modified power law function $\frac{A}{(p_0+p_T)^n}$ overlaid with PYTHIA default [50] prediction for Open Charm + Bottom electron cross-section. . . . .                                       | 98  |
| 4.44 | Comparison of $\phi$ and $Z$ acceptance of charged tracks in Converter (thin) and Non-converter (thick) run period for different $p_T$ bins. Minimum Bias sample, full electron ID cuts (except $n0 > 1$ ). . . . .  | 100 |
| 4.45 | Ratio of "raw" $\frac{1}{N_{MB}} \frac{dN}{dp_T}$ distributions for Converter and Non-Converter run groups. Charged tracks, full electron ID cuts (except $n0 > 1$ ). . . . .  | 101 |
| 4.46 | Inclusive electron cross-section for MB (left) and ERT trigger (right) for two run groups: Converter (squares) and Non-converter (circles). ERT sample have only statistical errors applied. . .   | 102 |
| 4.47 | Ratio of EXODUS Cocktail electrons from all conversions sources to $\pi^0$ Dalitz electrons. Fit to the data by second order polynomial - exponential. . . . .   | 103 |
| 4.48 | Ratio of photonic electron component with photon converter added to photonic electron component without the converter. .   | 103 |
| 4.49 | "Photonic" electron invariant cross-section for Minimum Bias (circle) and ERT data sample (squares) (ERT statistical errors includes the systematic error due to ERT trigger efficiency). Combined by Eq. 4.9 inclusive electron invariant cross-section (large circle). . . . .     | 105 |
| 4.50 | "Photonic" electron invariant cross-section comparison to Cocktail "Photonic" prediction. . . . .  | 105 |
| 4.51 | Ratio of "Photonic" electron invariant cross-section to Cocktail photonic prediction. . . . .  | 105 |
| 4.52 | "Non-photonic" electron invariant cross-section for Minimum Bias (circle) and ERT data sample (squares) (ERT statistical errors includes the systematic error due to ERT trigger efficiency). Combined by Eq. 4.9 inclusive electron invariant cross-section (large circle). . . . . | 106 |

|      |  |     |
|------|--|-----|
| 4.53 | "Non-Photonic" electron invariant crosssection from Converter subtraction analysis (circles) comparison to Cocktail subtracted "Non-photonic" crosssection (squares). . . . .  | 106 |
| 4.54 | Ratio of "Non-photonic" to "Photonic" electron invariant crosssection for cocktail subtraction and converter subtraction methods. . . . .  | 107 |
| 4.55 | Variation of inclusive electron crosssection for different $d_{EMC}$ matching cut $ d_{EMC}  < 2.0, 2.5, 3.5, 4.0$ . . . . .   | 109 |
| 4.56 | Variation of inclusive electron crosssection for different $E/p$ matching cut $ E/p  < 2.0\sigma, 2.5\sigma, 3.5\sigma, 4.0\sigma$ . . . . .   | 110 |
| 4.57 | Variation of inclusive electron crosssection for different $Z$ acceptance cuts $ Z  < 70, 60cm$ . . . . .  | 110 |
| 4.58 | Variation of inclusive electron crosssection for different Random Hadronic background association efficiency ( $\pm 1\sigma$ ). . . . .  | 111 |
| 4.59 | Comparison of correction function for Fast Simulator (points) and full PISA Simulation (line) for $e^+ + e^-$ . . . . .  | 113 |
| 4.60 | Comparison of correction function for Fast Simulator (points) and full PISA Simulation (line) for electrons. . . . .   | 113 |
| 4.61 | Comparison of correction function for Fast Simulator (points) and full PISA Simulation (line) for positrons. . . . .   | 113 |
| 4.62 | Relative difference between Fast Simulator and PISA simulation correction functions from Fig. 4.59. . . . .  | 113 |
| 4.63 | Correction function calculated under assumption of ideal momentum measurement (solid curve) compared with final Correction function $\epsilon_{reco}(p_T)$ used in the analysis. . . . .   | 114 |
| 4.64 | Variation of the Correction function due to smearing of the momentum resolution from $\sigma_{DCH} = 0.74\%$ to $\sigma_{DCH} = 1.48\%$ compared with final Correction function $\epsilon_{reco}(p_T)$ used in the analysis. . . . . | 114 |
| 4.65 | Variation of inclusive electron crosssection due to 1% absolute momentum scale uncertainty. . . . .  | 115 |
| 4.66 | Comparison of $\phi_{EMC}$ distribution for Fast simulation and PISA without any matching to outer detectors. . . . .  | 116 |
| 4.67 | Ratio of $\phi_{EMC}$ distributions from Fig. 4.66 fitted with constant. This ratio estimates tracking efficiency in Simulation. . . . .   | 116 |
| 4.68 | Ratio of $\phi_{EMC}$ distributions after $n0 > 1$ cut is applied fitted with constant. . . . .  | 116 |
| 4.69 | Ratio of $\phi$ acceptance of Minimum Bias electrons and PISA simulation fitted in two $\phi$ regions shown in the plot. . . . .   | 117 |
| 4.70 | Variation of inclusive electron crosssection for two separate run groups compared to total run statistics. . . . .   | 118 |

|      |  |     |
|------|--|-----|
| 4.71 | Total systematic error on the inclusive electron crosssection. Separate contributions to the systematic shown in the plot. Total systematic is quadratic sum of individual components. . . . .                                 | 119 |
| 4.72 | Systematic uncertainty of the cocktail due to the uncertainty in the pion input spectra. . . . .   | 120 |
| 4.73 | Systematic uncertainty of the cocktail due to the uncertainty in the meson/ $\pi^0$ ratios(see Table. 4.8). $\eta$ , $\eta'$ , $\omega$ , $\rho$ , $\phi$ contributions shown in different colors. . . . .                     | 121 |
| 4.74 | Systematic uncertainty of the cocktail due to the uncertainty in the contribution from photon conversions (light blue curve at about 4 %), from weak kaon decays (green curve), and direct photons (dark blue curve) . . . . . | 121 |
| 4.75 | Total systematic error on the cocktail. . . . .  | 122 |
| 4.76 | Total systematic error on the "Non-photonic" electron invariant crosssection. . . . .  | 123 |
| 5.1  | Default PYTHIA $p_T$ (left panel) and rapidity (right panel) distribution for charm (solid) and bottom (dashed) $Q\bar{Q}$ pairs. . .  | 127 |
| 5.2  | Default PYTHIA $p_T$ (left panel) and rapidity (right panel) distributions for Open Charm (solid) and Open Bottom (dashed) particles. . . . .  | 127 |
| 5.3  | Default PYTHIA $p_T$ (left panel) and rapidity (right panel) distributions for Open Charm (solid) and Open Bottom (dashed) particle decay electrons. . . . .   | 127 |
| 5.4  | Correlation between transverse momentum of charm quark and daughter $D$ -meson (left panel). Correlation between transverse momentum of charm quark and $p_T$ of decay electron (right panel).128                              |     |
| 5.5  | Comparison of Non-Photonic electron crosssection with default PYTHIA expectation for Open Charm and Open Bottom semi-leptonic decays. . . . .  | 129 |
| 5.6  | K-factor for the charm quark as a function of quark rapidity (top) and $p_t^2$ (bottom) for two sets of PDFs: GRV HO (circles), MRS D-' (cross) [73]. . . . .  | 131 |
| 5.7  | K-factor for the charm quark as a function of quark rapidity (top) and $p_t$ (bottom) for CTEQ5 PDF set [19]. . . . .  | 131 |
| 5.8  | Comparison of rapidity and transversal momentum distributions for NLO and LO charm quark production. . . . .   | 133 |
| 5.9  | Comparison of rapidity and transversal momentum distributions for NLO and LO charm quark production. Fit functional form from Eq. 5.2. . . . .   | 133 |

|      |  |     |
|------|--|-----|
| 5.10 | Comparison of Non-Photonic electron crossection with default PYTHIA expectation for Charm + Bottom (solid curve) and HVQLIB tuned PYTHIA expectation for Charm + default PYTHIA bottom (dashed curve). . . . . | 134 |
| 5.11 | Comparison of Non-Photonic electron invariant crossection with HVQLIB tuned PYTHIA (dashed curve) and theoretical prediction from FONLL [87]. . . . .  | 135 |
| 5.12 | Results of the best fit to the shape of the charm, bottom and charm+bottom electron crossections from default PYTHIA. . .  | 138 |
| 5.13 | World data compilation for the ratio of charged to neutral $D$ -mesons $R_{D^\pm/D^0}$ . . . . .   | 138 |
| 5.14 | Fits to the "Non-photonic" electron crossection using PYTHIA expectation for open charm and bottom crossection shape. Different low $p_T$ cut-off values (0.4, 0.5, 0.6, 0.8 GeV/c) used for the fits. . . . . | 140 |
| 5.15 | $\frac{d\sigma_{c\bar{c}}}{dy}$ as a function of low $p_T$ cut-off. . . . .  | 141 |
| 5.16 | Variation of the charm crossection due to the systematic error of the "Non-photonic" crossection. . . . .  | 141 |
| 5.17 | World Data compilation for Open Charm crossection as a function of $\sqrt{s}$ . Modified version of the plot from [72]. . . . .  | 142 |

## List of Tables

|      |   |     |
|------|---|-----|
| 3.1  | Summary of the PHENIX Detector Subsystems [37]. . . . .   | 18  |
| 3.2  | Performance of Pad Chambers in RUN-2 [44]. . . . .  | 41  |
| 4.1  | Statistics summary for Non-Converter and Converter run period.  | 55  |
| 4.2  | "Raw" electron count in $p_T$ bin for Minimum Bias and ERT trigger sample. . . . .  | 62  |
| 4.3  | Fit results for ERT trigger efficiency and hi-lo systematic error band for E2,E3 EMC sectors. . . . .   | 63  |
| 4.4  | BBC trigger bias fit results for different particles. All values have 3% systematic uncertainties [52] . . . . .  | 80  |
| 4.5  | Initial inclusive electron invariant crossection for Minimum Bias, ERT trigger. Random Hadronic background level is <b>not</b> subtracted from the data. Crossection and statistical errors are in units of $[mb \cdot c^3/GeV^2]$ . . . . .  | 82  |
| 4.6  | Inclusive electron invariant crossection for MB and ERT data sample (ERT statistical errors includes the systematic error due to ERT trigger efficiency). Combined inclusive electron crossection with statistical error. Hadronic background is subtracted from both data samples (see Table 4.5). Crossection and statistical errors are in units of $[mb \cdot c^3/GeV^2]$ . . . . . | 85  |
| 4.7  | Final inclusive electron invariant crossection before and after the bin width correction. . . . .   | 87  |
| 4.8  | Ratios of light mesons to $\pi^0$ at high $p_T$ . . . . .   | 90  |
| 4.9  | $K_{e3}$ decay branching ratio and Decay Length for different Kaon species. . . . .   | 95  |
| 4.10 | Non-photonic electron invariant crossection. . . . .  | 98  |
| 4.11 | Components of the total systematic error on the inclusive crossection. . . . .  | 119 |
| 5.1  | Ratio of the Open Charm particles to $D^0$ and the corresponding semi-leptonic decay branching ratios for World Data average and PYTHIA. . . . .  | 139 |

## Acknowledgements

First of all I would like to express my deepest gratitude to my colleagues from SUNYSB and PNPI for letting me to take part in the creation and running of one of the most pioneering physics devices in high energy field - PHENIX detector. Especially I would like to thank Professor Thomas Hemmick, for teaching me basically all the aspects of modern experimental physics, for trusting in me and his unique ability to strive for perfection. I want to thank Dr. Federica Messer and Professor Axel Drees for giving me a chance to participate in an exciting and challenging world of PHENIX software, all the members of the PHENIX electron working group (especially Dr. Yasuyuki Akiba and Dr. Ralf Aeverbeck) for an encouraging results in the development of the signal extraction technique, used in this work and a significant contribution to the analysis. Needless to say that without the friendly team of graduate students at Nuclear and Heavy Ion group (Felice Matathias, Jianyong Jia, Anuj Purwar, Jamil Egdemir) this mission would never have been accomplished. Thank you very much for fruitful and thought-provoking discussions and support.



# Chapter 1

## Introduction

Heavy quarks are a unique tool in High Energy and Nuclear Physics. Discovered in 1974, the charm quark has attracted the attention of both experimentalists and theoreticians. The production of particles with Open Charm (carrying a single  $c$  or  $\bar{c}$  quark, such as  $D$ -mesons and  $\Lambda_c$  baryons) and Closed Charm ( $c\bar{c}$  mesons) is a rare process purely from energy considerations, because the charm mass,  $m_c \approx 1.2 - 1.5$  GeV, is so high. This energy scale allows one to use (with some caution, of course) perturbative Quantum Chromodynamics (pQCD) - a theoretical model of the strong color field interaction to describe the production mechanisms and rates of Open Charm.

Open Charm particles are produced through the fragmentation of  $c\bar{c}$  pairs. Creation of those pairs is intrinsically sensitive to the initial state of the partonic system. pQCD predicts that the primary production mechanism in Leading Order approximation is "gluon fusion". Thus, the production rate of charm pairs is proportional to the initial gluon density inside the collision. Open Charm production in heavy ion collisions at the Relativistic Heavy Ion Collider (RHIC) can thereby lead us to understanding how the initial properties of the matter change with the size of the colliding system. RHIC raised the High Energy Nuclear physics to the next level, enabling us to study with the same detector setup the full variety of collisions -  $p + p$ ,  $d + Au$ ,  $Au + Au$  at  $\sqrt{s} = 200$  GeV. Detailed comparison of Open Charm production in those collisions will help us to answer the fundamental questions:

- What are the mechanisms governing charm production?  
The  $p + p$  collision is a reference measurement, which should be exactly explainable by perturbative QCD. Production of Open Charm at lower energies has always been a serious confirmation of pQCD's applicability for heavy quarks. So far, exact calculations from pQCD exist to second order (NLO) [2, 3, 4, 5, 6] and describe the lower energy data within the theoretical uncertainties. It may well be that at our high energy, the

theory cannot neglect these higher order partonic interaction processes in order to describe the data. The theory of hadronization of the  $c$  and  $\bar{c}$  is presently at a rudimentary stage and in order to constrain the different theoretical predictions, we need to study  $p + p$  collisions at different rapidity ranges.

- How does the production sensitive to additional "cold" matter in the collision?

A comparison of  $p + p$  production with  $d + Au$  will measure the modification of the gluon structure function in "cold" hadronic matter. In this case, the ability to perform rapidity scan is essential to study the  $x$  dependence of the gluon modification factor that was clearly observed in case of light quark mesons.

- What happens with the charm quark production in "hot" dense matter of  $Au + Au$  collisions?

Direct comparison of charm production crosssection in  $Au + Au$  with  $d + Au$  and  $p + p$  will answer this question. So far there are a lot of different predictions, expecting both enhancement due to the initial state thermal production and suppression due to the media induced gluon radiation. So far, we observed a significant suppression for the light quarks, in case of the heavy quark this effect may be significantly reduced due to the suppression of gluon radiation at small angles for the charm quark.

There is a lot of very interesting new physics that can be discovered if this program is accomplished. In this thesis we begin the program by accomplishing the baseline measurement of Open Charm production in  $p + p$  collisions at mid rapidity.

There are two experiments at RHIC capable of performing this task, each with certain advantages and disadvantages - PHENIX and STAR.

PHENIX was a pioneer in Open Charm measurements at RHIC. Built with a strong accent towards the electron and muon identification, PHENIX successfully measured Heavy Flavor production at  $\sqrt{s} = 130$  GeV [50]. Fig. 1.1 shows the invariant multiplicity for the electrons, originated from the semi-leptonic decay of the charm and bottom quarks  $c(b) \rightarrow eX$ .

STAR also has elaborated electron identification using Electromagnetic Calorimeter, Time-of-Flight Detector and Time Projection Chamber. They were able to perform similar semi-leptonic measurement in  $p + p$  and  $d + Au$  collisions at  $\sqrt{s} = 200$  GeV [72]. But STAR has also been able to directly measure decays of  $D$  mesons into hadronic channels. This is a more direct measurement of the Open Charm production then measuring decay leptons.

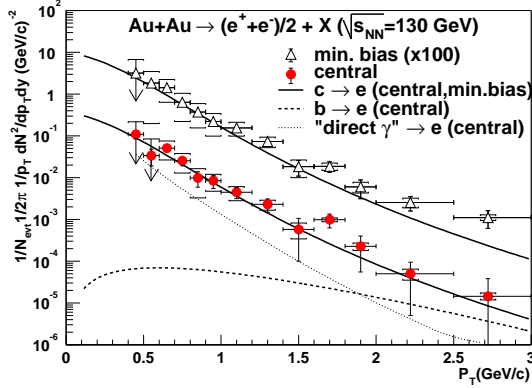


Figure 1.1: Invariant cross section for "Non-photonic" electrons at  $\sqrt{s} = 130$  GeV at PHENIX [50].

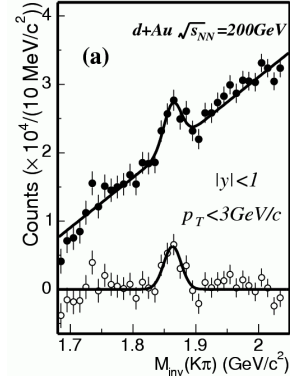


Figure 1.2: Mass spectrum of  $K\pi$  pairs in  $d + Au$  collisions with clear  $D^0$  peak [72]

Fig. 1.2 shows the reconstruction of  $D^0 \rightarrow K\pi$  decay channel by STAR collaboration. It is doubtful that these measurements can be also done in case of  $Au + Au$  collisions. Direct measurement of hadronic decays of Open Charm mesons in PHENIX is very hard due to the limited acceptance for these decays.

My dissertation sets the cornerstone to the foundation of the Heavy Flavor measurements at energy  $\sqrt{s} = 200$  GeV - I will present the experimental measurement of Open Charm production at mid-rapidity in PHENIX at RHIC from single electron channel ( $c \rightarrow eX$ ). The paper is organized in the following way: Chapter 2 presents the current theoretical aspects of the heavy quark production and fragmentation. The experimental setup, used in the analysis is described in Chapter 3. Chapter 4 is dedicated to data reduction towards the final Open Charm electron cross section. A discussion and theoretical comparison is summarized in Chapter 5 and final conclusions and a future outlook are presented in Chapter 6.

## Chapter 2

### Theory

#### 2.1 Quantum Chromodynamics

Quantum ChromoDynamics (QCD) is the set of physical laws, describing our current understanding of strong interactions between the quarks and gluons. QCD was developed as an extension of Quantum Electrodynamics via the imposition of a local  $SU(3)$  symmetry of rotation in color space. The Standard Model couples the  $SU(3)$  strong interaction with the unified electro-week interaction making the overall symmetry group  $SU(3) \times SU(2) \times U(1)_Y$ . The Standard Model describes the large variety of mesonic and baryonic states by the existence of the deeper level of elementary constituents of matter: **quarks** [8]. All the variety of particles that can be found in Particle Data Tables [9] can be explained in terms of six spin- $\frac{1}{2}$  quark **flavors**:

|                    |       |
|--------------------|-------|
| $Q = +\frac{2}{3}$ | u c t |
| $Q = -\frac{1}{3}$ | d s b |

The meson state in this case consists of quark-antiquark ( $q\bar{q}$ ) and baryonic state is a combination of three quarks ( $qqq$ ) or antiquarks ( $\bar{q}\bar{q}\bar{q}$ ), this model gives us a unique correspondence between the observed particle and its state.

However, the early quark picture faced a problems with Fermi-Dirac statistics, for example  $\Lambda^{++}$  baryon ( $J = \frac{3}{2}$ ) should have been explained as a combination of  $u \uparrow u \uparrow u \uparrow$  quarks which contradicts Fermi statistics of spin- $\frac{1}{2}$  particles. This problem was solved by introducing a new quantum number [10], **color**, such that each species of quark can have  $N_C = 3$  different colors. In this picture mesons and baryons are described as color-singlet combinations of colored quarks.

$$B = \frac{1}{\sqrt{6}}\epsilon^{\alpha\beta\gamma}|q_\alpha q_\beta q_\gamma\rangle \quad M = \frac{1}{\sqrt{3}}\epsilon^{\alpha\beta}|q_\alpha \bar{q}_\beta\rangle \quad (2.1)$$

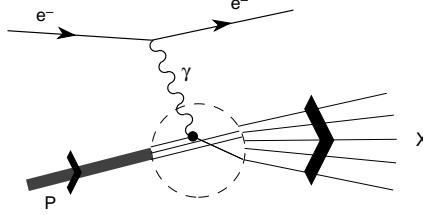


Figure 2.1: Deep Inelastic  $e^- p \rightarrow e^- X$  scattering. [1]

States, with color content not equal to zero were never observed, which led the theorists to postulate the hypothesis that all states are color-singlets. This statement is known as “**confinement hypotheses**” implying directly the non-existence of free quark colored states.

The next valuable piece to the construction of the QCD theory was obtained from “**deep inelastic scattering**” (DIS) of high energy electrons on the proton. Fig. 2.1 shows the interaction of the electron with the content of the proton.

At higher energies, the virtual photon is sensitive to smaller distances and we are thereby able to resolve the structure of the proton by increasing the energy of the electron beam. Denoting the photon momentum transfer as  $Q^2 = 4EE' \sin^2(\theta/2)$ , where  $E$  and  $E'$  are incident and scattered electron energies.

From the studies of scattering crosssections, it was found that at large values of  $Q^2$  a sizable continuum contribution to the crosssection still persists, suggesting an existence of pointlike objects inside the proton. Those pointlike spin- $\frac{1}{2}$  constituents were called *partons*. It was also found that proton structure functions only depends on the transferred momentum  $Q^2$  and the relative contribution of parton momentum to the total proton momentum  $x$  [11]. This surprising discovery of pointlike partons inside the proton, initially contradicting previously explained confinement of the quarks by a strong color force leads to an fundamental property of strong interactions known as “*asymptotic freedom*” - the interaction between quarks should become weaker at short distances, so that at high  $Q^2$  transfer, quarks behave as free particles. The interaction in  $q\bar{q}$  system grows as we try to separate the quarks. At some point the energy of the string become more then  $2m_Q$ , where  $m_Q$  is the mass of another quark. It becomes energetically favorable to split the string into two  $q\bar{Q}$  and  $Q\bar{q}$  mesons. By increasing the energy, we can create more and more colorless meson states. Otherwise, if we try to approach two quarks, the

potential loses strength and the quarks start behave like free particles.

The field carriers in QED theory are photons, and the QED Lagrangian describes the interaction of a Dirac fermion with the electromagnetic field  $A_\mu$ . By analogy, the QCD Lagrangian can be constructed. This Lagrangian will describe the interaction of  $q_f^\alpha \bar{q}_f^\alpha$  quarks of color  $\alpha$  and flavor  $f$ . The free Lagrangian is given by Eq. 2.2 [1].

$$L_0 = \sum_f \bar{q}_f (i\gamma^\mu \partial_\mu - m_f) q_f \quad (2.2)$$

Propagation of the quark wave function requires the Lagrangian to be invariant under local  $SU(3)_C$  color space transformation. This invariance introduce  $3^2 - 1 = 8$  component gauge bosons  $G_a^\mu(x)$ , those particles are called **gluons**. The total invariant Lagrangian of QCD can be written as follows [1]:

$$\begin{aligned} L_{QCD} = & -\frac{1}{4} (\partial^\mu G_a^\nu - \partial^\nu G_a^\mu) (\partial_\mu G_a^\nu - \partial_\nu G_a^\mu) + \sum_f \bar{q}_f^\alpha (i\gamma^\mu \partial_\mu - m_f) q_f^\alpha \\ & + g_s G_a^\mu \sum_f \bar{q}_f^\alpha \gamma_\mu \left( \frac{\lambda^a}{2} \right)_{\alpha\beta} q_f^\beta \\ & - \frac{g_s^2}{2} f^{abc} (\partial^\mu G_a^\nu - \partial^\nu G_a^\mu) G_\mu^b G_\nu^c - \frac{g_s^2}{4} f^{abc} f_{ade} G_b^\mu G_c^\nu G_\mu^d G_\nu^e \end{aligned} \quad (2.3)$$

The first line presents the kinetic energy of quark and gluon field. The second line describes the color interaction between gluon and quark, where  $\lambda^a$  are color field  $SU(3)_C$  matrices. The last line shows gluon self-interactions, exhibiting non-abelian properties of the color field<sup>1</sup>. The coupling constant  $g_s$  is the universal *strong coupling constant*. Examples of  $q\bar{q} \rightarrow gg$  scattering Feynman Diagrams allowed in QCD are shown in Fig. 2.2 [1].

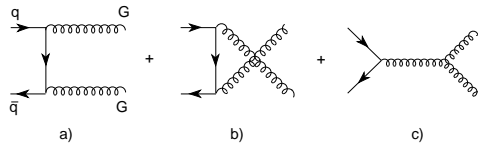


Figure 2.2: Tree-level Feynman diagrams contributing to  $q\bar{q} \rightarrow gg$ . [1]

---

<sup>1</sup>Gluon field self-interaction is a striking difference of QCD, compared to QED, where photon can not split into two photons

## 2.2 Renormalization of QCD

Renormalization techniques have been widely developed in QED as a useful mechanism to absorb the loop diagrams that cause logarithmic divergences. Ultraviolet logarithmic divergences appear in QED if the photon polarizes the vacuum, creating a virtual  $e^+e^-$ -pair. The calculated crosssection for this loop process produces an infinity which is "non-physical". In order to solve this problem, we assume (see Fig. 2.3) that for  $e^+e^-$ -interactions processes, the effective coupling constant that we measure is changing due to vacuum polarization. The "bare" coupling constant in QED has been known since Thompson experiments as  $\alpha_0 = e^2/(4\pi) \approx 1/137$ . Assuming that the coupling may vary as a function of photon transferred energy  $Q^2$  due to appearance of the loops leads to very powerful conclusion that the we can actually measure **renormalized running coupling**  $\alpha^{QED}(Q^2)$  which can be written as:

$$\alpha^{QED}(Q^2) = \frac{\alpha^{QED}(Q_0^2)}{1 - \frac{\beta_0 \cdot \alpha^{QED}(Q_0^2)}{2\pi} \ln(Q^2/Q_0^2)} \quad (2.4)$$

where  $\beta_0$  is a solution of differential equation (2.5) and for one loop contribution is equal to  $\beta_0^{QED} = \frac{2}{3}$ .

$$Q^2 \frac{d\alpha}{dQ^2} \equiv \alpha \beta(\alpha); \quad \beta(\alpha) = \beta_0 \frac{\alpha}{\pi} + \beta_1 \left(\frac{\alpha}{\pi}\right)^2 + \dots \quad (2.5)$$

$Q_0^2$  is an arbitrary scale, at which we can neglect the contributions from the radiative corrections. We can take it as  $Q_0^2 \rightarrow 0$  which produces classical value for the coupling constant  $\alpha(Q_0^2) = \alpha_0 = 1/137$ .

The fact that  $\beta_0 > 0$  leads to the conclusion that alpha is growing with the increase of the energy transferred and, i.e. the effective charge of the electron is decreasing with the distances between the charges. This is intuitively understandable as the produced virtual  $e^+e^-$ -pairs acts like a screen around the charge in the polarized dielectric medium.

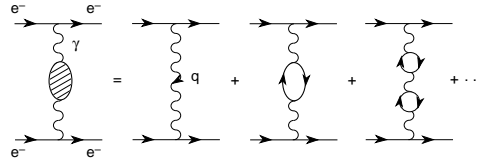


Figure 2.3: Photon self-energy contribution to  $e^-e^-$  scattering. [1]

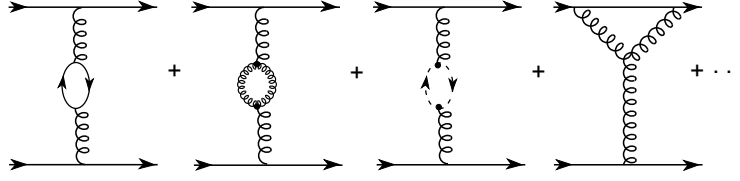


Figure 2.4: Feynman diagrams contributing to the renormalization of the strong coupling. [1]

A similar renormalization approach can be applied to the QCD theory, but in the case of QCD we need to take into account gluon self-interaction diagrams. Processes, contributing to the renormalization of the scale are shown in Fig. 2.4. The final equation for the QCD running coupling gives identical result to QED Eq. 2.4, but the  $\beta$  function will be drastically different [12].

$$\beta_0 = \frac{2 N_f - 11 N_C}{6} \quad (2.6)$$

where  $N_f$  is a number of flavors,  $N_C$  is the number of colors. The first term is due to the creation of  $q\bar{q}$  loops of different flavor and is similar to the QED value. The second, negative contribution in Eq. 2.6 corresponds to gluonic self-interaction loops and is proportional to number of colors. The existence of the second term makes the factor  $\beta_0$  negative for  $N_f < 16$  this leads to the important result that at short distances (large  $Q^2$ )  $\alpha_s(Q^2) \rightarrow 0$ . This is direct confirmation of *asymptotic freedom*.

In the one loop approximation we can write the strong interaction running coupling as (solving Eq. 2.5 for  $\alpha$ ):

$$\alpha_s^{(0)}(Q^2) = \frac{2\pi}{-\beta_0 \ln(Q^2/\Lambda_{QCD}^2)} \quad (2.7)$$

where  $\Lambda_{QCD}$  comes as an integration parameter at an energy scale at which the QCD coupling constant starts to exhibit non-perturbative properties. If the momentum transfer  $Q$  is much larger then  $\Lambda_{QCD}$ , we are in asymptotic freedom regime and  $\alpha_s(Q^2) \rightarrow 0$  allows us to use the **perturbative QCD** (pQCD) technique. In the case of energy transfer, comparable to  $\Lambda_{QCD}$ , Eq.2.7 blows-up the strong coupling constant making all orders diagrams to be of similar contribution and the pQCD approach cannot be used.



It is necessary to add that there are several theoretical approaches to pQCD renormalization (referred to as the *renormalization scheme*). Currently, the most adopted and cited approach is use of  $\overline{MS}$  - modified minimal subtraction scheme [13].

In  $\overline{MS}$  case the next orders of two loop corrections we have following expression for next term of  $\beta$  function deconvolution Eq. 2.5 [14].

$$\beta_1 = -\frac{51}{4} + \frac{19}{12} N_f \quad (2.8)$$

For  $N_f \leq 8$ ,  $\beta_1 < 0$  which even stronger justifies the use of asymptotic freedom. Fig. 2.5 shows the dependence of  $\alpha_s$  on the energy scale  $Q$  for the experimental data comparison with pQCD theory [15]. It is also clearly seen from this figure that  $\Lambda_{QCD}$  is on the order of  $\sim 220$  MeV and should be calculated for the expected number of flavors ( $\Lambda_{QCD}^{(5)}$  assumes  $N_f = 5$ ).

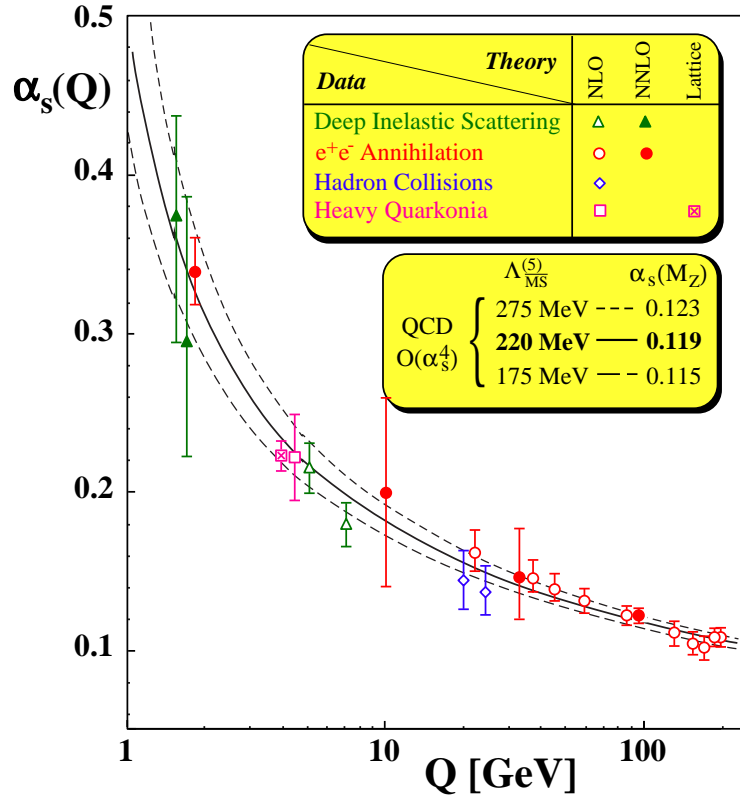


Figure 2.5: Measurements of  $\alpha_s$  as a function of energy scale [15].

## 2.3 Heavy quark production in QCD

In this section I discuss the production mechanisms of heavy quark particles in  $p + p$  collisions using the perturbative QCD formalism, described in previous Section.

The main advantage of the heavy quark measurements is that the initial content of the heavy flavor in the proton is negligibly small (there are some papers though that assume the intrinsic heavy quark content of the nucleon to be non-zero [16, 17] but we will not include this aspect into our considerations). Then, the heavy quarks should be produced in hard partonic scattering. The big advantage of the heavy quark production is that the energy scale for the production of charm quarks  $Q^2 \sim m_c^2$  is significantly higher than  $\Lambda_{QCD}$ . This gives us a coupling constant of the order of  $\alpha_s \sim (0.3 - 0.5)$  (see Fig. 2.4), which is small enough to utilize perturbative theory. pQCD should give even more accurate results for the higher mass bottom quark.

## 2.4 Hard scattering processes

In the partonic model we can assume that the colliding protons consist of a collection of partons (quarks, antiquarks, gluons) that interact with the content of the other proton. In Leading Order pQCD, hard scattering of the partons can create heavy quark-antiquark pairs  $Q\bar{Q}$  by the diagrams, shown in Fig. 2.6a,b). LO sub-processes are usually called "gluon fusion" ( $gg \rightarrow Q\bar{Q}$ ) and "quark-antiquark annihilation" ( $q\bar{q} \rightarrow Q\bar{Q}$ ).

The general perturbative extension for the total crosssection of quark pair production on the partonic level can be expressed by the following equation [19].

$$\sigma_{ij}(\hat{s}, m_Q^2, \mu_R^2) = \frac{\alpha_s^2(\mu_R^2)}{m_Q^2} \sum_{k=0}^{\infty} (4\pi\alpha_s(\mu_R^2))^k \sum_{l=0}^k f_{ij}^{(k,l)}(\eta) \ln^l \left( \frac{\mu_R^2}{m_Q^2} \right) \quad (2.9)$$

where  $\hat{s} = x_1 x_2 s$  is the partonic energy in center of mass. The useful dimensionless parameter  $\eta = \hat{s}/4m_Q^2 - 1$  [20] reflects the threshold production of the heavy quark ( $\sqrt{\hat{s}}$  should be at least  $2m_Q$  to create a quark-antiquark pair).  $i$  and  $j$  are the partonic indexes corresponding to each particular Feynman diagram on the Fig.2.6.  $f_{ij}^{(k,l)}(\eta)$  is a dimensionless scaling function representing

---

<sup>2</sup> $Q$  index refers to heavy quarks

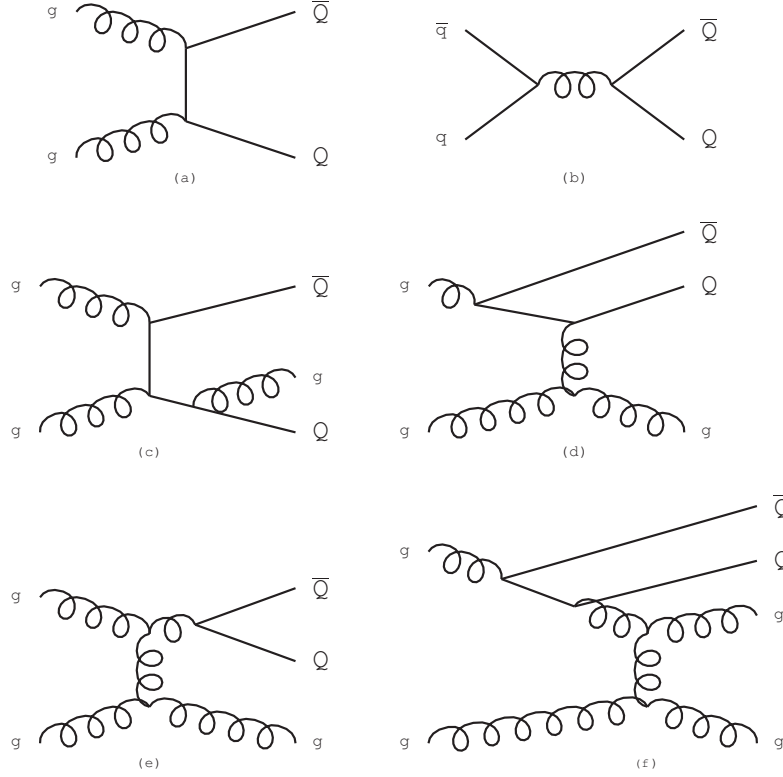


Figure 2.6: LO and most important NLO heavy quark production diagrams. LO - a) "gluon fusion" b) "quark-antiquark annihilation" NLO - c) Pair creation with gluon emission in output channel d) "flavor excitation" e) "gluon splitting" f) "gluon splitting but of "flavor excitation" character [18]

the amplitude of a given partonic scattering diagram. Index  $k$  shows the order of the process diagram,  $k = 0$  corresponds to LO, one can see that in the leading order the total crosssection is a function of  $\alpha_s^2$ . Next order of perturbation  $k = 1$  corresponds to Next-Leading-Order (NLO) contributions (some of the NLO diagrams are shown in Fig. 2.6c-d)). The NLO crosssection is of the order of  $\alpha_s^3$  and in principle are of the next order of smallness, unfortunately, the NLO crosssection develops a logarithms term for  $l = 1$  which can  $\ln(\frac{\mu_B^2}{m_Q^2})$  be make NLO crosssection of the order and even higher then the LO contribution. Case of  $k = 2$  is usually referred to as Next-to-Next Leading Order (NNLO) so far the exact crosssection for NNLO heavy quark production has not been calculated because of a large number of contributing diagrams and mathematical complications in resummation procedure. There have been

theoretical attempts to calculate the NNLO cross-section contribution near production threshold [20].

$Q^2$  in Eq. 2.9 is called **renormalization scale** and usually assumed to be proportional to  $m_Q^2$  or  $m_Q^2 + p_{TQ}^2$  depending on the model. The proportionality coefficient  $sc_R$  in  $\mu_R^2 = (sc_R \cdot m_Q)^2$  is a variable parameter in QCD and usually assumed to be in the range of  $sc_R \in (\frac{1}{2}; 2)$ . Low values of  $sc_R = \frac{1}{2}$  for charm quark creation produces scales on the order of  $m_c^2/4 \leq 1 \text{ GeV}^2$  and from Fig. 2.5 one can see that  $\alpha_s$  becomes quite large to utilize perturbative technique.

The next general step in QCD is to assume that we know the distribution of the partons inside of the proton. This distribution is called **parton distribution function** (PDF) [21, 22]  $f_i^p(x, \mu_F^2)$  described in terms of Feynman variable  $x$  and the momentum transfer scale  $\mu_F^2$ .  $x$  is a relative fraction of partonic momentum to the total momentum of the hadron  $x_i = \frac{p_{zi}}{p_{zmax}}$ . Scale dependence of the PDF is described by DGLAP equations [23, 24, 25] and the shape of the parton distribution is derived from comparison of pQCD predictions to experimental measurements.

Fig. 2.7 shows the most striking agreement of pQCD prediction and the results of  $\pi^0$  and direct- $\gamma$  production in  $p+Be$  collisions from E706 experiment. The results show the existence of non-zero smearing of the transverse  $\langle k_T \rangle \approx 1 \text{ GeV}$  of the parton (so called intrinsic  $k_T$ ). Experimental results helped to constrain the gluon distribution function with very good accuracy. There is a big variety of PDF functions developed by different theory groups. At the current moment, the CTEQ group's PDF set [22] seems to be the most accurate in describing existing experimental data for the structure of the proton.

Taking the assumption of the parton distribution, we can write the total cross-section for Heavy Flavor production [19]

$$\sigma_{pp}(s, m_Q^2) = \sum_{i,j=q,\bar{q},g} \int_{\frac{4m_Q^2}{s}}^1 d\tau \int_{\tau}^1 \frac{dx_1}{x_1} f_i^p(x_1, \mu_F^2) f_j^p\left(\frac{\tau}{x_1}, \mu_F^2\right) \sigma_{ij}(\tau s, m_Q^2, \mu_R^2) \quad (2.10)$$

where  $\sigma_{ij}(\tau s, m_Q^2, \mu_R^2)$  is the partial partonic cross-section (Eq. 2.9),  $\mu_F^2$  is a momentum transfer scale (**factorization scale**) of the PDF factorization. The usual assumption for pQCD calculations is to expect the factorization and renormalization scales to be similar  $\mu_R^2 = \mu_F^2 = \mu^2$  since all PDFs uses this assumption *a priori* in calculations [19].

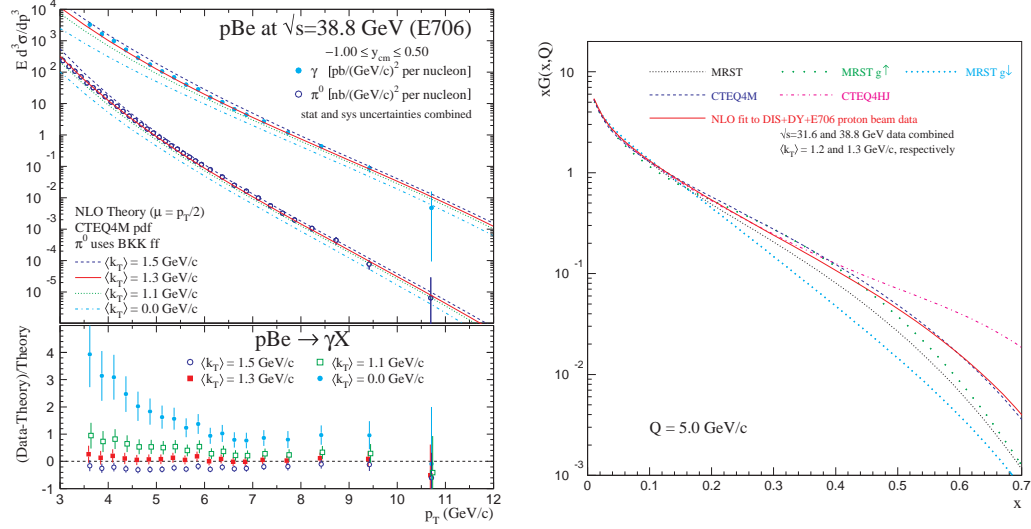


Figure 2.7: Comparison of the photon and direct- $\gamma$  measured by *E706* experiment in  $p + Be$  collisions at  $\sqrt{s} = 38.8$  GeV with pQCD predictions for different values of  $\langle k_T \rangle$  smearing (left panel). Comparison of gluon structure function for most recent PDF sets (right panel). [26]

## 2.5 $Q\bar{Q}$ fragmentation

After the quark-antiquark pair is created, each of the produced heavy quarks picks up a light quark from the proton in order to create a color singlet object (**string**). The string is fragmented into hadrons using a phenomenologically determined **fragmentation function**  $D(z)$  where  $z$  is the momentum fraction of the quark, carried by the hadron.  $D(z)$  determines the probability of producing hadron with given momentum.

By default, PYTHIA (a widely used pQCD Monte Carlo program) uses the Lund fragmentation function [27] modified by Bowler [28]:

$$D(z)_{LUND} \propto \frac{(1-z)^a}{z^{1+bm_Q^2}} \exp\left(\frac{-bm_T^2}{z}\right) \quad (2.11)$$

where  $m_T^2 = m_h^2 + p_T^2$  is the transverse mass of the hadron. The default parameter values in PYTHIA are  $a = 0.3$  and  $b = 0.58 \text{ GeV}^{-2}$ .

A different parametrization of the fragmentation function was proposed by Peterson [29]

$$D(z)_{\text{Peterson}} \propto \frac{1}{z(1 - 1/z - \epsilon/(1 - z))^2} \quad (2.12)$$

The central value for  $\epsilon$  in  $D$ -meson decay usually assumes to be  $\epsilon = 0.06$  [30, 31] in case of LO theory fits to the data, this parameter is much smaller if NLO fits are used for parameter extraction ( $\epsilon = 0.01 - 0.02$ ) [32].

Now we have everything to calculate the single differential crosssection for the produced Heavy Flavor hadrons. The non-perturbative hadron production can be obtained using the *factorization theorem*:

$$\frac{d\sigma^H}{dp_T} = \int dp_T^Q dz \frac{d\sigma^Q}{dp_T^Q} D(z) \delta(p_T - zp_T^Q) \quad (2.13)$$

where  $\frac{d\sigma^Q}{dp_T^Q}$  is single differential crosssection for heavy quark.

Heavy Flavor hadroproduction is currently a subject to significant uncertainty. The most accurate approach to deriving the fragmentation function is to use the Mellin transforms of the  $D(z)$  and obtain the momenta of this transform from the experimental data [33, 34, 35]. Mellin transformation is a decomposition of the function on the powers of  $N$  according to the following formula [34]:

$$D_N \equiv \int D(z) z^N \frac{dz}{z} \quad (2.14)$$

Assuming the quark  $p_T$  distributions have power law behavior  $\frac{d\sigma}{d\hat{p}_T} = \frac{A}{\hat{p}_T^n}$  in the neighborhood of some  $p_T$ , one can immediately find from Eq. 2.13 that

$$\frac{d\sigma^H}{dp_T} = \int d\hat{p}_T dz \frac{A}{\hat{p}_T^n} D(z) \delta(p_T - z\hat{p}_T) = \frac{A}{p_T^n} D_n \quad (2.15)$$

Thus, the hadronic crosssection is given by the product of  $n^{\text{th}}$  moment of the fragmentation function. Recent results from the ALEPH collaboration on the bottom meson energy transfer indicates that Peterson fragmentation form **does not** describe the calculated momenta of the fragmentation function (see Fig. 2.8). More studies of fragmentation function form for Heavy Flavor mesons need to be performed to remove this apparent uncertainty.

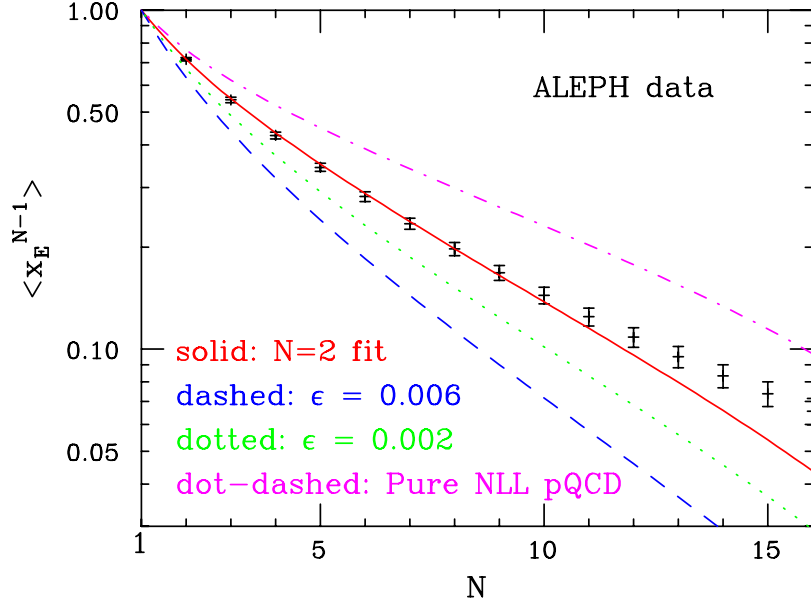


Figure 2.8: Momenta of measured B meson fragmentation function compared with pQCD NLL calculations with different assumptions for  $D(z)$ . The solid line is one-parameter fit to the second momentum [34].

## 2.6 Heavy Flavor meson decay

Heavy flavor semi-leptonic decay diagrams for  $D$  and  $B$  mesons are shown in Fig. 2.9. This weak decay channel should be calculable using the standard technique, developed for decay of free mesons (*spectator model*) [36].

The total semi-leptonic decay rate can be written as

$$\Gamma_{sl}^Q = \frac{m_Q}{2^8 \pi^3} \int dx dy \theta(x + y - x_m) \theta(x_m - x - y + xy) \times \overline{\sum} |M^Q|^2 \quad (2.16)$$

where  $x = 2E_e/m_Q$  and  $y = 2E_\nu/m_Q$  are the rescaled energies of charged and neutral lepton in the heavy quark rest frame.  $x_m = 1 - (m_q/m_Q)^2$  is kinematic limit to the energy transfer.

Matrix decay elements equal to:

$$\overline{\sum} |M^c|^2 = 64 G_F^2 |V_{cs}|^2 c \cdot e^+ s \cdot \nu \quad \overline{\sum} |M^b|^2 = 64 G_F^2 |V_{cb}|^2 b \cdot \nu c \cdot e^+ \quad (2.17)$$

where  $c, b, s, e^+, \nu$  are corresponding 4-momenta of the decay particles.  $|V_{cs}|, |V_{cb}|$  are elements of Cabibbo-Kobayashi-Maskawa (CKM) flavor mixing matrix.  $G_F = 1.16637 \cdot 10^{-5} \text{ GeV}^{-2}$  is Fermi constant of weak interaction.

From Eq. 2.16 we can now calculate the differential semi-leptonic decay rate for the Heavy Flavor meson.

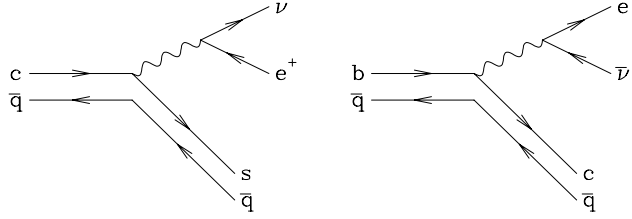


Figure 2.9: Semi-leptonic decay diagrams for Open Charm and Open Bottom meson semi-leptonic decay.

$$\begin{aligned} \frac{d\Gamma_{sl}^c}{dx} &= |V_{cs}|^2 \Gamma_0(m_c) \left[ \frac{12x(x_m - x)^2}{(1 - x)} \right] \\ \frac{d\Gamma_{sl}^b}{dx} &= |V_{cb}|^2 \Gamma_0(m_b) \left[ \frac{2x^2(x_m - x)^2}{(1 - x)^3} \right] (6 - 6x + x x_m + 2x^2 - 3x_m) \end{aligned} \quad (2.18)$$

where  $\Gamma_0(m_Q) = \frac{G_F^2 m_Q^5}{192 \pi^3}$ . Fig. 2.10 shows the resulting decay rate as a function of relative electron energy for  $c \rightarrow s$ ,  $c \rightarrow d$ ,  $b \rightarrow c$ ,  $b \rightarrow u$  semi-leptonic decays.

Thus, pQCD theory provides us with the solid prescription to calculate the Heavy Flavor production, hadronization and decay.

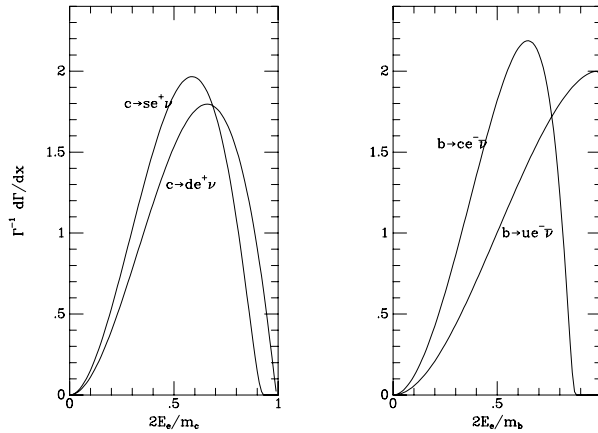


Figure 2.10: Semi-leptonic decay rate as a function of  $2E_e/M_Q$  for Open Charm (left panel) and Open Bottom (right panel) [36].



## Chapter 3

### PHENIX Experiment

#### 3.1 PHENIX Detector

PHENIX is one of the most advanced detector systems in High Energy Nuclear Physics. It consists of 14 independent detector subsystems collecting the information about the particles produced in Heavy Ion collisions. The PHENIX tracking system provides accurate measurements of charged particle tracks and particle identification (electron, muon, hadron identification) over wide range of momentum. Together with charged particle tracking, PHENIX also performs a high precision measurements of photons via a large area Electro-Magnetic Calorimeter. A sophisticated Level-1 and Level-2 trigger system, enables a unique ability to address specific **rare** physics events recording at high luminosity ( $J/\psi$  leptonic decays, for example, by triggering on a pair of highly energetic electron candidates). All those factors make PHENIX both the most challenging and the most capable detector in RHIC to study Heavy Flavor particle productions.

The detectors in PHENIX are grouped into three major categories by design and specific physics tasks they are intended to perform:

- Global Trigger Detectors
- Central Arm Detectors
- Muon Arm Detectors

The PHENIX detector is shown in Figure 3.1. It is symmetric around mid-rapidity with the interaction point positioned in the center of the magnets, commonly referred to as the Interaction Region (IR). Two Central Arm detectors (referred to as East and West) are located around the interaction point and cover the rapidity range  $-0.35 < \eta < 0.35$ . Each Central Arm covers  $90^\circ$  in  $\phi$

Table 3.1: Summary of the PHENIX Detector Subsystems [37].

| Element                        | $\Delta\eta$               | $\Delta\phi$          | Purpose and Special Features  |
|--------------------------------|----------------------------|-----------------------|---|
| Magnet: central (CM)           | $\pm 0.35$                 | $360^\circ$           | Up to 1.15 T·m.   |
| muon (MMS)                     | -1.1 to -2.2               | $360^\circ$           | 0.72 T·m for $\eta = 2$   |
| muon (MMN)                     | 1.1 to 2.4                 | $360^\circ$           | 0.72 T·m for $\eta = 2$   |
| Silicon (MVD)                  | $\pm 2.6$                  | $360^\circ$           | $d^2N/d\eta d\phi$ , precise vertex, reaction plane determination   |
| Beam-beam (BBC)                | $\pm(3.1 \text{ to } 3.9)$ | $360^\circ$           | Start timing, fast vertex.  |
| NTC                            | $\pm(1 \text{ to } 2)$     | $320^\circ$           | Extend coverage of BBC for p-p and p-A.   |
| ZDC                            | $\pm 2 \text{ mrad}$       | $360^\circ$           | Minimum bias trigger.   |
| Drift chambers (DC)            | $\pm 0.35$                 | $90^\circ \times 2$   | Good momentum and mass resolution,<br>$\Delta m/m = 0.4\%$ at $m = 1 \text{ GeV}$ .   |
| Pad chambers (PC)              | $\pm 0.35$                 | $90^\circ \times 2$   | Pattern recognition, tracking for nonbend direction.  |
| TEC                            | $\pm 0.35$                 | $90^\circ$            | Pattern recognition, $dE/dx$ .  |
| RICH                           | $\pm 0.35$                 | $90^\circ \times 2$   | Electron identification.  |
| ToF                            | $\pm 0.35$                 | $45^\circ$            | Good hadron identification,<br>$\sigma < 100 \text{ ps}$ .  |
| T0                             | $\pm 0.35$                 | $45^\circ$            | Improve ToF timing for p-p and p-A.   |
| PbSc EMCal                     | $\pm 0.35$                 | $90^\circ + 45^\circ$ | For both calorimeters, photon and electron detection.   |
| PbGl EMCal                     | $\pm 0.35$                 | $45^\circ$            | Good $e^\pm/\pi^\pm$ separation at $p > 1 \text{ GeV}/c$ by EM shower and $p < 0.35 \text{ GeV}/c$ by ToF. $K^\pm/\pi^\pm$ separation up to 1 GeV/c by ToF. |
| $\mu$ tracker: ( $\mu$ TS)     | -1.15 to -2.25             | $360^\circ$           | Tracking for muons.   |
| ( $\mu$ TN)                    | 1.15 to 2.44               | $360^\circ$           | Muon tracker north installed for year-3   |
| $\mu$ identifier: ( $\mu$ IDS) | -1.15 to -2.25             | $360^\circ$           | Steel absorbers and Iarocci tubes for   |
| ( $\mu$ IDN)                   | 1.15 to 2.44               | $360^\circ$           | muon/hadron separation.   |

and populated with the particle detectors for precise measurement of electrons, photons, and charged hadrons. Two Muon Arm detector subsystems (referred to as South and North) measure the muon and decay hadrons yield at forward and backward rapidity region ( $\eta \in (-2.25, -1.15)$  and  $\eta \in (1.15, 2.44)$ ). Global Trigger detectors provide the Level-1 trigger information for the collision by measuring the time and position of the interaction vertex with high precision.

Detector parameters and performance, rapidity and azimuthal angle ( $\phi$ ) coverage, of each subsystem are summarized in Table 3.1.

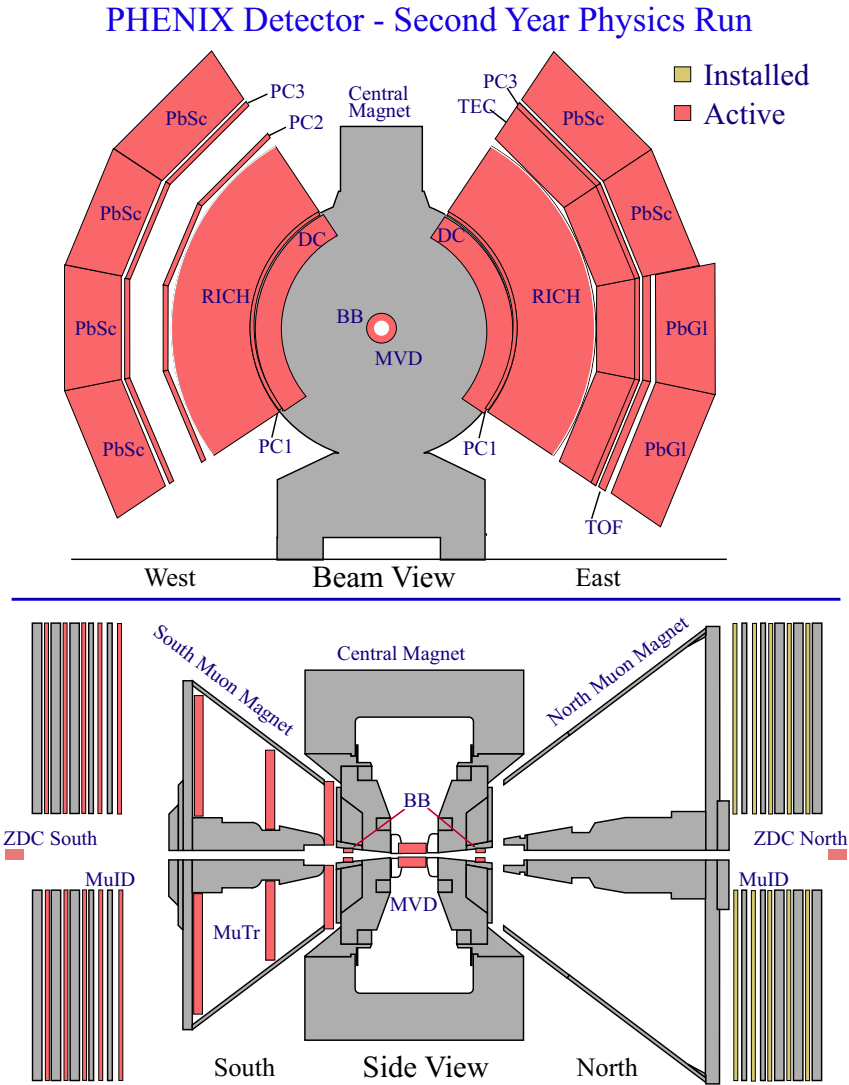


Figure 3.1: Layout for PHENIX Experiment.

We define a coordinate system relative to the beam axis. The origin is located in the center of the IR with the  $Z$ -axis pointing along the beam line from South to North. The  $X$ -axis is points horizontally from East to West and the  $Y$ -axis points upwards, making a proper right-handed coordinate system.

## 3.2 Global Detectors

Nuclear collisions are characterized by their impact parameter vector (both magnitude and direction). Both of these parameters can be determined with reasonable collision on a event-by-event basis. Nearly all physics measurements are then studied to determine their variation with respect to these so-called “global” characteristics of the event.

“Global” detectors measure global characteristics of the collisions and issue online trigger decision to read-out the information. In PHENIX this task has been principally accomplished by two subsystems: the **Beam – Beam Counters** (BBC) and the **Zero Degree Calorimeters** (ZDC). The BBC consists of a set of two (South and North) fast trigger counters providing information about  $Z$  vertex position and collision time with respect to the RHIC beam crossing clock ( $t_{0\text{ BBC}}$ ). The ZDCs are a set of two Tungsten calorimeters (South and North) located far from the collision point and providing additional information about the impact parameter of the collision. The third global detector is the **Multiplicity Vertex Detector** (MVD), a silicon barrel detector designed to measure  $d^2N/d\eta d\phi$  distribution for charged particles near the collision point. This detector is not yet functioning reliably and was not used in my analysis.

### 3.2.1 Beam-Beam Counter-BBC

The BBC consists of two sets of quartz tube Cerenkov arrays, which measure relativistic charged particles produced in narrow cone around each beam axis ( $3.0 \leq \eta \leq 3.9$ ,  $2\pi$  in  $\phi$ ). Positioned at 1.4 m from the PHENIX center point it has an outer radius of 30 cm and inner radius of 5 cm (see Fig. 3.2).

Each BBC counter consists of 64 photomultiplier tubes (schematically shown in Fig. 3.3) equipped with quartz Cerenkov radiators in front. The dynamic range of each tube of the BBC allows to register 1-30 minimum ionizing particles which makes it the main Minimum Bias trigger detector in PHENIX for any collision species.

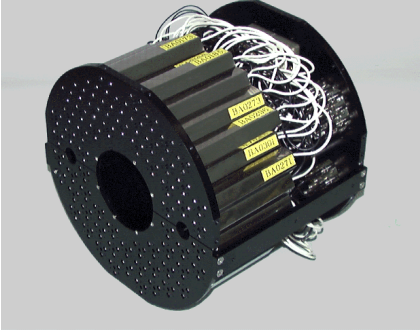


Figure 3.2: Picture of BBC barrel before the installation.

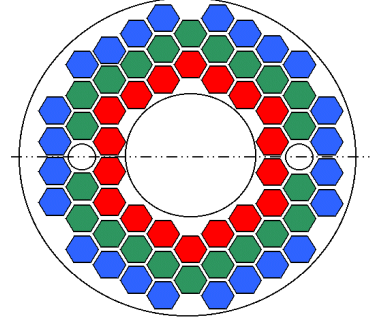


Figure 3.3: Structural drawing of one BBC (beam view). Each box corresponds to one PMT.

Each BBC PMT has intrinsic timing resolution of  $\sigma_t = 50$  ps and provides high precision measurement of collision time and vertex position. For each collision, the BBC measures time of the collision with respect to the RHIC collider clock (synchronized with beam bunches). This time is usually referred to as the **BBC t-zero** and is one of the fundamental items of information about the collision in that it sets the start time for all the subsystems performing timing measurements.

$t_0^{BBC}$  is calculated as a half sum of average hit time over individual BBC PMTs (denote as  $t_N^{BBC}$ ,  $t_S^{BBC}$  for North and South detector). Obviously, vertex position can be calculated as a half difference of those variable.

$$t_0^{BBC} = (t_N^{BBC} + t_S^{BBC})/2; \quad Z_{vtx}^{BBC} = (t_N^{BBC} - t_S^{BBC})/2c \quad (3.1)$$

The vertex resolution in  $p + p$  collisions can be evaluated from the assumption that the multiplicity in the BBC is small and we have one hit in each BBC. Using Eq. 3.1, we can estimate in this case that  $\sigma_Z = \sigma_t/\sqrt{2}c \approx 1.2$  cm. In central  $\sqrt{s}$  collisions, accuracy of vertex measurement becomes much better ( $\sigma_Z \leq 0.3$  cm) due to the averaging effect over all PMTs improves the timing resolution significantly.

The BBC timing is an essential input to Level-1 trigger providing online information about the vertex of the collision. Level-1 trigger electronics, generate trigger accept signals if the vertex lies within  $\pm 50$  cm from the PHENIX center point (to remove beam gas interactions and interactions inside the magnet poles). This method enables the experiment to obtain a clean sample of events. Since the BBC trigger is efficient for a wide variety of interaction processes, it is referred to as a so-called “Minimum Bias” trigger.

### 3.2.2 Zero Degree Calorimeter

The Zero Degree Calorimeter is a small area hadron calorimeter positioned  $\approx 18$  m from the interaction point along the beam axis. The main purpose of ZDC is measurement of the spectator neutron rate in nucleus-nucleus collisions. Spectator protons and other charged particles produced in the collision bend in the magnetic field of RHIC dipole magnets and miss the ZDC acceptance. By measuring the flux of neutrons in heavy ion collision in correlation with the charged particles multiplicity in Beam-Beam counter, PHENIX obtains an information about the impact parameter on the collision (typically called the collision's "centrality"). A single ZDC counter consists of 3 modules each with a depth of two hadronic interaction lengths and read out by a single PMT. The ZDC provides timing and amplitude information similar to the BBC but with decidedly lower resolution. The energy resolution at the one neutron peak is approximately 21% [38, 39]. In Au+Au collisions the ZDC is an important part of Minimum Bias trigger, but in case of  $p + p$  collisions, presented in the analysis, it has no particular use since there are no spectator neutrons.

Fig. 3.4 shows schematic view of ZDC detector. One can also see the projected trajectory for Au ions, spectator protons and neutrons at the ZDC placement plane A – A.

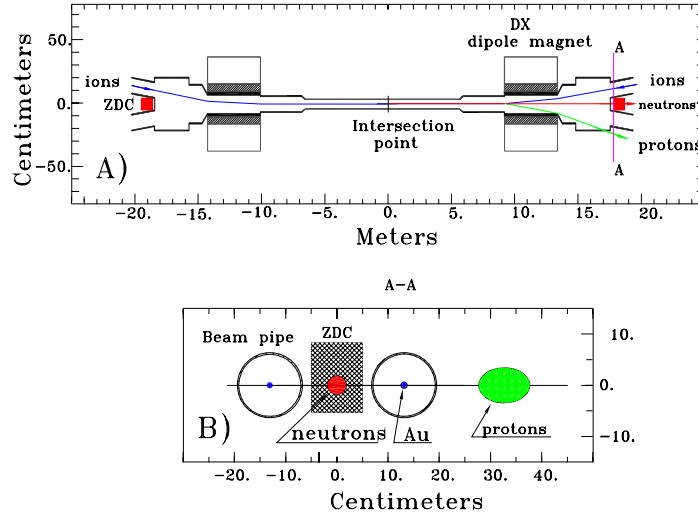


Figure 3.4: Schematic view of ZDC detector. A) Top view of interaction region. B) Projected proton and neutron deflection area at ZDC placement plane.

### 3.3 Central Arm Detectors

The Central Arm detectors provide unambiguous measurements of charged particle track information in mid-rapidity range ( $|\eta| < 0.35$ ). The track's momentum is determined by measuring its deflection angle in the magnetic field of the **Central Magnet** by the multi-wire **Drift Chamber** (DCH). A set of three **Pad Chambers** (PC1, PC2, PC3) helps to reconstruct the  $Z$  information of the track and remove the background tracks. The **Ring Image Cherenkov** detector (RICH) is essential for electron identification and provides good  $e/\pi$  separation for  $p_T < 4.8$  GeV/c. Finally, the **Electromagnetic Calorimeter** (EMC) measures the energy, deposited by the charged particle or photon. The EMC also provides significant hadron/electron separation, crucial for electron analysis.

The central arm subsystems are the most essential component of my electron analysis and the final results rely on the stable performance of all of the described detectors.

#### 3.3.1 Central Magnet

Although the Central Magnet (CM) is not a detector subsystem, central arm tracking relies on its stable operation. The Central Magnet consists of two coils (outer and inner) embedded into the massive steel yolk that generate an axially symmetric magnetic field in the region close to the interaction point. A picture of the CM during production is shown in Fig. 3.5 and the cross-section schematic drawing is shown in Fig. 3.6.

The main requirements to the Central Magnet listed below:

- Provide an smoothly varying magnetic field that can be mapped with 0.2% precision.
- Two coil operation, enabling creation of zero field at  $R = 0$  region in case of opposite coil polarization.
- Minimal material in the PHENIX Central Area detector acceptance in order to minimize photon conversion background.
- Magnetic Field strength should be significantly lower in the region of tracking detectors ( $R > 200$  cm). This allows to assume a straight track model for tracking.
- Movable configuration of the magnets in order to simplify detector assembling and commissioning.

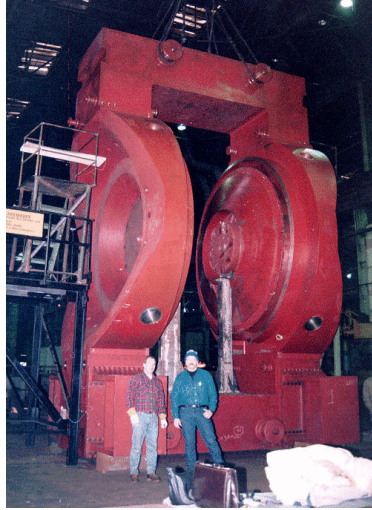


Figure 3.5: Central Magnet during assembly (Izhorskiy plant, St. Petersburg, Russia).

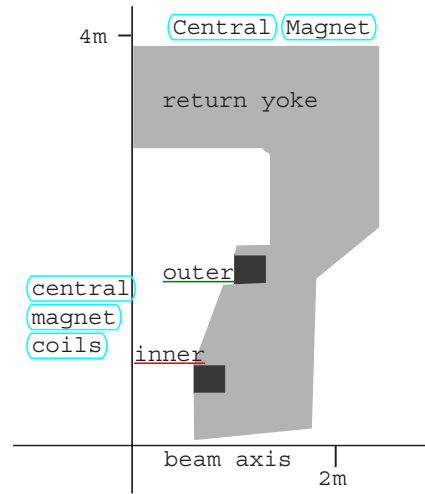


Figure 3.6: Crosssection view of Central Magnet coils and yolk.

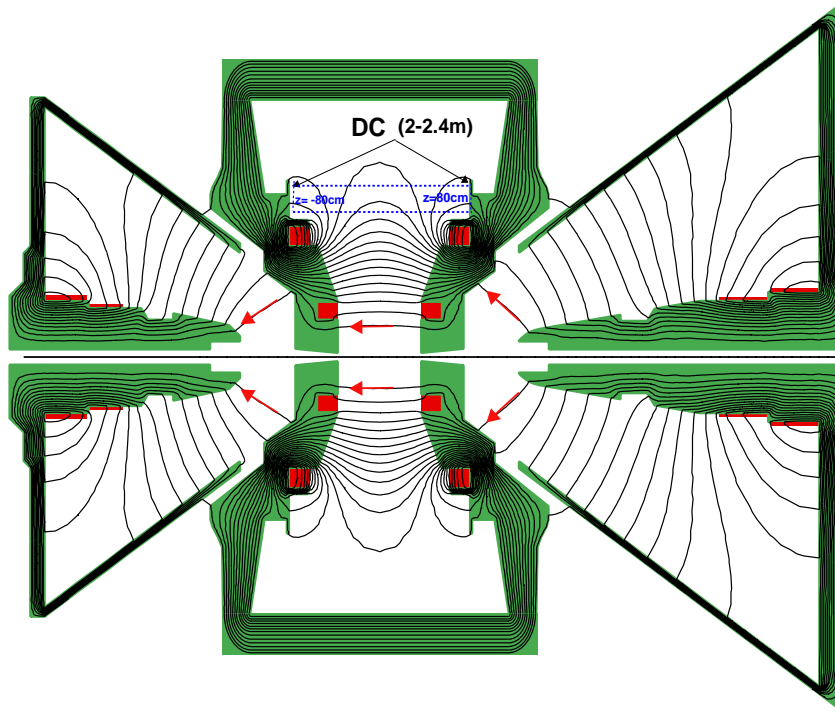


Figure 3.7: Magnetic field lines in PHENIX Magnet System. Drift Chamber location is shown by dashed box.



All the tasks listed were successfully accomplished, the magnetic field line contours in PHENIX Magnet system are shown in Fig. 3.7. Magnetic field strength as a function of radial distance  $R$  on  $Z = 0$  plane for different polarization of “outer” and “inner” magnetic coil is shown in Fig. 3.8. During Run02 PHENIX running period, used for this analysis, only the “outer” coil was energized which lead us to effective field integral for the charged track  $\int B dx = 0.78 [T \cdot m]$ . An additional “inner” coil used in later runs helps to create an even stronger magnetic field in the acceptance in order to improve the momentum resolution for high  $p_T$  tracks.

The field reaches 0.096 T (0.048 T) at the DCH inner and outer radius at  $Z = 0$  and reach even smaller values at  $|Z| = 80$  cm which allows us to assume straight track in the DCH drift volume.

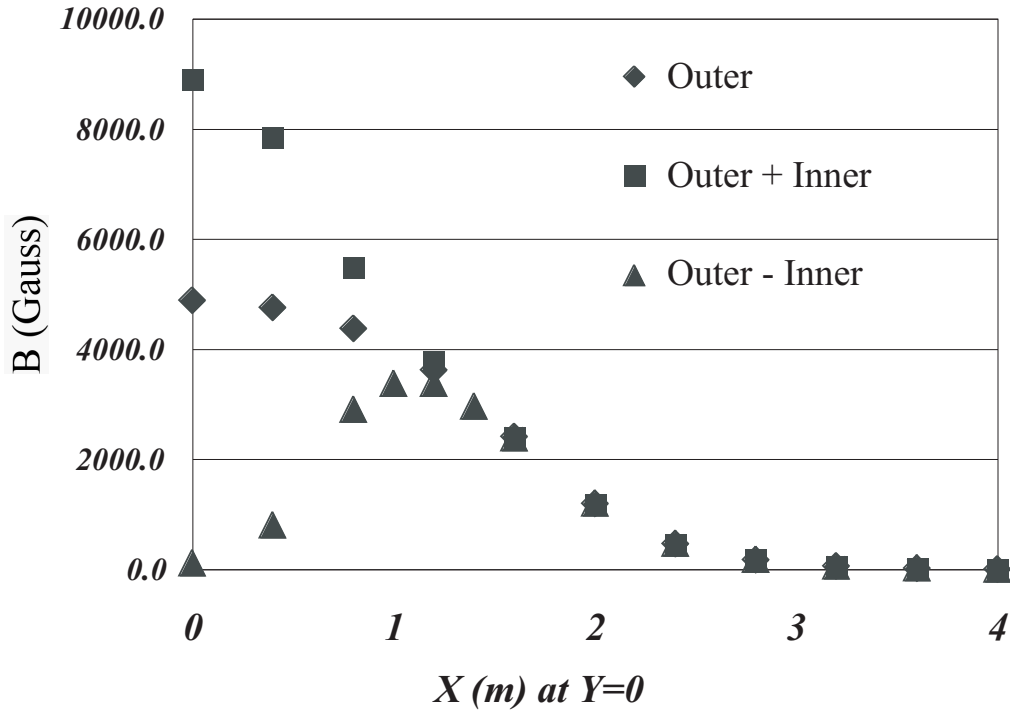


Figure 3.8: Magnetic field strength as function of radius for three different configurations of the magnetic coil polarizations.

### 3.3.2 Drift Chamber

PHENIX Drift Chamber system contains a set of two “jet”-type multiwire detectors and is the main tracking device in PHENIX. It is placed at a radius of  $R \in (202; 246)$  cm and consists of two identical arms each of which cover  $90^\circ$ . The DCH performs the following tasks:

- Accurate measurement of charged particle tracks in  $r$ - $\phi$  plane for determination of their transverse momentum  $p_T$ .
- Measure  $Z$  and  $\theta$  (inclination angle of the track with respect to Z axis) of the charged particle tracks together with PC1 and BBC.
- Provides input information for global tracking in PHENIX.

During the construction of the Drift Chamber the following design requirements have been applied [37]:

- Single wire resolution better than  $150 \mu m$  in  $r$ - $\phi$  direction
- Single track reconstruction efficiency better than 99%
- Two track resolution better than  $1.5 mm$ .
- Spacial resolution in the  $z$  direction better than  $2 mm$ .

In order to reach the specifications, the following design concept was implemented. A cylindrically shaped  $Ti$  frame was built as the support for wire nets with inner and outer radii of 202 and 246 cm and a length of 180 cm. A schematic view of one of the DCH arms is shown in Fig. 3.9. The active volume of the DCH is filled with Argon(50%)/Ethane(50%) gas mixture at STP. Charged particle tracking is done by a set of wire nets placed inside the gas volume of the chamber. There are total of 80 identical wire structures called nets around the azimuthal angle. Each net covers  $1.125^\circ$  in azimuth and is designed to measure the position of the track within its coverage by measuring the **drift time** ( $t_{dr}$ ) of the charge clusters, ionized by the incoming charged particle in the vicinity of the sense (anode) wire.

The wire nets are subdivided into 6 separate sections along the radius, named in the following order (from inside to outside radius) X1, U1, V1, X2, U2, V2. Each X wire net consists of 12 anode wires and measures the track trajectory in  $r - \phi$  plane. Each U, V net has 4 sense wires and designed to reconstruct  $Z$  information for the track. Groups of 4 wire cells share the same electronics set and high voltage supply. Such a grouping is called a **keystone**. Fig. 3.10 shows the net configuration within one keystone.

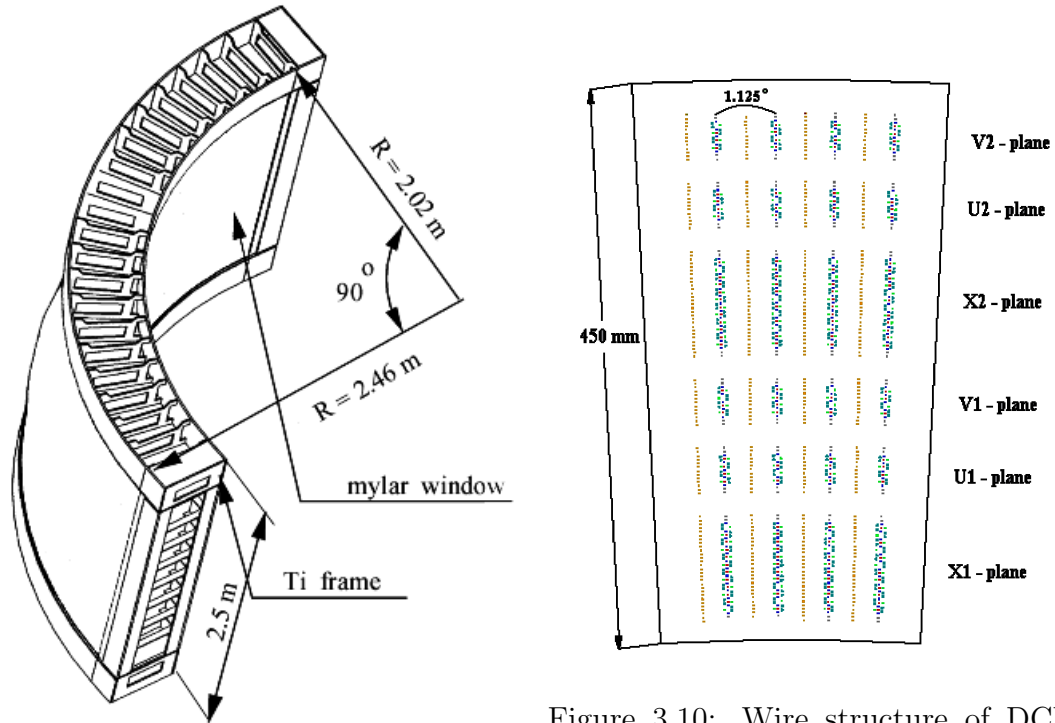


Figure 3.10: Wire structure of DCH Keystone.

Figure 3.9: Schematic drawing of one Drift Chamber Arm.

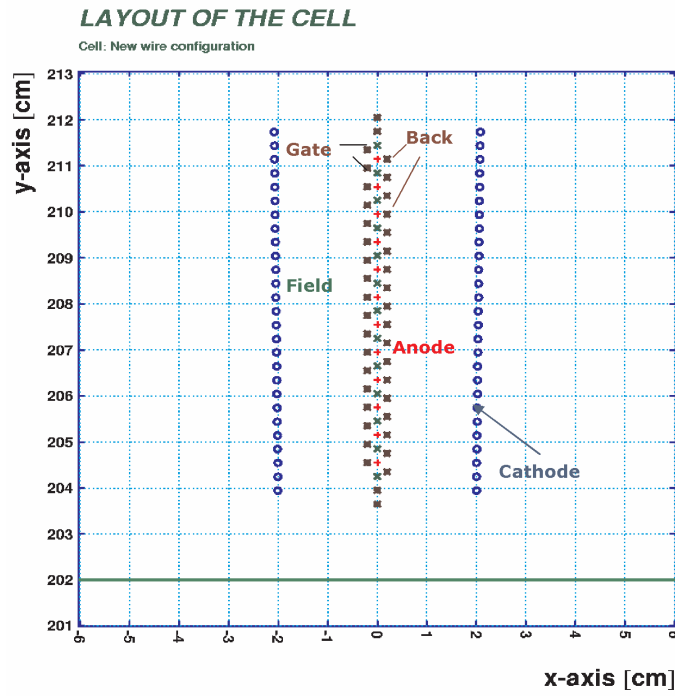


Figure 3.11: Layout of the wire structure of X1 cell.

One cell consists of an anode wire net, surrounded by a pair of cathode nets. The region of  $\approx 2$  cm between cathode and anode net is called drift region or charge collection region. Fig. 3.11 shows the wire structure of X1 wire cell.

The wire nets have a complicated wire and high voltage configuration in order to create a specially tailored electric field in the drift region. In total 5 different values of high voltage are applied to different wires in order to create a narrow and isochronous alley in the drift region that supplies charge to the anode wire as shown in Fig. 3.11. The 5 voltages are named for the drift characteristic they control:

- “Anode” (sense) wires - Read-out the charge, induced by drifting ion current.
- “Cathode” wires - Create uniform electric field in the drift region ( $V_C \approx -4100$  V).
- “Back” wires - Block charge drift from one side of the anode wire to solve left-right ambiguity ( $V_B \approx -850$  V).
- “Gate” wires - Create a localized isochronous charge collection region and increase the field strength close to the anode wire ( $V_G \approx -2000$  V).
- “Field” wires - Separate individual anode wires drift regions and create a strong electric field around the anode wire ( $V_F \approx -2000$  V).

As a result, the electric field, created within one cell generates a well-localized charge collection region directed to one side of the net for odd anode wires and to the opposite side for the even wires. Fig. 3.12 illustrates GARFIELD [41] simulation of the regions which allow the ionized charge (dots) to drift to the anode wires.

The **drift velocity** ( $v_{dr}$ ) within the drift region has a weak dependence on the electric field by the choice of gas mixture and typical field strength. The drift velocity as a function of electric field is shown in Fig. 3.13. The electric field is on the order of  $E \approx 0.8 - 1$  kV/cm in the area between the Gate and Cathode and is significantly higher between the Gate and Anode wire. The average drift velocity in the drift region is on the order of  $\langle v_{dr} \rangle \approx 50 \mu\text{m/ns}$ .

The position of a hit within the cell can be calculated as using  $x - t$  relation:

$$x = v_{dr} \cdot (t_{dr} - t_0) \quad (3.2)$$

where  $t_0$  is an important reference constant, corresponding to creation of the charge in the area of the anode wire.

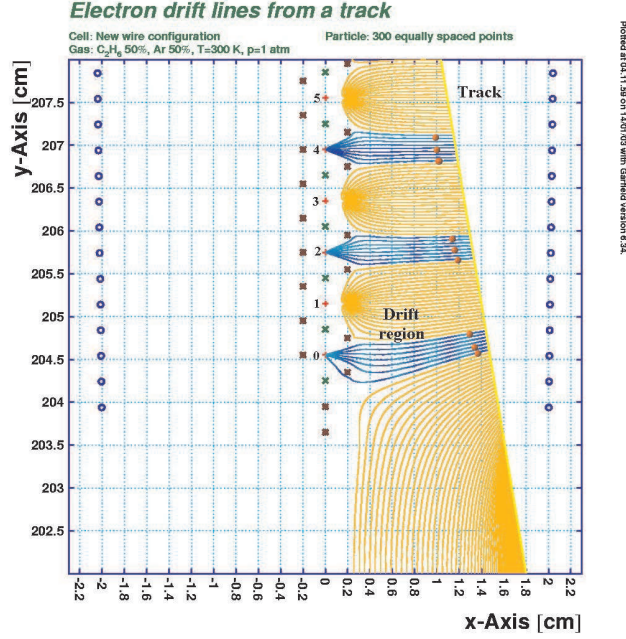


Figure 3.12: GARFIELD simulation of electric field lines inside X1 cell of the DCH. Marked region display the charge collection zone of each anode wire. Circles represents charge clusters drifting towards the anode wire.

Detection of the ionization signal would be impossible using room temperature electronics without **gas amplification**. Electrons travelling in the strong electric field can obtain enough energy between the collisions, to knock-out a secondary electron from a gas molecule, this secondary electron can then knock out another one and so on causing avalanche type multiplication of the charge. The threshold electric field is usually on the order of  $E_{thr} \approx 10 \text{ kV/cm}$  and is reached very close to the anode wire. The electric field in the vicinity of the anode wire can be expressed as  $E = \frac{Q}{r}$  where  $Q$  is a charge per unit length in  $[V] = \frac{[C]}{2\pi\epsilon_0}$ . Using GARFIELD we can simulate the distribution of the charges on each wire for given values of the potentials and wire geometry. From the test runs measurements (see Fig.3.14), it was found that  $Q = 290 \text{ V}$  produce a single wire efficiency of 90 %. The standard voltage configuration was selected so that the charge on all planes exceed this limit.

The DCH Front End electronics digitize the leading and trailing edge of the charge signal using the so-called “ASD-8” chip (Analog - Shaper - Discriminator) [40]. The thresholds for each input channel are set via an eternal DC voltage established by a DAC this is downloaded through an ARCNET net-

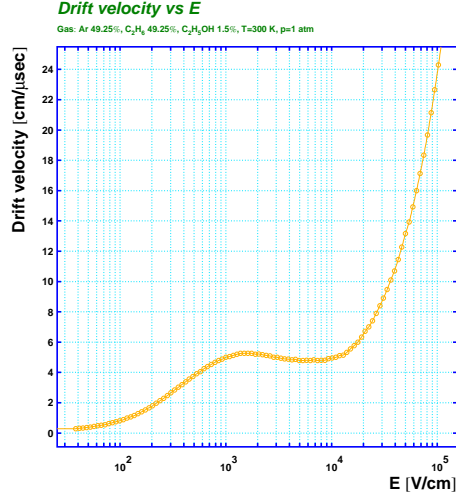


Figure 3.13: Drift velocity as a function of electric field.

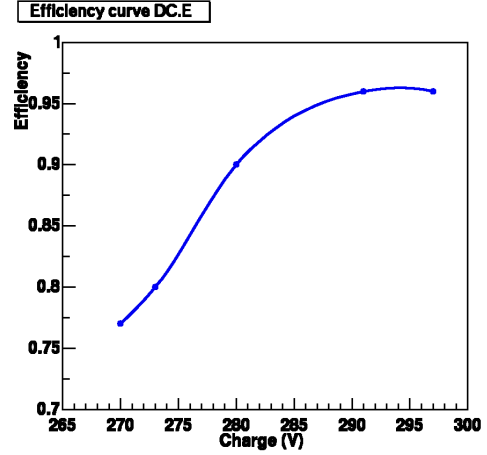


Figure 3.14: Single wire efficiency as a function of charge per unit length  $Q$ .

work. The typical running configuration uses a  $q_{thr} = 6$  fC threshold. The time of the leading edge is being digitized with a granularity of  $\frac{1}{128}^{th}$  of the RHIC clock period or  $\approx 0.8$  ns. , The trailing is digitized with twice coarser binning allowing the pulse width of each trigger to be measured. This measurement is used to reject especially narrow pulses as noise. The “Time Memory Chip” (TMC) functions by storing the continual running history of the leading and trailing edges for the previous  $6 \mu s$  in a circular memory buffer. Triggers force the chip to store one memory frame (an range from the past of user selected delay and depth) into one of 5 static memories. This allows the TMC chip to buffer hits from triggers that occur during the readout of previous data. This nearly eliminates deadtime from the PHENIX data collection system. The value of the “offset” (delay between the real data and the trigger arrival) is selected so that full drift time range could be read-out. Fig. 3.15 shows the typical time distribution shape from the DCH. The left edge of the timing distribution corresponds to the particles, depositing charge close to the anode wire<sup>1</sup>. The right edge of the timing distribution corresponds to the drift time of the electrons from the area of the Cathode wire. By measuring the half height time of the edges of the timing distribution we can make a rough estimation for  $t_0$  and  $v_{dr}$  using Eq. 3.2.

<sup>1</sup>In the region between Gate and Anode wire we do not have Back side cancellation mechanism, this cause apparent double-counting of the signal and left-right ambiguity.

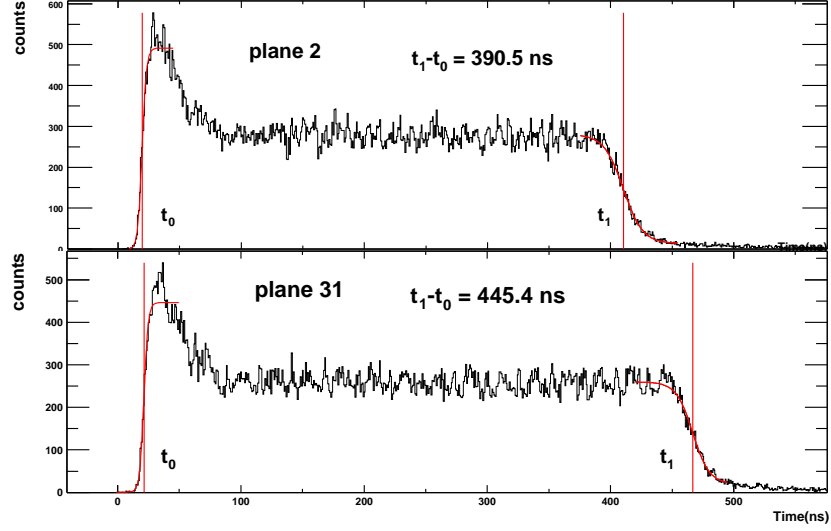


Figure 3.15: Time distribution for two DCH planes. Left and right edges fitted with error function [42].

### DCH fine tuning

It quickly became clear that in order to reach the design resolution, fine tuning of the calibration parameters ( $t_0$  and  $v_{dr}$ ) need to be performed for each wire. This method was called **internal alignment** of the DCH and included:

- Slewing correction - removal of  $t_0$  dependance of the width of the signal.
- $v_{dr}$  channel-by-channel alignment.
- $t_0$  channel-by-channel alignment.

The most appropriate way of performing those type of corrections was based upon **residual** distributions. Residual by definition was denoted as  $\Delta t = t_0 - (t_1 + t_2)/2$  where  $t_0$  is the time of the hit on the trial wire,  $t_1$  and  $t_2$  are corresponding times for the neighboring wires hits. For convenience (as those calculations were performed on-line) the time unit for all time variables is going to be TMC time-bin (1 tb  $\approx 0.8$  ns). Using the straight track assumption, it is clear that in optimal case  $\Delta t$  should be independent of all parameters and have a mean of zero. The side-standing wires (wires at the edge of the cell) have no neighbors and we can not calculate the residuals for them, they play a role of reference wires.

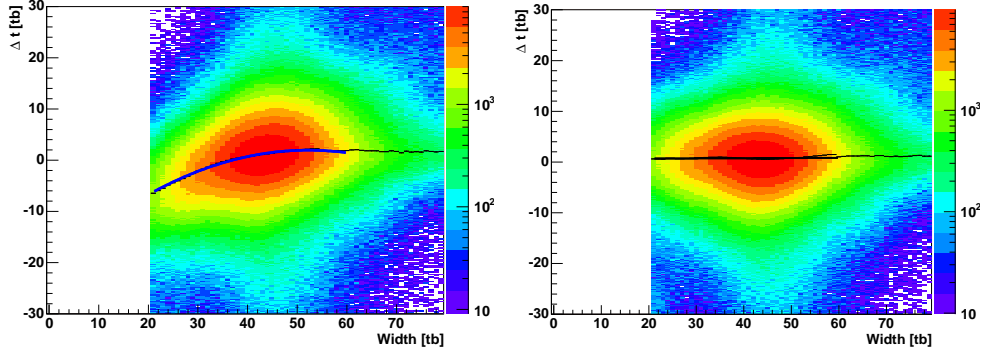


Figure 3.16: Residual distribution as a function of hit width before (left) and after (right) the slewing corrections.

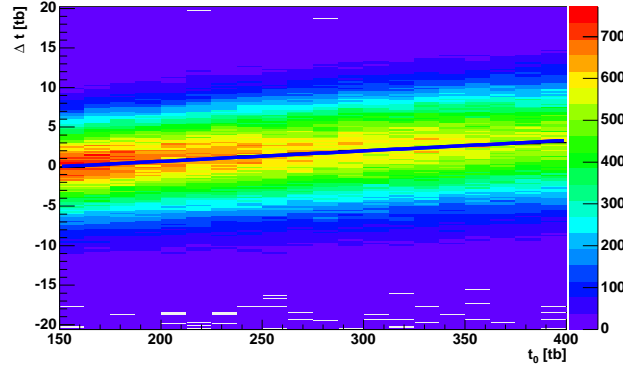


Figure 3.17: Residual as a function of time fitted with linear function.

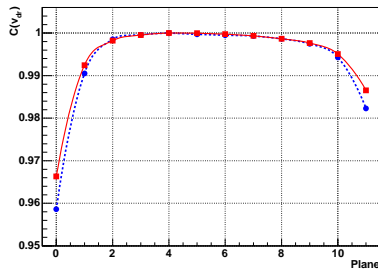


Figure 3.18: Comparison of  $v_{dr}$  for East X1 wires obtained from the data residual slope (circles) and GARFIELD simulation (squares).

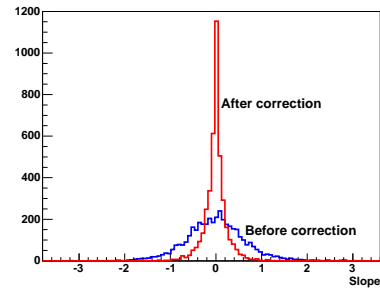


Figure 3.19: Distribution of the residual distribution slopes (see Fig. 3.17) for all the DCH wires before and after drift velocity corrections.



We first look at the dependence of the residual as a function of the hit width (see Fig. 3.16). After including the fitted value of the mean shift as a correction to t-zero  $t_0 = t_0 - dt^{slew}(w)$  and performing at least three iterations we remove the dependence of residual on a hit width.

The Drift velocity can be fine-adjusted using the field-off data. In this case, the majority of the tracks (not coming from decays or scatters) should go radially from the vertex with no deflection angle  $\alpha \approx 0^\circ$ . If we look at the distribution of the residual for particular wire as a function of time (shown in Fig. 3.17), the linear slope of the distribution that can **only** be caused by the difference of the drift velocities between the wire and its neighboring wires. It is possible to solve the corresponding system of linear equations for the corrections to the  $v_{dr}$  variations with respect to the reference drift velocity. The solution require two constrains which can be selected arbitrarily. The best choice for choosing the constraints is by comparing the results of the corrections to the variation of  $x-t$  relation slope from GARFIELD simulation. Fig. 3.18 shows the comparison of drift velocity profile obtained from data with the one produced from GARFIELD code. One can see nice agreement between expectation and the measurement. This method was performed on the plane-by-plane basics, the second order wire-by-wire corrections have been performed as a perturbation to the plane-by-plane corrections. Comparison of the individual wire slopes after wire-by-wire fine tuning of the drift velocity is shown in Fig. 3.19. The final set of  $v_{dr}$  correction coefficients was recorded as a multiplier for the global drift velocity, measured from the edges of the timing distribution.

Fine adjustments to the calibration parameters were also performed on the  $t_0$ . Similar to the drift velocities,  $t_0$ s have strong dependence on the plane (probably due to the combined effect of the  $x-t$  relation non-linearity and the propagation time of the signal on the ASD board). It also has a strong variation on the wire-by-wire basis due to possible geometrical displacement (driven by electrostatic sag) of individual wires and possibly different gas gain. The wire-by-wire variation of  $t_0$  was applied as an additional correction on top on plane-by-plane correction.

In order to estimate the plane-by-plane variation of  $t_0$ , the rising edge of the timing distribution was fitted at the constant level (1% - 5% of the maximum) as shown in Fig. 3.20. The results of the fit do not depend on the fit level (except for constant shift of the resulting time) and behavior is similar for both DCH arms (see Fig. 3.21).

The local wire-by-wire  $t_0$  fine tuning was done plane by plane using the side-standing wires as a references and moving the middle wires  $t_0$  in order to zero the mean of the residual. The problem is easily reducible to a set of

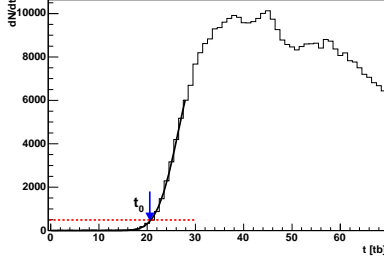


Figure 3.20: Determination of  $t_0$  from the slope of timing distribution at constant height for one DCH plane. Slope is fitted by Error function.

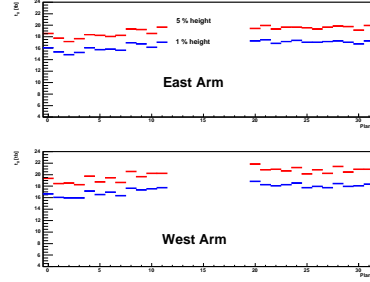


Figure 3.21: Comparison of plane-by-plane  $t_0$  corrections for different DCH arms and different height cut.

linear equations for  $dt_0_i$  as a function of  $\Delta t_0_i$ .

After all the corrections are applied, the residuals distribution of the hit to the track reaches the design values of  $\approx 150\mu\text{m}$  which is shown in Fig. 3.22 for both DCH arms. If we only look at the tracks far from the anode and cathode, this value can go down to  $\approx 100\mu\text{m}$  - which is probably the physical limitation due to the cluster arrival time smearing and the gas diffusion coefficient. Needless to say that this value only indicates the relative accuracy of the tracking within one cell, data-based geometrical alignment of the nets within the DCH and matching to the outer detectors and vertex need to be done in order to perform **global alignment** of the Drift Chamber [42].

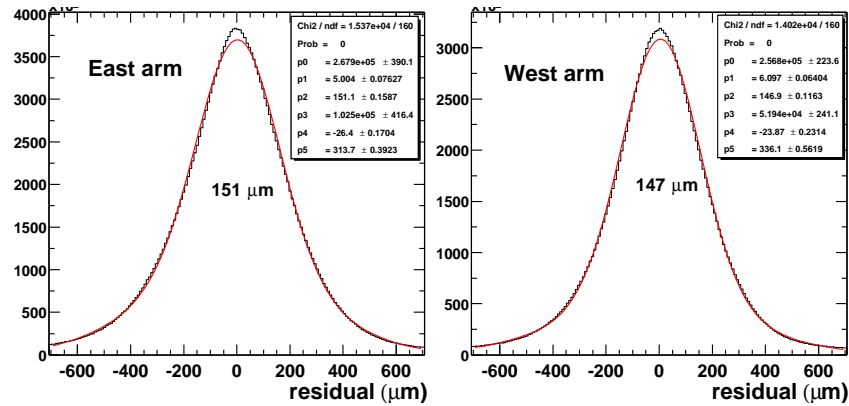


Figure 3.22: Residual distribution of the hit to the track for East (left panel) and West (right panel) DCH arm fitted with double-gaussian [42].

## Tracking algorithm

Tracking is the most critical step of the particle identification. Not only must the tracking operate with high single track reconstruction efficiency, but also it needs to be reliable in the high multiplicity environment of central  $Au + Au$  collisions and have a low “ghost” track rate.<sup>2</sup> The rate of the “ghost” tracks can be later reduced by association to other detectors (PC2, PC3, EMC).

Much of the tuning to optimize the tracking performance was performed by me and I will summarize the key features of the method in this chapter.

The ideal track (meaning 100 % single wire efficiency) should leave at least 6 hits in X1 section and 6 hits in the X2 section of the DCH. In reality, inefficiencies cause the track to lose hits with a certain probability. The single wire efficiency can be calculated for each wire using the ratio of tracks, having a hit on this wire within some wide association window to the total number of tracks passing within that wire’s active area. In order to remove the complications of the cathode or anode crossing tracks, only the region confined close to the center of the cell is used for this calculation. The final efficiency map for  $p + p$  Run02 is shown in Fig. 3.23. One can see that the single wire efficiency is on the order of 95% for the middle wires and on the order of 90% for the side-standing wires (especially closest to mylar window of the chamber). This effect is well understood and was predicted from the Garfield simulations. It results from “edge effects” that reduce the field and hence the gain on the side-standing wires.

Now we can estimate the tracking efficiency assuming that we consider a track to have at least  $N$  hits in X1 and  $N$  hits in X2 for a given (constant) level of single wire efficiency. This can be exactly calculated using probability theory, the results of calculations for  $N = 4, 5, 6$  are shown in the Fig. 3.24. This plot show that having 95% single wire efficiency we already at the region of  $> 99\%$  tracking efficiency if we chose  $N = 4$  which was chosen as a minimum number of hits in X1 or X2 layer for the track.

The tracking in PHENIX is based on the assumption of the track having a straight line trajectory inside the Drift Chamber volume. First, the track is reconstructed in  $X - Y$  plane projection, determining  $\alpha$  and  $\phi$  angles of the track, defined as indicated in Fig. 3.25.

First stage of the trackfinding utilizes the **“combinatorial hough transform”** algorithm. Basic idea of the “combinatorial hough transform” is very

---

<sup>2</sup>Ghost tracks are pattern recognition solutions that did not actually come from real tracks.

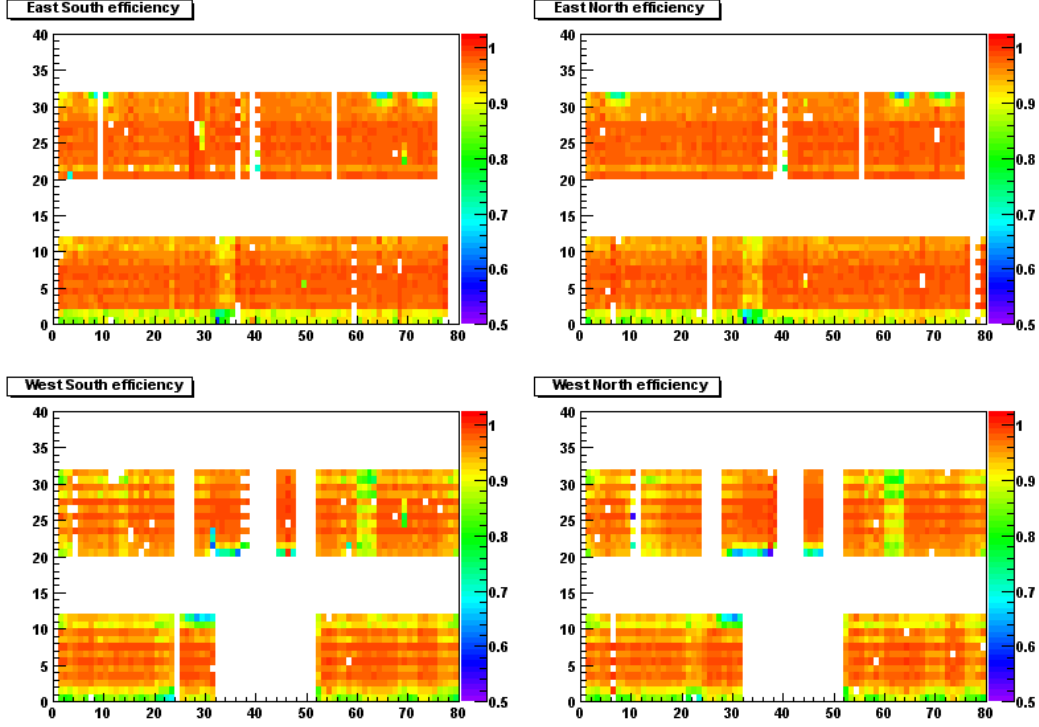


Figure 3.23: Single wire efficiency map for  $p + p$  Run02.

simple: we are looking for a straight tracks, having X1 and X2 hits. Every straight line is described by two parameters ( $y=mx+b$ ), both of which can be determined by any set of two points lying along the line. If we make all possible combinations between each X1 and each X2 hit (laying within reasonable vicinity range from each other) we can calculate and histogram the line parameters. The line parameters ( $m, b$ ) have infinite bounds and are impractical to histogram, so we instead calculate, for each pair, the local angles  $\alpha_p$  and  $\phi_p$  (same notation as on Fig. 3.25) to fill a 2-D histogram of  $\alpha_p$  vs.  $\phi_p$ . As the result - all the pairs of hits belonging to one track will create a localized peak on this histogram. The histogram can be replaced by 2-D array, which is called “hough array” and the local maxima in this array provide a “guess” value for  $\alpha$  and  $\phi$  of a track. In order to remove the possible bin-edge effects, a threshold is applied to the 3x3 bin sum around the local maximum of the “hough array” elements. This way we are able to clearly separate the background random combinations from the real tracks. to improve the initial guess parameters, we use weighted average of the neighboring array bins to improve the initial guess for  $\alpha$  and  $\phi$ .

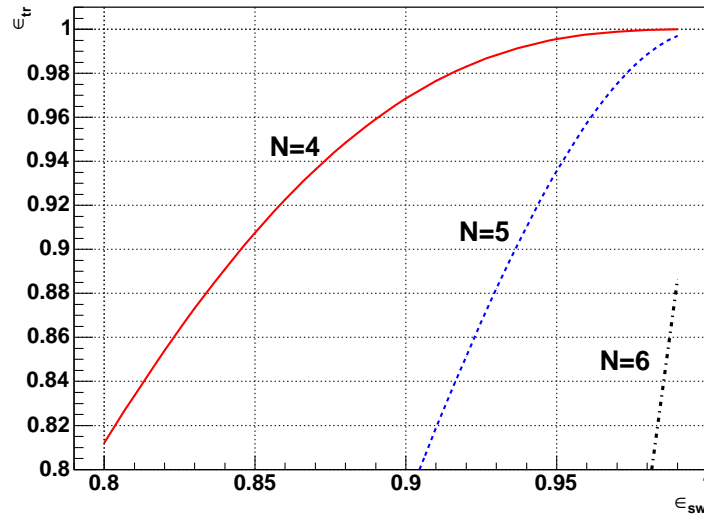


Figure 3.24: Tracking efficiency as a function of single wire efficiency for different requirement on the number of hits in X1 and X2 DCH plane.

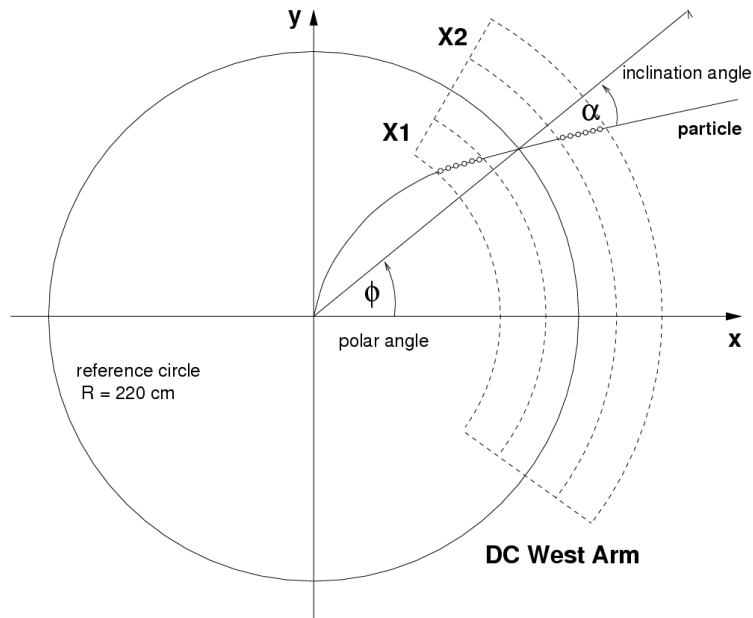


Figure 3.25: Single wire efficiency map for  $p + p$  Run02.

The threshold of the hough array is chosen  $N_{thr} = 15$ , low enough to allow “4 hits in X1 + 4 hits in X2” tracks to survive the cut. The binning of the hough array is also very critical issue: the coarser the binning, the more the probability to have all hits from one track localized to one bin. However if the bins are too coarse the accuracy for the determination of the initial guess parameters is decreased. Making the bins finer also has the drawback that hits from one track start to smear around the bins of “hough array” and the track may fall below the cut threshold. The bin size of the hough array was optimized by studying the reconstruction probability of one chosen track in high multiplicity  $Au + Au$  events (worst case scenario). It does not matter at this stage whether we have a lot of background tracks, it is more important not to lose any.

The next step of the trackfinding - is a “gentle” removal of the background:

- Association of the hits to the track with (*one hit*  $\leftrightarrow$  *many track*) correspondence. The association algorithm calculates the closest approach of the hit to the projected track guess and associates it if the hit is at least 4 mm from the track guess.
- Robust fitting of the track - iterative linear fitting using a weighting the hits, dewatering hits in accordance to their deviation from the mean of the previous iteration. This helps to remove randomly associated hits that are far off from the projected track. 5 fitting iterations performed, gradually rejecting mis-associated hits. Fig. 3.26 shows the track candidates (improved accuracy as compared to track guesses) after the first fitting stage.
- The next step is sequential removal of the excess track candidates. 3 stages of “gentle” removal perform the following procedure:
  1. Associate hits to the track with *one hit*  $\leftrightarrow$  *one track* correspondence. In this step each hit will be associated **only** to the closest track. Association window is 4 mm for 1st and 2nd stage and 2 mm for the final association stage.
  2. Removal of the tracks that have less hits than a threshold  $n_{thr}$  associated.  $n_{thr} = 4$  for the 1st stage,  $n_{thr} = 6$  for the 2nd stage and  $n_{thr} = 8$  for the final stage. This procedure **gradually** removes the tracks that have too few hits associated, returning their mis-associated hits to the real tracks.
- Final fitting of the remaining tracks to the hits. Fig. 3.27 shows the tracks that were filtered to the output. Most all extraneous tracks are

removed by the method which proved to be extremely robust and efficient enabling as to reach  $\approx 75\%$  tracking efficiency in the most central full energy AuAu collisions. In low multiplicity environment of  $p + p$  collision the tracking efficiency exceeds 98%.

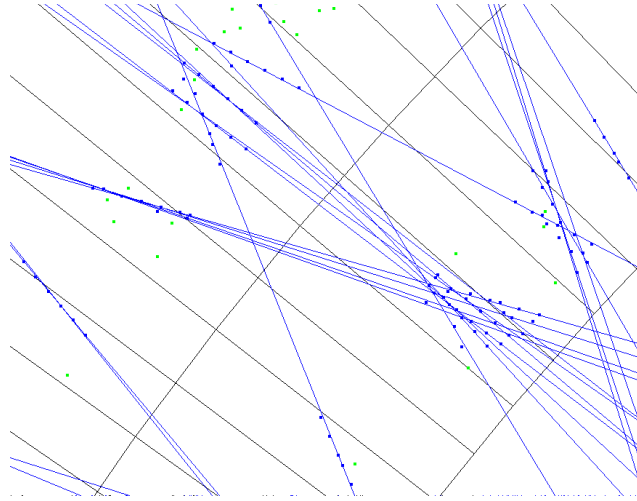


Figure 3.26: Event display snapshot with track candidates after the initial hit fitting.

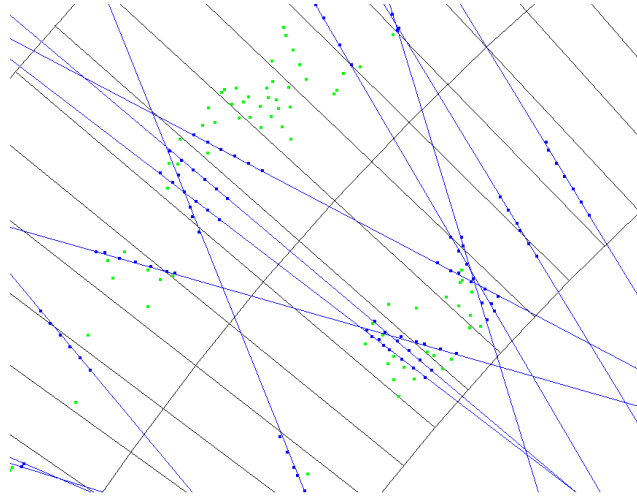


Figure 3.27: Event display snapshot with tracks on the final stage of track-finding. Same event as for Fig. 3.26

### 3.3.3 Pad Chambers

The PHENIX Pad Chambers are unique background rejection devices using a novel pixelation scheme. Their primary purposes are following [37]:

- Measurement of non-projective three dimensional spatial points, which are used for both momentum determination ( $p_z$ ) and pattern recognition.
- Rejection of decays and photon conversion background at high  $p_T$  by tight matching requirements to the tracks measured by the DC.
- Distinguishing electrons from other particles by accurate pointing of charged track to the RICH and EMC.
- Charged particle veto in front of EMC.
- Providing seed for tracks in charged high  $p_T$  Level-2 triggers and electron Level-2 triggers.

The space points provided by PC3 and EMC allow us to more accurately determine the track's actual trajectory through the RICH, an essential improvement to the electron identification. All  $Z$  information for the track is obtained from PC1 high precision  $Z$  measurement<sup>3</sup>

During the PC design of the following requirements were applied [44]

- Very high efficiency ( $> 99\%$ ) and low occupancy(few % in most central  $Au + Au$  collisions).
- Good spatial resolution.
- Low mass, in order to minimize secondary particle production and multiple scattering.

The PCs are multi-wire proportional chambers placed at radial positions of 2.5m, 4m, and 5m. Each detector contains a single plane of wires inside a gas volume bounded by two cathode planes. One cathode is segmented into an array of interlaced “pixel-pads”. Each track fires three pixelpads. The coincidence reduces the false hit rate to be entirely negligible and localizes the track 3X better than a standard pixel chamber with the same number of channels.

---

<sup>3</sup>The DCH can provide information about  $Z$  of the track using UV layers, but, the accuracy of this measurements is less precise than that provided by PC1 alone.



A schematic view of the PC subsystem is shown in Fig. 3.28. The important PC specifications achieved in RUN-2 are listed in Table 3.2. The pad size for PC1 is  $0.84\text{ cm} \times 0.845\text{ cm}$  to achieve less than 8% occupancy in most central  $Au + Au$  collisions. This gives a position resolution of  $1.7\text{ mm}$  along  $z$  and  $2.5\text{ mm}$  in  $r - \phi$ . The pad size for PC2 and PC3 is chosen such that they have similar angular resolution compared to PC1.

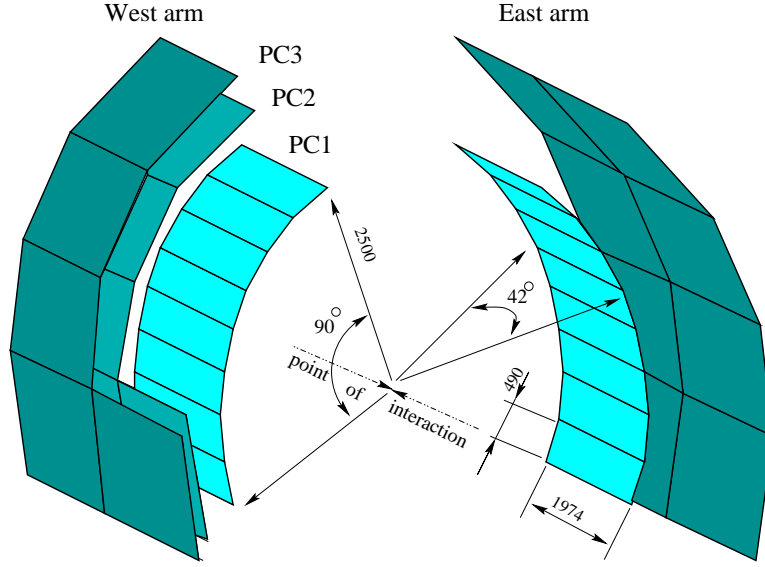


Figure 3.28: Schematic view of PHENIX Pad Chamber set. Several sectors of PC2 and PC3 in the west arm are removed for clarity of the picture. [44].

Table 3.2: Performance of Pad Chambers in RUN-2 [44].

| Parameters   | PC1                 | PC2                  | PC3               |
|--|---------------------|----------------------|-------------------|
| Pad Size ( $r-\phi \times z$ ) [ $cm^2$ ]            | $0.84 \times 0.845$ | $1.355 \times 1.425$ | $1.6 \times 1.67$ |
| Single hit resolution<br>( $r-\phi, z$ ) in [ $mm$ ] | (2.5,1.7)           | (3.9,3.1)            | (4.6,3.6)         |
| Double hit resolution<br>( $r-\phi, z$ ) [ $cm$ ]    | (2.9,2.4)           | (4.6,4.0)            | (5.3,5.0)         |
| Radiation Length [%]                                 | 1.2                 | 2.4                  | 2.4               |
| Efficiency   | >99%                | >99%                 | >99%              |

### 3.3.4 Ring Imaging Cerenkov Detectors

The Ring Image Cerenkov (RICH) detector is the key component of PHENIX leptonic program. Not only does it have a nearly perfect rejection of pions over electrons up to  $p_T \approx 5 \text{ GeV}/c$  ( $1 \times 10^{-4}$  error rate), but it also provides the Level-1 electron trigger decision that enables us to collect rare electron and dielectron events. The main functions of RICH are:

- Identification of electrons below  $p_T < 4.8 \text{ GeV}/c$ .
- Enable charged pion identification at  $p_T > 4.8 \text{ GeV}/c$  [42].
- Provide a fast Level-1 trigger decision. In combination with EMC tile trigger, helps us **significantly enrich** the electron sample in high luminosity  $p + p$  collisions. Unfortunately, electron rate in  $Au$  collisions is too high to make the electron trigger effective.

A schematic view of RICH detector is shown in Fig. 3.29. Each RICH detector has a volume of  $40 \text{ m}^3$ . The spherical mirrors focus Cerenkov light onto two arrays of photomultiplier tubes (PMT), each located on one side of the RICH entrance window. In order to achieve the design requirements, RICH performance has to satisfy the following specifications [37]:

- $e/\pi$  separation at the  $10^4$  level for single tracks.
- The Photo Multiplier Tube (PMT) should have high single photon efficiency ( $> 99\%$ ). It should also have good timing resolution ( $300 \text{ ps}$ ) to reduce noise and contamination from albedo electrons generated during emc showers.
- Minimal radiation length to reduce conversions inside RICH.

The entrance of each PMT features a “Winston cone” of  $50 \text{ mm}$  diameter. The cone funnels light to the tube and increases the active area by reflecting light into the sensitive area of the tube that otherwise would have been missed. Each tube also has a magnetic shield that allows it to operate in magnetic field up to  $100 \text{ Gauss}$ . The radiator gas length seen by electron is  $87 \text{ cm}$  at  $\eta = 0$  and  $150 \text{ cm}$  at  $\eta = 0.35$ , the average path length through radiator gas is  $120 \text{ cm}$ .

The RICH active volume is filled with  $CO_2$  gas at a pressure slightly above atmospheric. The gas has a Cerenkov threshold of  $\gamma_{thr} = 35$  which is about  $17 \text{ MeV}/c$  for an electron and  $4.8 \text{ GeV}/c$  for pion. The RICH can also be used to identify pions at  $p_T > 4.8 \text{ GeV}/c$  [42] Fig. 3.30 illustrates the principle of

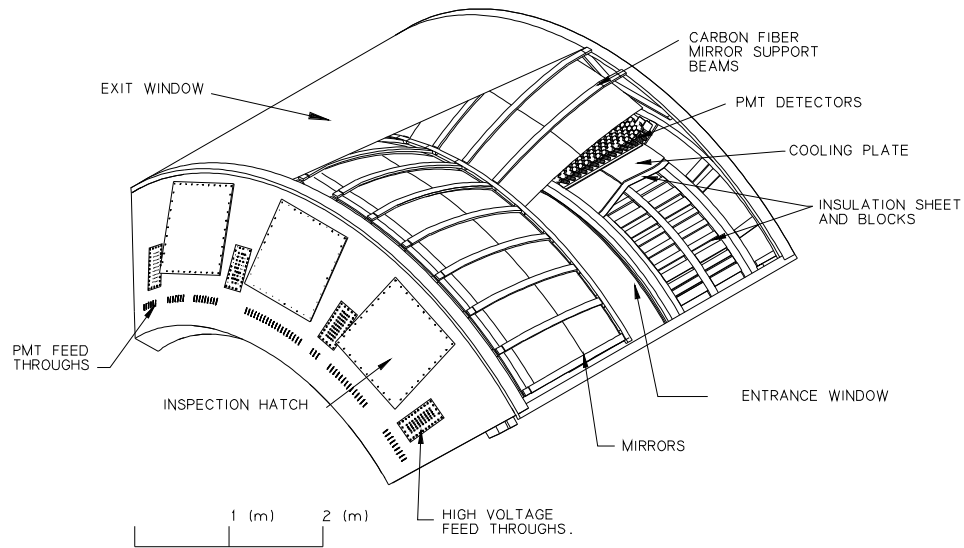


Figure 3.29: A cutaway view of the RICH detector [45].

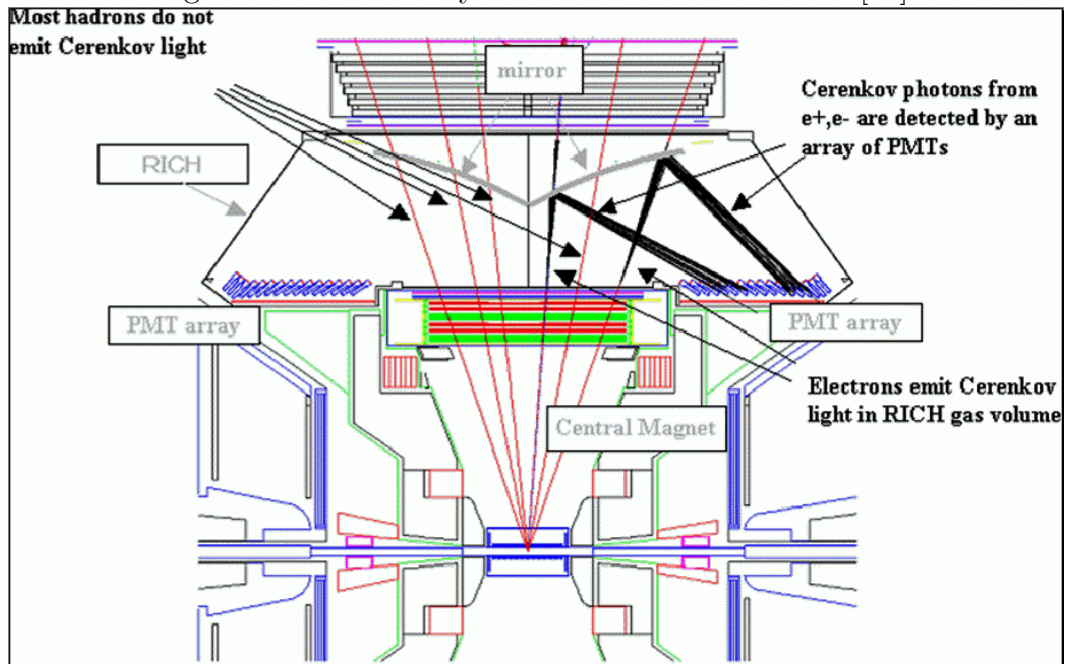


Figure 3.30: Top view of the RICH and its optics. The tracks of the electrons and the emitted Cherenkov light cone are shown. Courtesy of Takashi Hachiya.

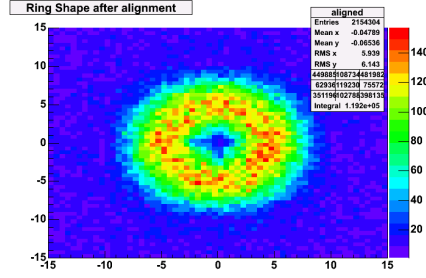


Figure 3.31: Profile of the ring around the projected charged track intersection point. Courtesy of T. Kajihara.

electron detection in the RICH. The Cerenkov photons generated by  $e^+$ ,  $e^-$  and high momentum hadrons are reflected by spherical mirrors placed within the radiator volume. The photons are focused onto PMTs placed just behind the PHENIX central magnet. The pole tips of the magnet thus serve as hadron shields for the PMTs.

Cerenkov photons are emitted at an angle of  $\theta = \cos^{-1}(1/(\beta n))$ . These photons are focused as a ring of photons onto the PMT array,

The total number of photo electrons for a charged particle above the Cerenkov threshold can be written as [9]

$$N_{npe} = L \frac{\alpha^2 z^2}{r_e m_e c^2} \int \epsilon_c \epsilon_d \sin^2 \theta dE \quad (3.3)$$

where  $\frac{\alpha^2 z^2}{r_e m_e c^2} = 370 \text{ cm}^{-1} \text{ eV}^{-1}$ ,  $L$  is path length of particles in the gas volume,  $\epsilon_c$  is the PMT Cerenkov light collecting efficiency and  $\epsilon_d$  is the quantum efficiency of the PMT.

$$\begin{aligned} N_{npe} &= N_{npe}^0 L \sin^2 \theta, \text{ where} \\ N_{npe}^0 &= \frac{\alpha^2 z^2}{r_e m_e c^2} \langle \epsilon_c \rangle \langle \epsilon_d \rangle. \end{aligned} \quad (3.4)$$

which quantifies the RICH electron detection performance. This number takes into account acceptance and quantum efficiency of the PMT and the property of the gas. In RUN-2, it is measured to be  $116 \text{ cm}^{-1}$  for  $\text{CO}_2$  gas.

Each PMT has a diameter of about  $2.5 \text{ cm}$ , while the ring of photons reflected onto the PMT array has a radius of  $11.8 \text{ cm}$ . Fig. 3.31 shows the association of the RICH ring with respect to the incident charged track. The RICH ring can be clearly seen as expected from the ring diameter for  $\text{CO}_2$  gas. To reduce false hit rate, the number of PMTs for a given charged track are counted within  $3.4\text{--}12.8 \text{ cm}$  from the projection - this value is called  $n_0$ .

### 3.3.5 Electromagnetic Calorimeters

The Electromagnetic Calorimeter (EMC) in the PHENIX is used to measure the spatial position and energy of electrons and photons produced in Heavy Ion collisions. EMC also provides the means to trigger on rare events (high  $p_T$  electrons and photons). The hadrons with kinetic energy more than 200 MeV will not deposit significant energy in the calorimeter as the design and the thickness is deliberately chosen to be “uncompensated”. The detector covers the full Central Arm acceptance of  $-0.35 < \eta < 0.35$  and has two arms  $90^\circ$  in azimuth each.

The main specifications to the EMC design are listed below [37]:

- Good energy and position resolution for electromagnetic showers.
- Sub-nanosecond time resolution.
- Comparatively low cost.

To accomplish those goals, the basic design of EMC was selected to consist of 8 large sectors covering in total  $60\text{ m}^2$  of the PHENIX acceptance, 6 of the EMC sectors (E2,E3,W0-3) “**Plumbum-Scintillator**” modules (PbSc) and 2 sectors of “**Plumbum-Glass**” modules (PbGl). The PbGl represents the greatest cost savings since the device was recycled from a previous experiment. The schematic view of the EMC sector is shown in Fig. 3.32. PbGl sectors of EMC were previously used by WA98 experiment and were re-installed in PHENIX. The PbSc sectors was built specifically for PHENIX in 1992 and designed as a set of lead-scintillator sandwich with readout by wavelength shifting (WLS) fibers penetrating the entire length of the detector cell (usually referred to as “tower”). The dimensions of one PbSc tower are  $5.25 \times 5.25 \times 37.0\text{ cm}^3$  and the effective depth of the EMC corresponds to 18 radiation length. The depth is chosen to obtain the optimal  $e/\pi$  separation via  $E/p$  matching. For this analysis we use only PbSc sectors of EMC. Each tower measure the deposit energy of the electromagnetic shower in localized place on the detector surface. This enables us to look for the “**clusters**” of energy, localized to a particular block of towers and measure the total deposited energy under assumption of electromagnetic shower. The electron and photon leave all its energy in the EMC and localized to  $2 \times 2$  towers with 85% probability, making the EMC an unique electron ID device in PHENIX.

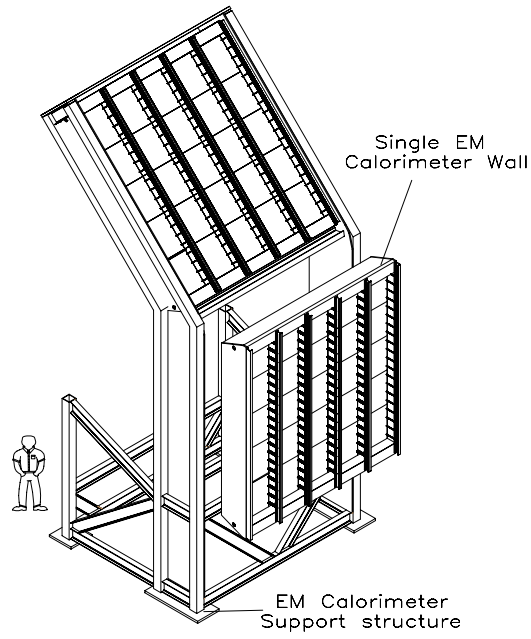


Figure 3.32: Structural design of EMC sector [37].

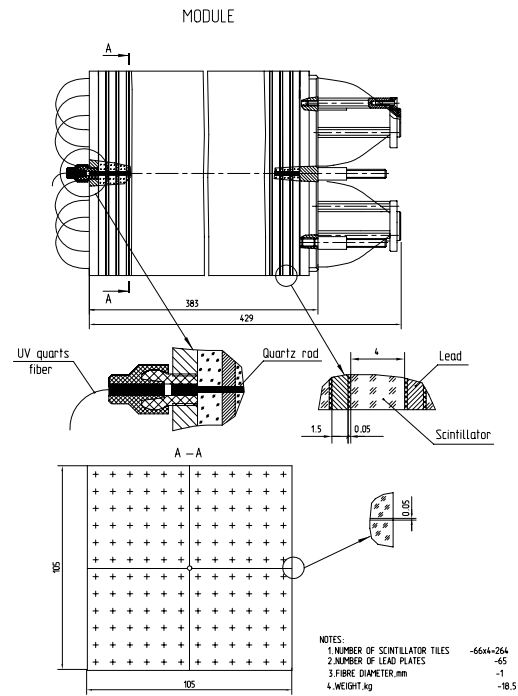


Figure 3.33: Design of PbSc EMC tower [37].

The schematic design of one PbSc tower is shown in Fig. 3.33 there are total of 18240 individual towers in PbSc EMC sectors grouped into 25 “supermodules” each containing 64 towers. The module consists of a stack of alternating layers of 1.5 mm thick layers of lead, white reflective paper and 4.0 mm thick polystyren-based scintillator tiles. Each stack has a drilled array of holes for the WLS fibers with 500 nm emission peak. The light is collected from fibers by a conventional PMT tube at the base of the tower. This design (so called “shish-kebab” type) prove to provide a perfect light collection and perfect time uniformity of the signal. The dynamic range of the PMT was chosen to perform the energy measurements starting from 0.1 up to 50 GeV with good linearity.

The energy resolution of the PbSc EMC was measured on the test beam to be on the order of  $\frac{\sigma(E)}{E} = 1.2 \oplus \frac{8}{\sqrt{E}}\%$  and spatial resolution on the order of  $\sigma(x) = \frac{10}{\sqrt{E(\text{GeV})}}$  mm. Fig. 3.34 shows the energy deposited in the EMC by pion, proton and electron with different particle energy. One can clearly see very good separation of the electrons and hadrons (especially at  $E > 1.0$  GeV) which is the advantage of the electron identification capabilities of the EMC.

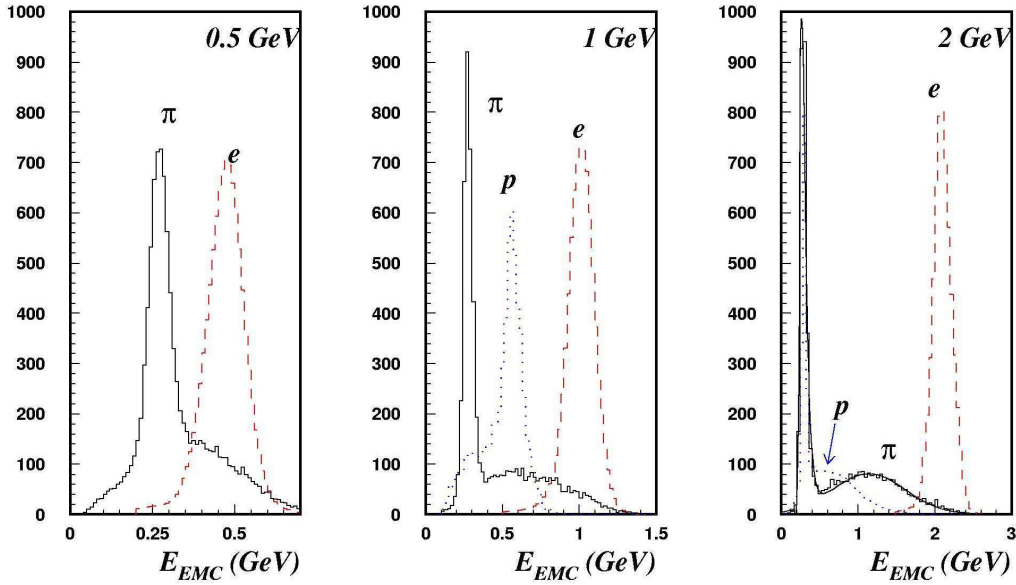


Figure 3.34: Energy deposited in PbSc EMC by the pion, proton and electron of  $E = 0.5, 1.0$  and  $2.0$  GeV.

## Chapter 4

### Data Analysis

This chapter describes the analysis procedure used to extract and isolate the electron sample from heavy flavor semi-leptonic decays. Section 4.1 describes the quality control, run and event selection used in the analysis. Electron identification cuts and their optimization is presented in Section 4.2. Section 4.3 explains the inclusive electron invariant crosssection calculation. The estimation of the electron component from "photon" related decays of light mesons ("photonic" electron component) through the EXODUS Cocktail is summarized in Section 4.4. The final results for "non-photonic" electron crosssection subtraction are presented in Section 4.5. In order to crosscheck the results of "non-photonic" electron component measurement, the independent "Converter subtraction" analysis was performed which is described in Section 4.6. Section 4.7 presents the Systematic Error estimations for inclusive electron crosssection, Cocktail prediction and the subtracted "non-photonic" electron crosssection.

#### 4.1 Quality Assurance and run selection

The accurate run selection is essential for high precision measurement of Open Charm decay electron component. The contribution of "photonic" electron background is on the order of 80% at low  $p_T$  of total electron signal and even a small variation of total electron yield can cause a significant variation in the background-subtracted result.

The other complication for the electron analysis is that we need to be certain that we have uniform distribution of material in the acceptance. Any additional piece of equipment in the acceptance can cause a significant increase to creation of conversion electrons. Thus we need to apply an elaborate acceptance cuts in order to make a conversion rate uniform in the acceptance.



### 4.1.1 Acceptance cuts

The acceptance for the electrons in PHENIX is best represented in terms of the track inclination angle  $\alpha$  and the azimuthal angle  $\phi$ . The transverse momentum of the particle is inversely proportional to  $\alpha$  and can be approximated to the first order as  $p_T \approx \frac{0.086}{\alpha}$  GeV/c.

The Drift Chamber performance in the East arm was much more stable than that of the West arm and for this analysis we decided to use only the East arm acceptance. Applying very loose electron ID cuts ( $n0 > 1$ ,  $|d_{EMC}| < 5$ ) we can plot the density of the electron candidates in  $\alpha$  vs.  $\phi$  space. Fig 4.1 shows the electron acceptance of the East arm. One can see that big portion of acceptance is "shadowed" by conversions from Time Zero counter (TZR). This detector was installed into the PHENIX acceptance about 60 cm from the interaction point in order to improve the measurement of "start" time for the Time-of-Flight detector. Unfortunately due to very large radiation length of TZR counter ( $X_{TZR} \approx 5.0\%$ !!) it creates a very large rate of conversions far from vertex that creates a huge conversion background in the region of its shadow.<sup>1</sup> The region effected by the TZR counter is removed by the fiducial cut shown in the acceptance plot. Stripes on this figure depict acceptance holes for various PHENIX detectors. There is also a small portion of acceptance (circled on the plot) affected by conversions from cable tray of the "New Trigger Counter" NTC detector, it is also removed by fiducial cut<sup>2</sup>. The small acceptance region at  $\phi > 3.2$  rad that is not affected by TZR "shadow" does not contain high momentum electrons which are of particular interest for Open Charm electron measurements. That is why analysis is using only EMC PbSc sectors E2, E3.

Non-uniform conversion rate acceptance cuts are listed below:

- $|\phi + 0.85 \cdot \alpha| < 2.68$ ; TZR counter cut
- $|\phi + 0.85 \cdot \alpha| > 1.95$ ; NTC cable tray shadow
- E2,E3; EMC sector cut

---

<sup>1</sup>Since the TZR detector debacle, any new detector placed in the PHENIX aperture has been required to submit a "detector impact statement" prior to its inclusion in our apparatus.

<sup>2</sup>The NTC also failed to pass its "detector impact study" and is removed. Neither the NTC nor the TZR were ever used to produce a physics result in PHENIX.

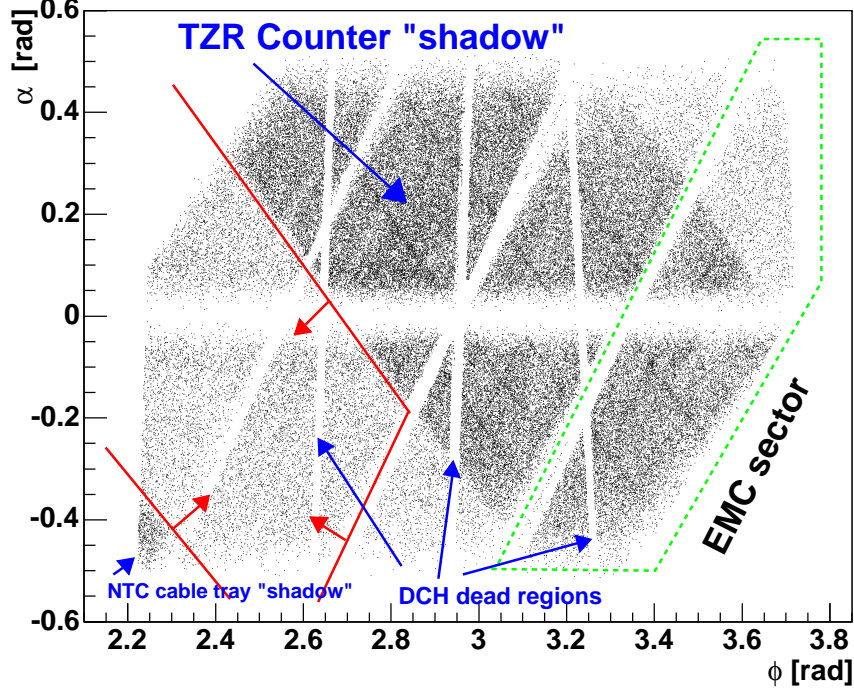


Figure 4.1: Density of the electrons in  $\alpha$  vs.  $\phi$  space for East Arm. The area indicated by red arrows is the acceptance region used in the analysis. The various acceptance holes and additional photon conversion "shadows" indicated on the plot.

The additional holes in the acceptance of the detector were studied starting from those closest to the interaction point (*i.e.* the DCH). Due to the bending of the track in the magnetic field, the azimuthal angle  $\phi'$  at which track intercepts each detector component of the PHENIX will be shifted with respect to DCH  $\phi$ , which is calculated at the "reference radius"  $R_{ref} = 220$  cm. The shift is proportional to  $\alpha$  and is negative for interception with radius  $R > R_{ref}$  and is positive otherwise.  $\phi_{X1} = \phi + 0.06 \cdot \alpha$  corresponds to track angle in X1 DCH plane,  $\phi_{X2} = \phi - 0.04 \cdot \alpha$  corresponds to track intersection of X2 DCH plane. By plotting track density in  $\phi_{X1}$ ,  $\phi_{X2}$  coordinates we can clearly identify the dead DCH regions.

The same analysis can be performed for the Pad Chamber (PC1) dead regions.  $\phi_{PC}$  can be approximated as  $\phi_{PC} = \phi - 0.13 \cdot \alpha$ . Fig. 4.2 shows the

track density in  $\phi_{PC}$ ,  $Z$  space. There is a PC1 region of unstable performance that was cut-out.

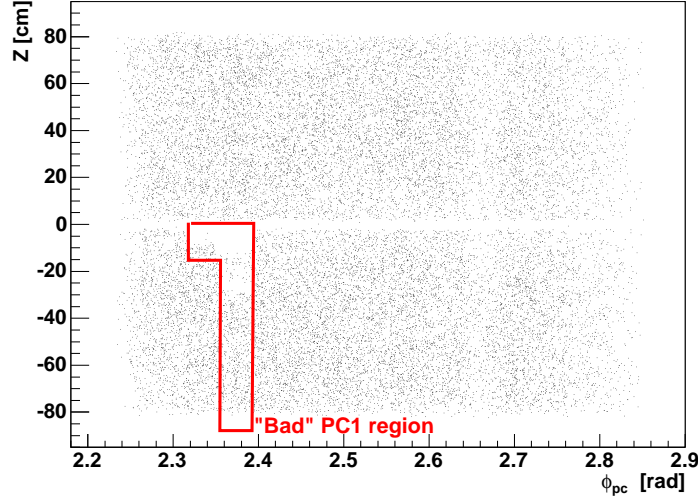


Figure 4.2: Density of the electrons in  $Z$  vs.  $\phi_{PC}$  space.

Final list of tracking fiducial cuts is summarized below:

- $Not(|\phi + 0.06 \cdot \alpha - 2.562| < 0.005 \ \& \ (Z < 0))$  DCH dead region
- $Not(|\phi - 0.13 \cdot \alpha - 2.365| < 0.025 \ \& \ (Z < 0))$  PC1 dead region
- $Not(|\phi - 0.13 \cdot \alpha - 2.325| < 0.025 \ \& \ (Z < 0) \ \& \ (Z > -15))$  PC1 dead region

EMC dead area was calculated by photon density measurements in each EMC tower on a run-by-run basis [46, 47]. The final dead/noise map used in the analysis included all the towers that had a dead/noise flag set at least in one run. 3x3 tower region around the "bad" tower was fiducially removed in order to have more precise energy measurement in the vicinity of the "bad" tower. Fig. 4.3 shows the map of the dead towers in EMC that were removed from the analysis.

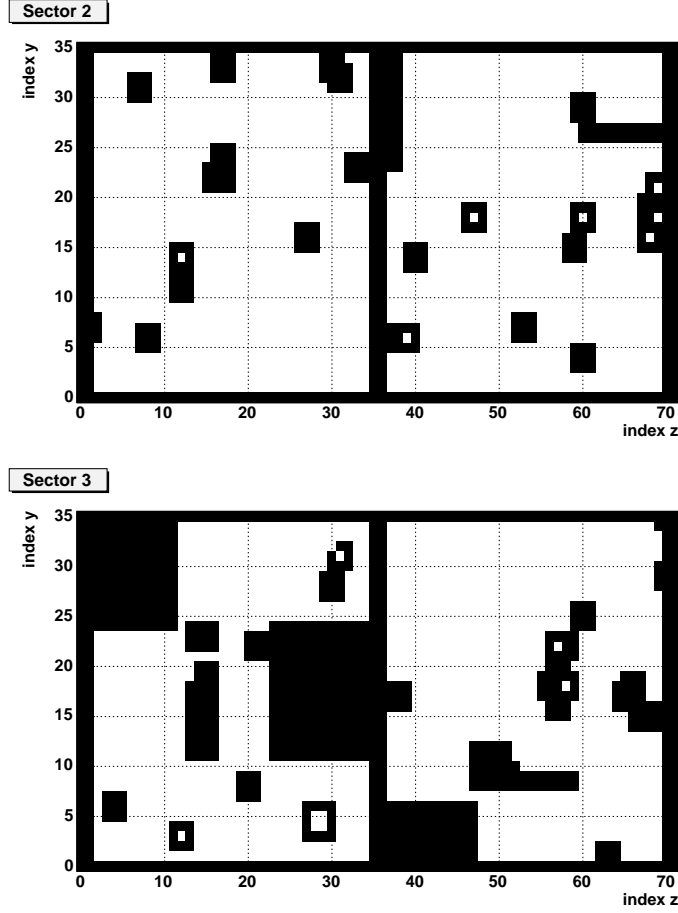


Figure 4.3: Dead/noisy EMC tower map for E2, E3 EMC sectors.

### 4.1.2 Event selection

The “Minimum Bias” event trigger in Run02 P+P was based on the coincidence of at least one hit each in the North and South Beam-Beam Counters (BBC). In order to keep up with high luminosity and to keep the constant bandwidth for Data Acquisition System, a trigger *prescale* logic was implemented. The live trigger rate was artificially reduced by only storing each one event out of  $R_{scale}$ .  $R_{scale}$  is called trigger prescale factor which depended on RHIC store luminosity and could be set to four possible values of 10, 20, 40, 80. The Minimum Bias trigger was always prescaled.

In order to increase the rate of events containing energetic electron, PHENIX uses special Level-1 electronics trigger called the ERT (EMC-RICH trigger). The basic principle of the trigger lies in the online summing of the energy signals in the EMC over a 2x2 tower region called a tile. If the signal from particular tile exceeds the tunable threshold value the specific bit is set in the data stream. To avoid edge effects, the tiles are overlapped and with 2x2 summing the number of tiles equals the number of towers. The other bit is set once a RICH tile (4x5 tubes, overlapping) have a signal exceeding threshold. A spatial match between emc and rich tiles is an indication that the high momentum electron may have been detected in the particular region of detector.<sup>3</sup> The trigger electronics issues the Local Level 1 (LL1) trigger decision for the PHENIX Global Level 1 system (GL1). The energy threshold of the ERT trigger can be adjusted by the threshold settings and was set to have a 50% registration probability for 800 MeV electron. The efficiency of the ERT trigger is discussed in more details in Section 4.3. The same electronics can be used to fire on high energy photons by skipping the coincidence of the RICH bit. This trigger called "Gamma1" was successfully used for high momentum  $\pi^0$  measurements [47, 48]. The ERT trigger has a significant rejection power (the rate of the triggered events compared to Minimum Bias rate)  $R_{ERT} \approx 40 - 50$ , does not limit the DAQ bandwidth, and requires no prescale factor. The proper normalization of the ERT trigger data should be done to the total number of *live* Minimum Bias triggers corresponding to the particular Run. It is crucial to **not** use the number of ERT trigger events for normalization as any noisy channel can artificially increase the rate of this trigger and a strong bias would be applied to the results.

The collision vertex is measured by the Beam-Beam Counters (see Section 3.2.1). The vertex resolution in  $p + p$  Run02 was  $\delta_{Z_{vtx}} = 1.2$  cm. Due to the specific geometry of PHENIX, the tracks originating from collisions that are far from the center of the detector ( $Z_{vtx} = 0$  cm) have a higher probability to interact with the material of the Central Magnet thus creating additional conversion electron background. The collision vertex distribution for the particles that are primarily electrons (tight eID cut  $n0 > 3$ ) is shown in Fig. 4.4. One can see that the vertex distribution has an almost Gaussian shape with some additional structure for high  $Z_{vtx}$ . In order to minimize the conversion background, we use tight vertex cuts for this analysis and only look at the events with  $|Z_{vtx}| < 25$  cm.

---

<sup>3</sup>low momentum particles have displaced RICH and EMC tiles and fail the trigger.

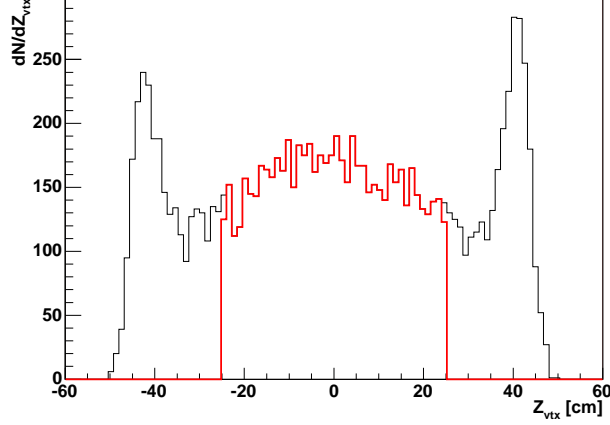


Figure 4.4: BBC  $Z_{vtx}$  distribution for electron candidates ( $n_0 > 3$ ). Bold line shows the vertex region used in the analysis.

#### 4.1.3 Run selection and event counting

To filter the bad runs we looked at the  $\phi$  distribution of all charged tracks ( $p_T > 0.4$  GeV/c) with standard electron identification cuts (except for RICH  $n_0 > 1$  cut, see Section 4.2) and all acceptance cuts. The  $\frac{dN}{d\phi}$  distribution for each run was normalized to the number of recorded Minimum Bias events  $N_{MB}$ . Then the ratio of the  $\frac{1}{N_{MB}} \frac{dN}{d\phi}$  distribution for given run to the same distribution for the chosen "reference" run (run having significant statistics and stable acceptance) was fitted with a constant  $R$ . Any significant deviation of the fit parameter  $R$  from one is an indication of additional dead area in the trial run. The criteria for the selection of the run was chosen to be:

- $R > 0.94$
- $\chi^2_\nu < 2.0$

The run by run variation of  $R$  and  $\chi^2_\nu$  presented on Fig. 4.5 (runs shown as red are considered to be "bad"). During Run02 we had an period with additional "photon converter" installed inside the PHENIX acceptance. "Converter" subtraction method explained in details in Section 4.6. Converter run period should be treated separately from Non-Converter run period. The total event statistics of the Converter and Non-Converter run periods summarized in Table 4.1.

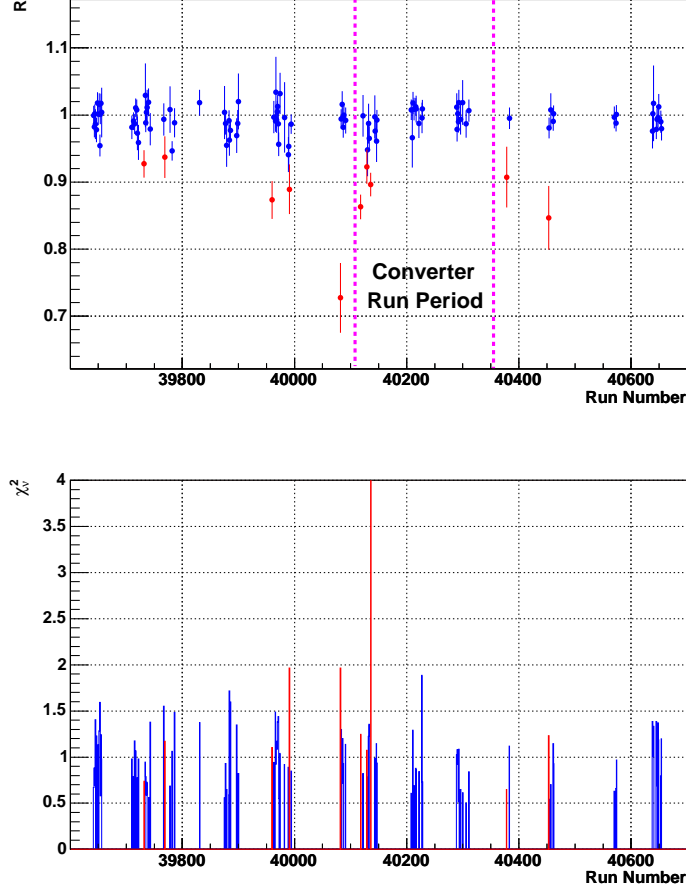


Figure 4.5: Run-by-run variation of charged particle yield.

Table 4.1: Statistics summary for Non-Converter and Converter run period.

|                       | $N_{MB}$          | $N_{MB \text{ live}}$ |
|-----------------------|-------------------|-----------------------|
| Non-Converter "Total" | 15 931 737        | 475 849 920           |
| Non-Converter "Bad"   | 540 061           | 10 683 600            |
| Non-Converter "Good"  | <b>15 391 676</b> | <b>465 166 320</b>    |
| Converter "Total"     | 4 851 787         | 264 284 240           |
| Converter "Bad"       | 361 847           | 28 947 760            |
| Converter "Good"      | <b>4 489 940</b>  | <b>235 336 480</b>    |

## 4.2 Electron identification cuts

Electron identification is one of the most critical parts of the analysis and required a precise tuning of the eID parameters. PHENIX is able to identify the electrons using the following parameters:

- Number of RICH photomultipliers that have hit within the projected track ring -  $n0$ .
- EMC matching - distance between track projection and EMC cluster in  $\phi$  and  $Z$  coordinates. We denote  $d_{EMC}$  as  $d_{EMC} = \sqrt{d\phi_{EMC}^2 + dZ_{EMC}^2}$ .
- Ratio of EMC deposited energy to particle momentum -  $E/p$ .

Those variables have been used for all the current PHENIX electron results [49, 50, 51]. All eID parameters were adjusted both for Data and Monte Carlo simulation to be identical and uniform (i.e. matching parameters have the mean value of zero and width of  $1\sigma$  independent of momentum and uniform throughout the detector acceptance).

### 4.2.1 $n0$ cut optimization

The rejection power of separate eID cuts was tested by studying the  $E/p$  distribution of electron candidates before and after the cut.

An initial assumption is chosen for the  $n0$  cut. This cut can not be set as low as one phototube since the random association background due to electronics noise would be too high. Thus  $n0 > 1$  was assumed to be lowest possible  $n0$  cut. The next step is to study what happens as the cut is tightened. Fig. 4.6 shows the effect of  $n0 > 2$  cut on the initial electron candidate sample ( $n0 > 1$ ) for  $p_T > 0.4$ . The bottom left inset shows the rejection power of the cut which shows the remaining portion of the particles after the cut. One can see a distinctive peak in  $E/p$  distribution which defines "real" electrons. The tail at  $E/p < 0.5$  consists principally of random charged hadron tracks associated with real RICH hits and off-vertex conversion electrons with mis-measured momentum. In order to estimate the effectiveness of the eID cut we check how much signal it removes in the  $E/p$  electron peak region and how strongly it cuts away the low  $E/p$  background.

From the plot we can conclude that we lose  $\approx 10\%$  of the electron signal and  $\approx 50 - 60\%$  of the background. This loss of the electron efficiency is too large to afford and the rejection is not significantly high so we decided to use  $n0 > 1$  cut for the analysis.



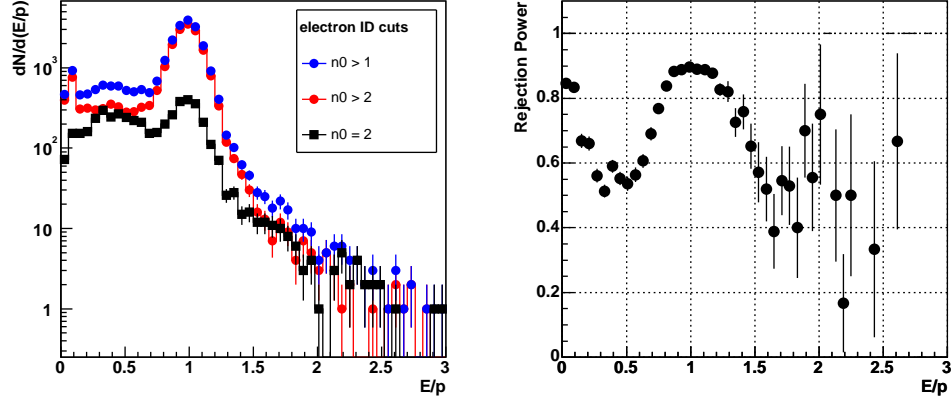


Figure 4.6: a)  $E/p$  distribution for the electron candidates for different  $n_0$  cuts  
b) Rejection power of eID cut  $n_0 > 2$  in comparison with  $n_0 > 1$  cut.

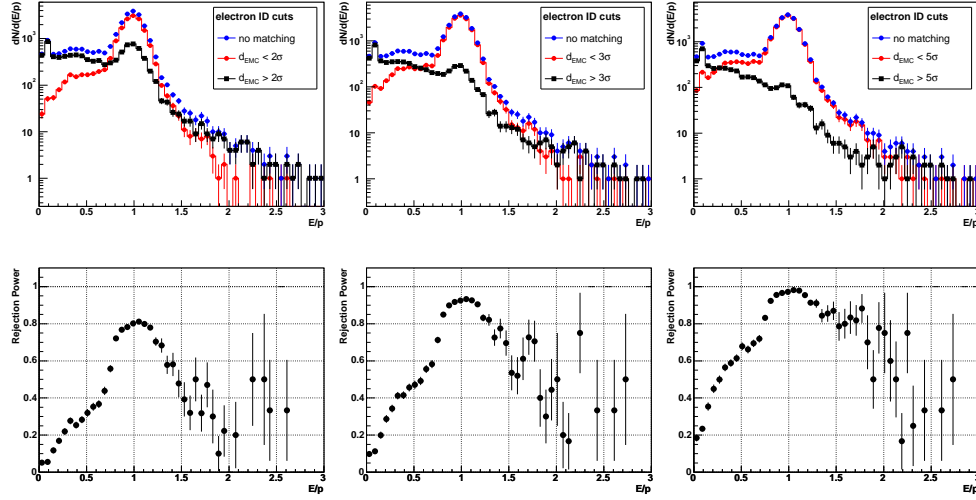


Figure 4.7:  $E/p$  distribution for the electron candidates and rejection power for different  $d_{EMC}$  cuts a)  $d_{EMC} < 2\sigma$  b)  $d_{EMC} < 3\sigma$  c)  $d_{EMC} < 5\sigma$ .

## 4.2.2 EMC matching cut optimization

The similar studies have been done on the "adjusted" track matching  $d_{EMC} = \sqrt{d\phi_{EMC}^2 + dZ_{EMC}^2}$  parameter.  $d_{EMC}$  variable cut has been tested for values of  $d_{EMC} < 2$ ,  $d_{EMC} < 3$ , and  $d_{EMC} < 5$ . The resulting rejection power of is shown in Fig. 4.7.

It is clear that  $d_{EMC} < 3$  already cuts a big portion of low  $E/p$  electron candidates leaving the peak statistics almost intact. The efficiency of a  $d_{EMC} < 2$  cut at the peak is  $\approx 80\%$  which is a significant statistics loss. Therefore,  $d_{EMC} < 3$  was chosen as an optimum for the analysis.

### 4.2.3 $E/p$ cut parametrization

We expect electrons to generate an electromagnetic shower in the EMC and therefore register an energy equal to their momentum. The energy over momentum distribution not only enables us to identify electrons by also allows us to measure both the energy and momentum resolution. The resolution of  $E/p$  can be directly derived from  $\frac{\sigma(p)}{p}$  and  $\frac{\sigma(E)}{E}$  and can be written as:

$$\begin{aligned}\frac{\sigma(p)}{p} &= \sqrt{\sigma_{MS}^2 + (\sigma_{DCH} \cdot p)^2} \\ \frac{\sigma(E)}{E} &= \sqrt{\sigma_C^2 + \left(\frac{\sigma_{EMC}}{\sqrt{E}}\right)^2}\end{aligned}\quad (4.1)$$

where  $\sigma_{MS}$  is term due to the multiple scattering,  $(\sigma_{DCH} \cdot p)$  is DCH angular resolution,  $\sigma_C$  is a constant term of EMC energy resolution,  $\frac{\sigma_{EMC}}{\sqrt{E}}$  - is an EMC energy resolution depending upon fluctuations in the number of particles produced in the EM shower.

The fluctuations are independent and so

$$\sigma\left(\frac{E}{p}\right) \approx \sqrt{\frac{\sigma(E)^2}{p^2} + \frac{E^2 \cdot \sigma(p)^2}{p^4}} \approx \sqrt{\sigma_C^2 + \sigma_{MS}^2 + \frac{\sigma_{EMC}^2}{p_T} + (\sigma_{DCH} \cdot p)^2} \quad (4.2)$$

Eq. 4.2 was obtained assuming  $E \approx p \approx p_T$ . From this equation one can see that at low  $p_T$  the main contributor to  $E/p$  resolution is energy resolution which is been overcome by momentum resolution term at high  $p_T$  and starts grow linearly.

The mean and sigma of  $E/p$  distribution for electron candidates was obtained as a function of  $p_T$  by fitting each slice with Gaussian + exponential background (or Gaussian wherever background is negligible or non-exponential). Fig. 4.8 shows the fit results for different  $p_T$  bins starting from 0.4 GeV/c up to 5 GeV/c.

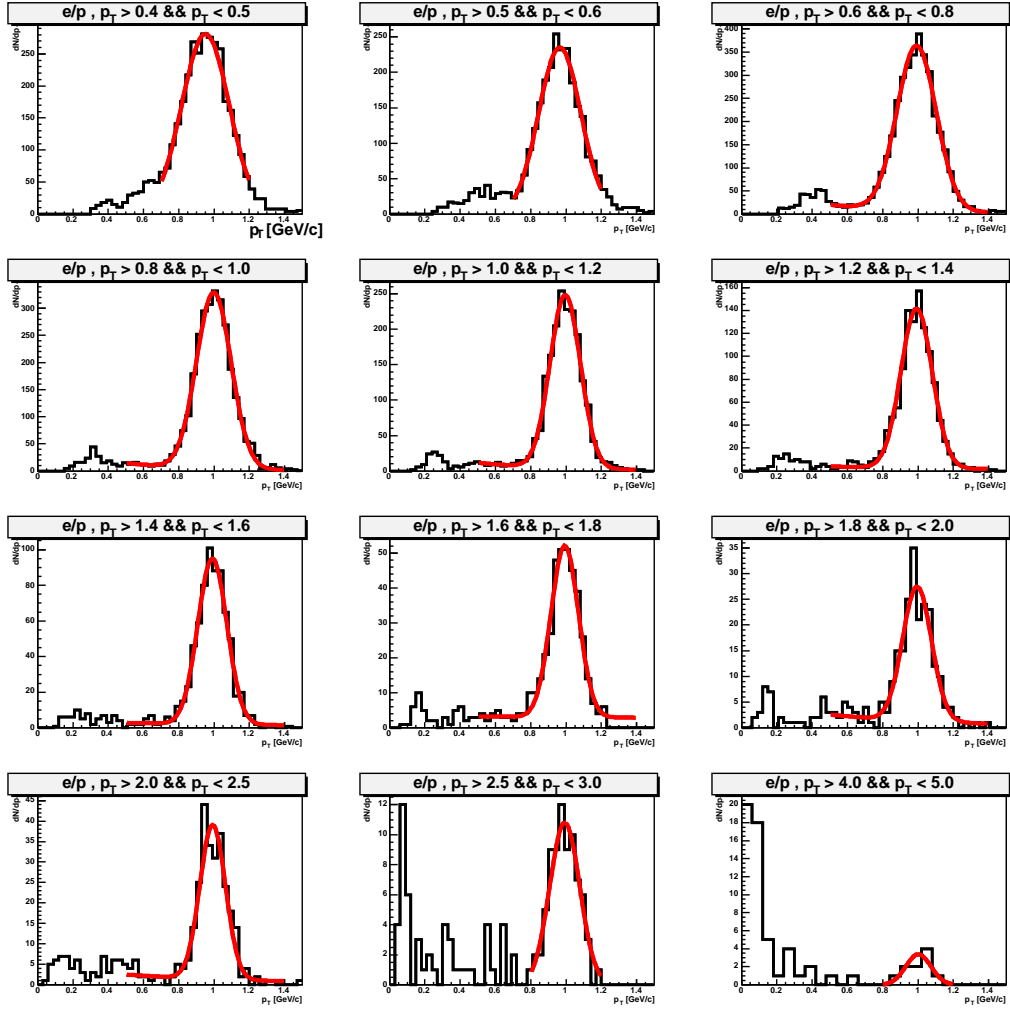


Figure 4.8: Fits to  $E/p$  distribution of electron candidates for different  $p_T$  bins.

Fig. 4.9 shows the mean and sigma distribution for the Gaussian component of the fit as a function of electron transverse momentum. One can see that we have a very clean electron sample with the background contribution slowly drifting to the lower  $E/p$  values going to higher momentum.

From Fig. 4.8 one can see that our energy and momentum measurements are in good agreement. The apparent fall of the mean  $E/p$  is possibly related with the fact that at low momentum the inclination angle of the track becomes significant and EMC cluster starts to spread spatially and we start measure

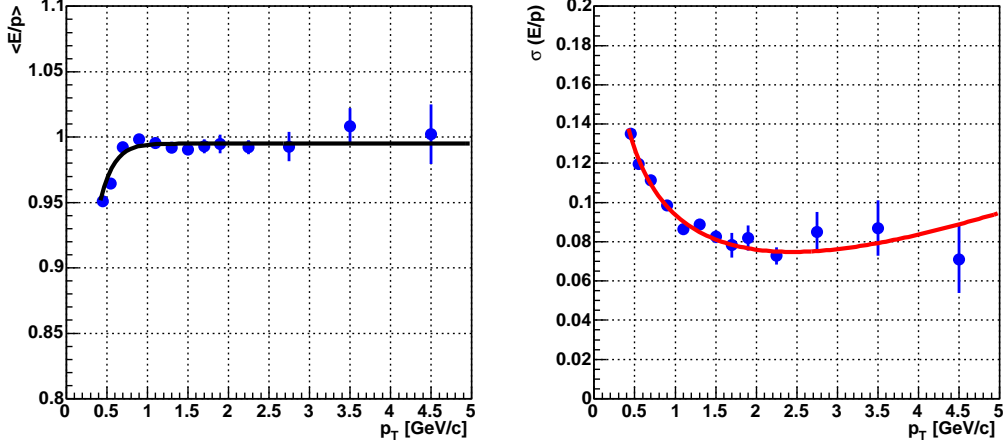


Figure 4.9: a) Mean and b) Sigma of  $E/p$  Gaussian fit to electron signal as a function of  $p_T$  (Sigma is fitted with Eq. 4.2 function).

only a fraction of its total deposited energy<sup>4</sup>.

The  $E/p$  resolution is fitted with Eq. 4.2 and the following energy and momentum resolution were derived:

- $\sigma_C \oplus \sigma_{MS} = (3.82 \pm 0.86)\%$
- $\sigma_{EMC} = (8.47 \pm 0.28)\%$
- $\sigma_{DCH} = (1.48 \pm 0.41)\%$

This results are in good agreement with PHENIX measurements of energy and momentum resolution [47, 70] via other independent techniques.

As the background level in p+p collisions is very low and significantly suppressed by EMC matching cuts, we decided to use a loose ( $\pm 3\sigma$ )  $E/p$  cut for the analysis

$$\left| \frac{E/p - \langle E/p \rangle}{\sigma(E/p)} \right| < 3$$

Thus, the cut width follows the fitted sigma as a function of the track's momentum.

---

<sup>4</sup>The EMC cluster algorithm is tuned for photons that land at near-normal incidence.

### 4.3 Inclusive electron invariant crossection

This section of the Thesis explains the procedure of single differential crossection calculation for single electrons starting from the "raw"  $\frac{N_e}{\Delta p_T}$  distribution, correction of the "raw" electron distribution to full azimuthal & one unit in rapidity, estimation of background level, combining ERT and MB data sample, trigger bias correction of the final crossection and bin width related corrections. The final expression for MB and ERT inclusive crossection can be written the following way

$$\begin{aligned}
 E \frac{d\sigma}{dp_{TMB}^3} &= \frac{1}{N_{MB}} \cdot \frac{1}{2\pi} \cdot \frac{1}{2} \cdot \frac{1}{p_T} \cdot \frac{N_{eMB}}{\Delta p_T} \cdot \frac{1}{\Delta y} \cdot \frac{\sigma_{pp\ tot} \cdot \epsilon_{BBC}}{\epsilon_{reco}(p_T) \cdot \epsilon_{bias}(p_T)} \\
 E \frac{d\sigma}{dp_{TERT}^3} &= \frac{1}{N_{MB\ live}} \cdot \frac{1}{2\pi} \cdot \frac{1}{2} \cdot \frac{1}{p_T} \cdot \frac{N_{eERT}}{\Delta p_T} \cdot \frac{1}{\Delta y} \cdot \frac{\sigma_{pp\ tot} \cdot \epsilon_{BBC}}{\epsilon_{reco}(p_T) \cdot \epsilon_{bias}(p_T) \cdot \epsilon_{ERT}(p_T)}
 \end{aligned} \tag{4.3}$$

where

- $N_{MB}$  - number of scaled minimum bias events in MB sample (Table 4.1)
- $N_{MB\ live}$  - number of live minimum bias events in ERT sample (Table 4.1)
- $\frac{N_e}{\Delta p_T}$  - "raw" electron count in  $p_T$  bin
- $\Delta y$  - rapidity range ( $\pm 0.5$  units in rapidity)
- $\epsilon_{reco}(p_T)$  - reconstruction and acceptance efficiency (correction function)
- $\epsilon_{bias}(p_T)$  - BBC trigger bias
- $\sigma_{pp\ tot}$  - total p+p inelastic crossection [52] ( $42.2 \pm 1.9$ ) mb
- $\epsilon_{BBC}$  - BBC efficiency for Minimum Bias [52] ( $0.516 \pm 0.031$ )
- $\epsilon_{ERT}(p_T)$  - ERT trigger efficiency

#### 4.3.1 "Raw" electron yield

A standard procedure for any spectroscopic measurement is to start with "raw" signal counting. First of all we selected an appropriate  $p_T$  binning which was chosen to match the bin boundaries of previous Au+Au single electron measurements [51]. Those bins that had significant statistics compared to Au+Au were split into two. The final choice for the binning is listed below:

- {0.4, 0.5, 0.6, 0.8, 1.0, 1.2, 1.4, 1.6, 2.0, 2.5, 3.0, 4.0, 5.0}

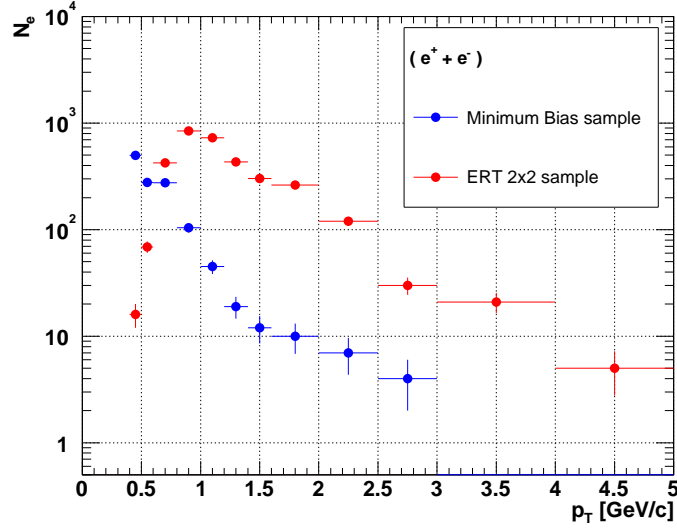


Figure 4.10: "Raw" electron count in  $p_T$  bin for Minimum Bias and ERT trigger sample.

Table 4.2: "Raw" electron count in  $p_T$  bin for Minimum Bias and ERT trigger sample.

| $p_T$ bin [GeV/c] | $N_e$ $_{MB}$ | $\delta N_e$ $_{MB}$ | $N_e$ $_{ERT}$ | $\delta N_e$ $_{ERT}$ |
|-------------------|---------------|----------------------|----------------|-----------------------|
| 0.4-0.5           | 498           | 22.31                | 16             | 4.00                  |
| 0.5-0.6           | 278           | 16.67                | 69             | 8.30                  |
| 0.6-0.8           | 276           | 16.61                | 424            | 20.59                 |
| 0.8-1.0           | 104           | 10.20                | 846            | 29.09                 |
| 1.0-1.2           | 45            | 6.71                 | 728            | 26.98                 |
| 1.2-1.4           | 19            | 4.36                 | 433            | 20.81                 |
| 1.4-1.6           | 12            | 3.46                 | 301            | 17.35                 |
| 1.6-2.0           | 10            | 3.16                 | 263            | 16.22                 |
| 2.0-2.5           | 7             | 2.65                 | 120            | 10.95                 |
| 2.5-3.0           | 4             | 2.00                 | 30             | 5.48                  |
| 3.0-4.0           | 0             | 0                    | 21             | 4.58                  |
| 4.0-5.0           | 0             | 0                    | 5              | 2.24                  |

Fig. 4.10 shows the electron statistics per bin for the ERT and Minimum Bias trigger data samples. Table 4.2 summarizes "raw" electron counting results. One can see that statistics in three highest  $p_T$  bins is quite low which is a limiting factor for Run02 single electron analysis.

### 4.3.2 ERT trigger efficiency

The ERT trigger for Run02 was calculated for the  $J/\psi$  analysis in  $p + p$  Run02 [49, 53] using single photons. The photon analysis uses only the EMC bit of the ERT trigger. However, the RICH trigger part the trigger does not introduce a significant efficiency loss. We can not use single electrons for the trigger efficiency measurement due to low statistics. The ERT efficiency calculation is trivial and described below.

- Find a single photon cluster of energy  $E$  in EMC with tight identification cuts from a Minimum Bias event.
- Check whether the ERT EMC trigger bit was set for this event and whether **this particular photon** fired the trigger.
- The ratio of ERT registered yield  $dN_r/dE$  to the total yield  $dN_t/dE$  will give us ERT trigger efficiency  $\epsilon_{ERT}(E)$

Taking into account the fact that the electron momentum resolution at low  $p_T$  is much better then energy resolution we use the trigger efficiency as a function of particle momentum instead of energy  $\epsilon_{ERT}(p)$ .

The measured ERT trigger efficiency for the E2, E3 EMC sectors is shown in Fig. 4.11. The systematic error shows the maximum extent error of efficiency variation obtained by a 10% variation of the number of dead/noisy towers in the trigger simulation. The trigger efficiency may be underestimated for this analysis because we remove additional "bad" EMC towers (see Fig. 4.3) as compared to the  $J\Psi$  analysis, but this difference is easily covered by the systematic error. Both the trigger efficiency and hi-lo limits of the systematic error were fitted with arbitrary functions, presented in Table 4.3

Table 4.3: Fit results for ERT trigger efficiency and hi-lo systematic error band for E2,E3 EMC sectors.

|    | ERT efficiency                       | Systematic error (hi limit)          | Systematic error (lo limit)          |
|----|--------------------------------------|--------------------------------------|--------------------------------------|
| E2 | $\frac{1}{1+0.771/p^4+0.473/p^9}$    | $\frac{1}{1+0.451/p^4+0.525/p^6}$    | $\frac{1}{1+1.307/p^4+0.685/p^9}$    |
| E3 | $\frac{0.96}{1+1.252/p^4+0.588/p^9}$ | $\frac{0.99}{1+0.681/p^4+0.787/p^6}$ | $\frac{0.94}{1+1.649/p^4+1.435/p^9}$ |

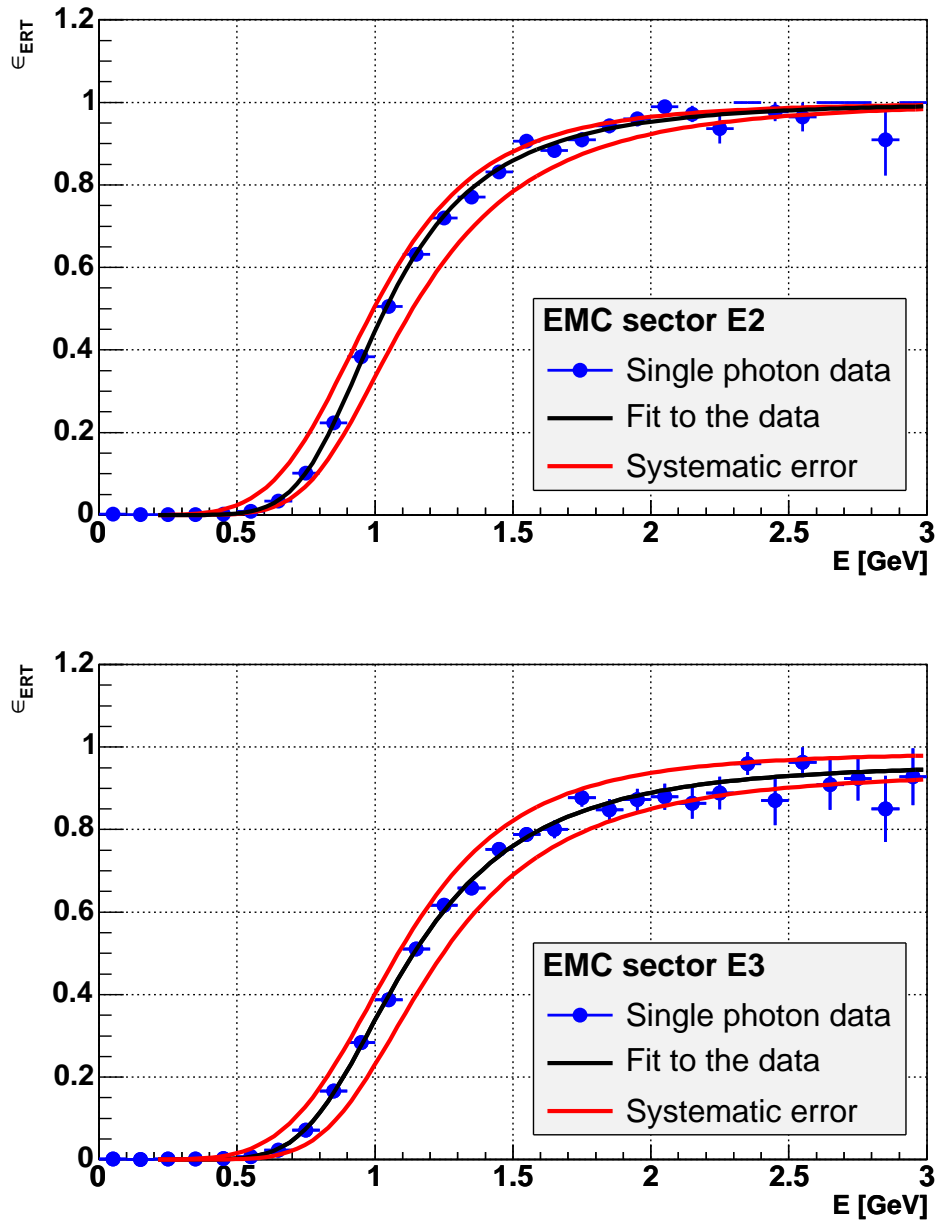


Figure 4.11: ERT trigger efficiency for E2, E3 EMC sector. The systematic error band to the efficiency from trigger simulation.



### 4.3.3 Hadronic background

The major source of background for this analysis is a random coincidence of a charged track with a RICH cluster (thereby falsely identifying the track as an electron). This was studied previously in great detail for the  $Au + Au$  single electron measurements [50, 51] where this contribution is much more significant. In  $p + p$  collisions the multiplicity is low, thus the chance of random coincidence is significantly reduced (see Fig. 4.8 for background level estimation). The standard technique that is used in PHENIX offline software is so called "*flip and slide*" method which is based on creation of a fake ("swapped") charged tracks by exchanging the North and South hits in all detectors except the drift chamber. This way we create an unbiased random track that then is being associated with outer PHENIX detector. The number of RICH phototube that are associated with the "swapped" charged track denotes as  $sn0$ . The distribution of  $E/p$  for the  $n0 > 1$  and  $sn0 > 1$  is shown in Fig. 4.12 for Minimum Bias data sample. Unfortunately, we can not use ERT trigger sample for those studies because the electron content of ERT events is strongly biased by trigger efficiency. One can see that the statistics of the purely random association of Minimum Bias sample is very small and alternative way to estimate the background contribution must to be found.

We want to make an assumption at this point that the random association rate should not depend on the inclination angle of the track and, thus, it is not a function of the particles momentum. We would then find a constant probability  $\epsilon_{rand}$  that the charged track is associated with a RICH ring. We can plot the  $E/p$  distribution for **charged tracks** and normalize it to the  $sn0 > 1$   $E/p$  distribution at low  $p_T$ . The normalization constant will be  $\epsilon_{rand}$  by construction. Fig. 4.13 shows the  $E/p$  distribution for  $n0 > 1$ ,  $sn0 > 1$ , and charged hadrons scaled by  $\epsilon_{rand} = (3 \pm 1.5(sys)) \cdot 10^{-4}$ . In order to account for a qualitative comparison in the normalization, we put a large (50%) systematic error on this value.

This probability does not include the effect of the  $\pm 3\sigma$   $E/p$  cut rejection. It adds an additional suppression of the random hadron association component by a factor  $\approx 10 - 100$ . Fig. 4.14 shows the probability that randomly associated charged track "survives" the  $E/p$  cut.

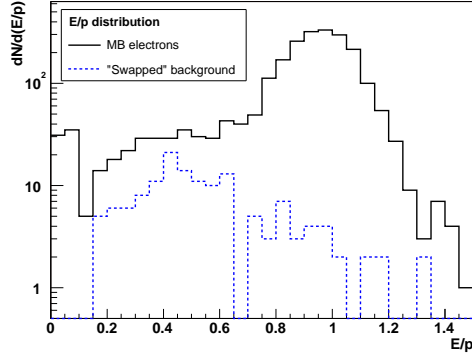


Figure 4.12:  $E/p$  distribution for electron candidates (solid curve) and random association tracks  $sn0 > 1$  (dashed curve) for Minimum Bias events  $p_T > 0.4$  GeV/c.

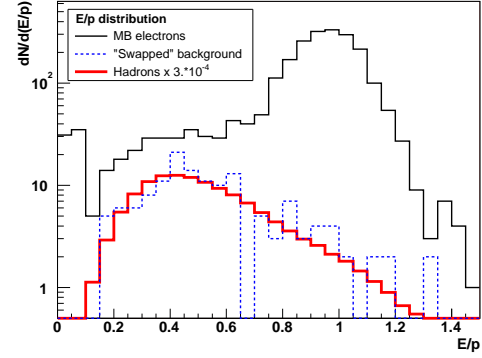


Figure 4.13:  $E/p$  distribution for electron candidates (solid curve), random association tracks (dashed curve) and charged hadron tracks scaled by  $\epsilon_{rand} = 3 \cdot 10^{-4}$  (thick solid curve) for Minimum Bias events  $p_T > 0.4$  GeV/c.

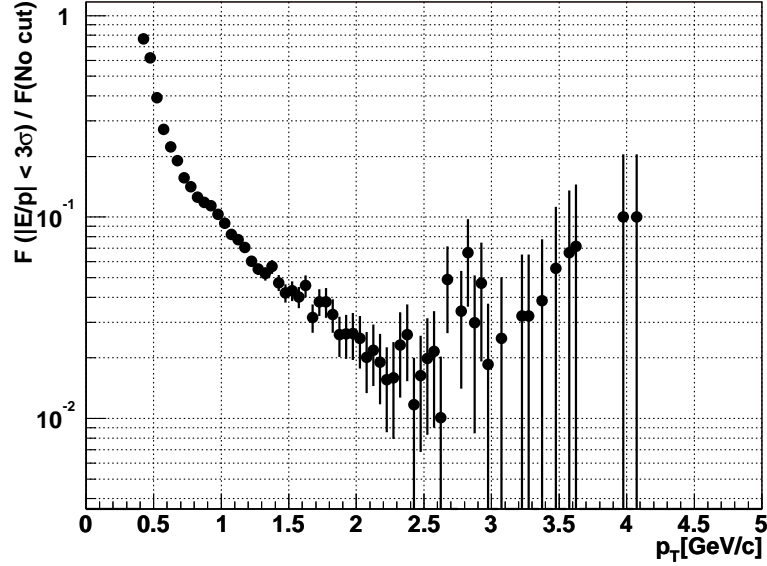


Figure 4.14: Rejection power of  $|E/p| < 3\sigma$  for charged hadrons.

#### 4.3.4 $\delta$ -electron background

$\delta$ -electrons (also called "knock-on" electrons or  $\delta$ -rays) refer to energetic electrons, that were knocked from the atomic shell of some atom in the detector volume. Depending on the construction of the detector and particle identification principles "knock-on" electrons may create a significant background.

In the case of PHENIX we need to take into account the rate of electrons emitted in RICH gas volume. The difference with previous effect is that delta electron, emitted with a reasonably small angle with respect to the initial hadron can create a hit in RICH and be misidentified as an electron. Thus, we need to estimate the probability for a hadron to emit delta electron that may fire RICH detector. To estimate the yield of  $\delta$ -rays in RICH volume (100 cm of  $CO_2$ ) we used the formula ( 4.4, 4.5) [9]<sup>5</sup>.

$$\frac{d^2N}{dTdx} = \frac{1}{2} K z^2 \frac{Z}{A} \frac{1}{\beta^2} \frac{(1 - \beta^2 T/T_{max})}{T^2} \quad (4.4)$$

$$T_{max} = \frac{2m_e c^2 \beta^2}{1 + 2\gamma m_e/M + (m_e/M)^2} \quad (4.5)$$

where

- $K$  -  $4\pi N_A r_e^2 m_e c^2 = 0.307075 [MeV cm^2]$
- $Z$  - atomic number of absorber
- $A$  - atomic mass of absorber [ $g mol^{-1}$ ]
- $z$  - charge of the incident particle
- $T$  - kinetic energy of the electron
- $\gamma$  -  $\gamma$  the incident particle
- $\beta$  -  $\beta$  the incident particle
- $M$  - mass of the incident particle
- $T_{max}$  - maximal possible kinetic energy of the  $\delta$ -electron (Eq. 4.5)

RICH threshold for the electron is  $\gamma_{thr} = 35$ . Thus, minimal energy of electron that can "fire" RICH is  $E_{min} = \gamma_{thr} \cdot m_e c^2 \approx 17.9$  MeV. Integrating Eq. 4.4 on  $T$  from  $E_{min}$  to  $T_{max}$  we obtain the total yield of  $\delta$ -electrons as the function of pion momentum (Fig. 4.15).

The angle of the "knock-on" electron with respect to the incident pion can be calculated by the following formula [9]:

---

<sup>5</sup>In calculations below we assume the validity of Rutherford crossection and spin-0 incident pion

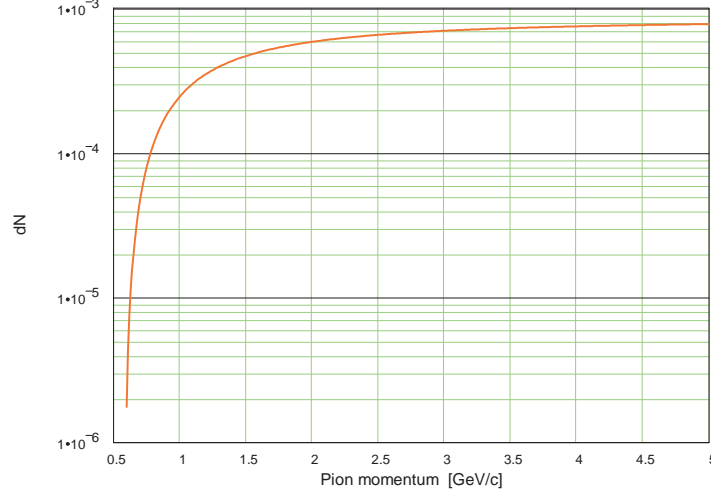


Figure 4.15: Total  $\delta$ -electron rate as a function of incident pion momentum.

$$\cos(\theta) = (T_e/p_e)(p_{max}/T_{max}) \quad (4.6)$$

where

$T_e, p_e$  - kinetic energy and momentum of the electron

$T_{max}, p_{max}$  - maximum available kinetic energy and momentum of the electron

Due to the RICH's geometrical acceptance, only when the  $\delta$ -ray is produced within  $\cos(\theta_{max}) > 1/n$  with respect to the pion direction will its Cerenkov radiation overlap in the RICH "ring" constructed around the pion projection point. The refraction index for  $CO_2$  gas  $n = 1 + 410 \cdot 10^{-6}$  which gives the value for the maximum angle  $\theta_{max} = 28.63$  mrad. From Eq. 4.6 one can calculate the minimal kinetic energy  $T_{min}$  of  $\delta$ -electron which is deflected to an angle  $\theta = \theta_{max}$ . Fig. 4.16 shows the range of kinetic energies for electrons that are emitted in  $\theta < \theta_{max}$  cone around the direction of incident pion.

Now we can obtain the yield of  $\delta$ -electrons that can be reconstructed in the RICH by integrating Eq. 4.4 from  $T_{min}$  to  $T_{max}$ .  $\delta$ -electrons rate as a function of incident pion momentum is shown in Fig. 4.17. One can see that we have a probability of  $\epsilon_\delta \approx 10^{-6}$  for a pion to create such an electron (the rate is even smaller for incident particle of higher mass). The yield is significantly lower then previously calculated random association background of  $3 \cdot 10^{-4}$ . Thus,  $\delta$ -electron contribution can be neglected in PHENIX electron analysis.

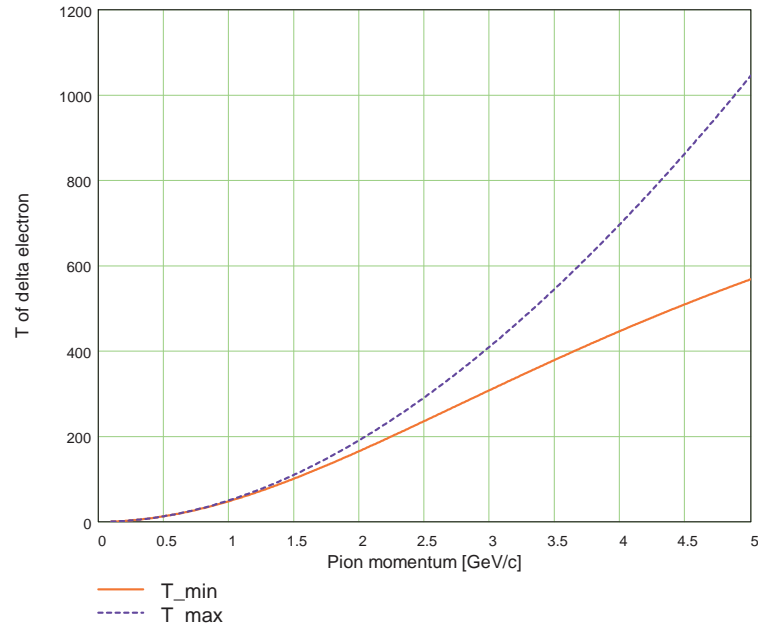


Figure 4.16: The range of  $\delta$ -electron kinetic energy that can be reconstructed by RICH,  $T_{min}$  (solid) and  $T_{max}$  (dashed).

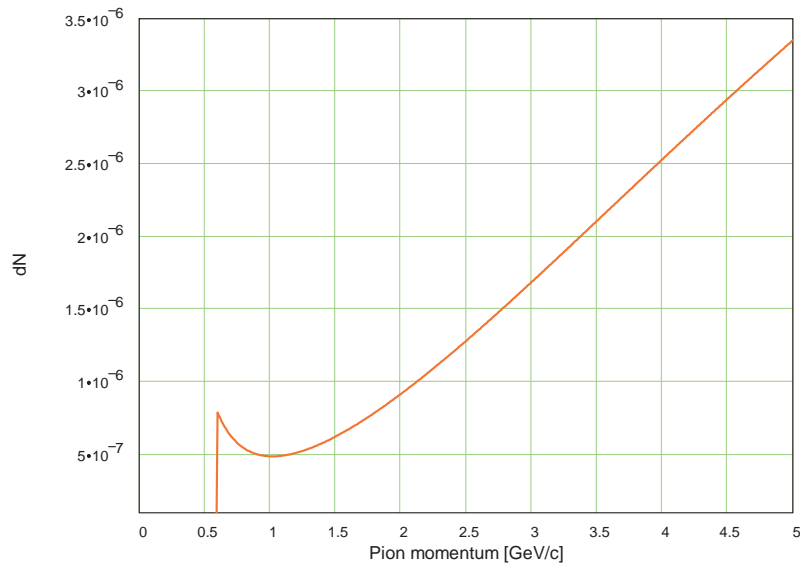


Figure 4.17: Rate of  $\delta$ -electrons reconstructible by RICH as a function of incident pion momentum.

### 4.3.5 Acceptance Correction function

In order to properly normalize the results of the measurements, we need to calculate the factor which describes the difference between an ideal  $4\pi$  detector and PHENIX. This factor (see Eq. 4.3) is called the correction function  $\epsilon_{reco}(p_T)$  and takes into account the limited acceptance and track reconstruction efficiency.

The standard way to obtain the correction function is through the full simulation of particle detection probability assuming an ideally distributed input particle density. In the case of single electron analysis we "throw" single electrons, generated by the EXODUS [54] event generator, with the following input parameters

- Uniform azimuthal angle distribution  $0 < \phi < 2\pi$
- Uniform vertex  $Z_{vtx}$  distribution<sup>6</sup>  $|Z_{vtx}| < 25$  cm
- Uniform rapidity distribution  $-0.6 < y < 0.6$  units
- Uniform  $p_T$  distribution  $0.0 < p_T < 5.0$  GeV/c

The total statistics of our simulation sample was  $3.98 \cdot 10^6$  single particles ( $2.00 \cdot 10^6$  positrons and  $1.98 \cdot 10^6$  electrons).

The particles pass through the full detector simulation chain called PISA (*PHENIX Integrated Simulation Application* [55]). PISA is a GEANT-3 based simulation code that has been successfully used since 1992 to simulate realistic particle propagation and detector response. The particle is "swimmed" through the tabulated Magnetic Field and GEANT-3 simulates the interaction of the primary particle with the material inside the PHENIX aperture. Both primary and secondary particles create a **hit** every time they enter the active area of the detector. This "Monte Carlo hit" information is stored in the "*PISA output file*".

The next step in simulation is applying a realistic detector response to the MC hits. This procedure includes a smearing of hit position and timing with appropriate resolution, digitization of the timing and analog information, hit merging, applying time-of-flight effects, and reproduction of registration efficiency & dead map for each detector subsystem, e.t.c.

---

<sup>6</sup>There is no strong dependence of reconstruction efficiency on  $Z_{vtx}$ . This fact allows us to use a "flat" vertex distribution instead of realistic "Gaussian" distribution (shown in Fig. 4.4)

The final step of the simulation is the *reconstruction* of the simulated data using standard PHENIX offline code which is used for real data analysis.

As an output we have a collection of reconstructed tracks. The offline software (*evaluation package*) maintains the relationship between MC track and reconstructed track. A "main contributor" scheme is used in that the MC track that provided most hits to any reconstructed track is then considered to be the "**main contributor**" to that track and is considered as the source of that reconstructed track. This helps us to obtain a direct correspondence between the reconstructed track parameters and the input track parameters.

The first thing that needs to be checked in simulation is the momentum and energy resolution. Fig. 4.18 shows the mean and  $\sigma$  of the difference between reconstructed  $p_T$  and initial  $p_{T\ MC}$  transversal momentum as a function of  $p_{T\ MC}$  for electrons and positrons. One can see that there is a linear dependence of the  $\delta(p_T)$  which needs to be removed from the simulation (we can not justify that this effect should exist in simulation and need to remove it and later treat it as a systematic error).

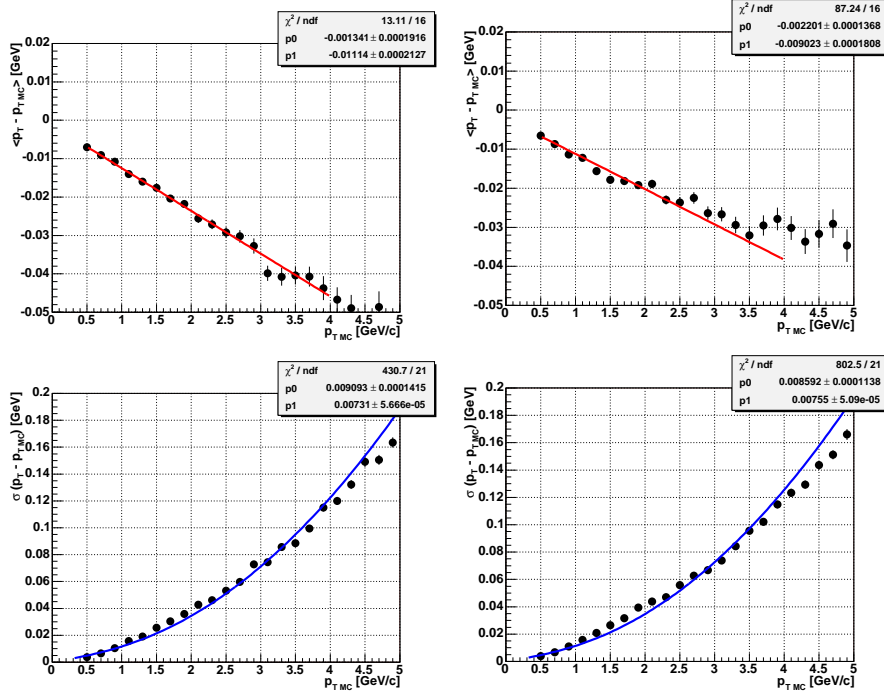


Figure 4.18: Mean and sigma of difference between reconstructed and ideal  $p_T$  in Simulation for electrons (left) and positrons (right). Linear fit is shown for mean distribution, sigma is fitted with Eq. 4.1 functional form.

The momentum resolution can be estimated from the fit to  $\sigma(p_T - p_{T\ MC})$  using functional form for the momentum resolution (Eq. 4.1). The Drift Chamber momentum resolution term in simulation is factor of two smaller then in the data:

- $\sigma_{MS} = (0.87 \pm 0.05)\%$
- $\sigma_{DCH} = (0.74 \pm 0.02)\%$

this means that we need to artificially worsen the momentum resolution in simulation and study what effect it may cause on the correction function (see Section 4.7).

The momentum distribution of input particles is uniform and different from the  $\frac{dN_e}{dp_T}$  of real data. In order to take into account this difference, a weighting factor of  $(\frac{dN_e}{dp_T})_{Data}$  dependent upon  $p_{T\ MC}$  is applied to each Monte Carlo variable. This weighting procedure "artificially" adjusts the shape of the input MC momentum distribution to match the final Data momentum shape. The shape of the final inclusive electron distribution can be taken from Fig. 4.33 and we can assume the weighting function to be:

$$w(p_{T\ MC}) = \left( \frac{dN_e}{dp_T} \right)_{Data} = \frac{p_{T\ MC}}{(p_{T\ MC} + 0.406)^{7.249}} \quad (4.7)$$

The absolute scale is taken arbitrary in this formula as we are only interested in the shape of the input spectrum. Fig. 4.19 shows the comparison of the reconstructed tracks in Simulation weighted with  $w(p_{T\ MC})$  and reconstructed Minimum Bias (not final!) One can see that the shape of reconstructed tracks in the data agrees very well with Monte Carlo.

Matching and eID cut parameters of the Simulations were adjusted in the same way as was done for the data. A comparison of the acceptance in the simulation and real data after applying the full eID cuts is shown in Fig. 4.20 for MB data sample ( $0.5 < p_T < 2.0$  GeV/c) and in Fig. 4.21 for ERT data sample scaled by ERT trigger efficiency ( $1.5 < p_T < 5.0$  GeV/c). The acceptance agrees well in all projections ( $\phi$ ,  $\phi_{EMC}$ ,  $Z$ ,  $Z_{EMC}$ ).



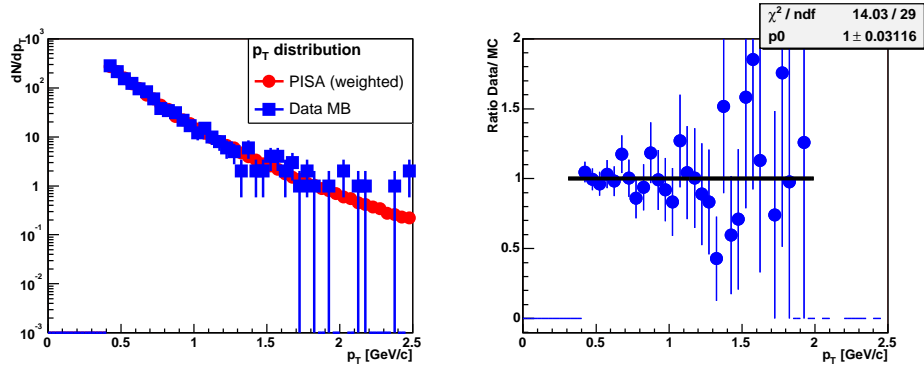


Figure 4.19: Comparison of  $\frac{dN_e}{dp_T}$  distribution for weighted PISA simulation (circles) and MB data (squares). Ratio of  $\frac{dN_e}{dp_T}$  in MB data to simulation (right).

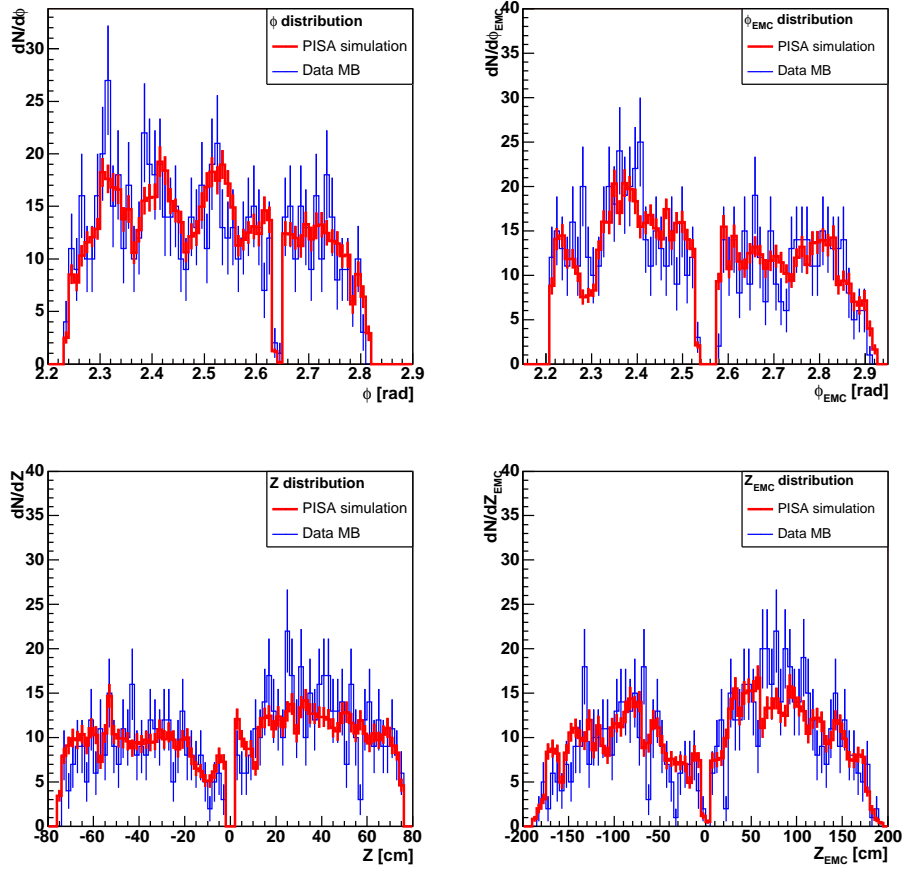


Figure 4.20: Comparison of acceptance in  $\phi$ ,  $\phi_{EMC}$ ,  $Z$ ,  $Z_{EMC}$  for MB data (thin line) and weighted PISA simulation (thick line) for  $0.5 < p_T < 2.0$  GeV/c.

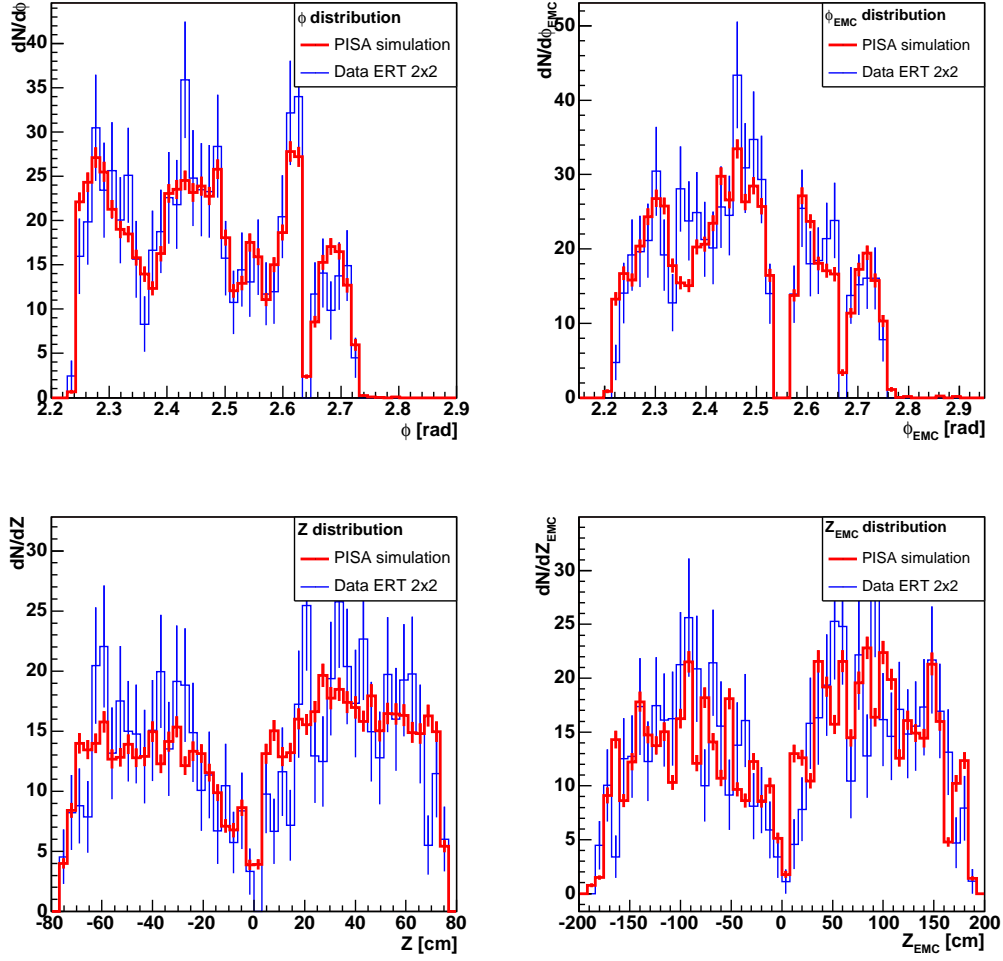


Figure 4.21: Comparison of acceptance in  $\phi$ ,  $\phi_{EMC}$ ,  $Z$ ,  $Z_{EMC}$  for ERT data (thin line) and weighted PISA simulation (thick line) for  $1.5 < p_T < 5.0$  GeV/c.

Now we have everything to calculate the correction function for simulation. By definition of the correction function:

$$\epsilon_{reco}(p_{T \text{ Reco}}) = \frac{\frac{dN}{dp_{T \text{ Reco}}} \cdot w(p_{T \text{ Output}})}{\frac{dN}{dp_{T \text{ Input}}} \cdot w(p_{T \text{ Input}})} \quad (4.8)$$

where the ratio means the ratio of the histograms (for a given  $p_T$  bin) filled with  $\frac{dN}{dp_{T \text{ Output}}} \cdot w(p_{T \text{ Output}})$  and  $\frac{dN}{dp_{T \text{ Reco}}} \cdot w(p_{T \text{ Input}})$  correspondingly.  $p_{T \text{ Input}}$  denotes the transverse momentum of the input EXODUS particle,  $p_{T \text{ Output}}$  is the transverse momentum of the "main contributor" PISA track associated to the reconstructed track with  $p_{T \text{ Reco}}$ . This method of correction function calculation treats the weighting of the input and output distributions correctly.

A rapidity cut of  $|y| < 0.5$  is applied to the input tracks in order to normalize the correction function to one unit of rapidity.

The correction function for the  $e^+ + e^-$  simulation is shown on Fig. 4.22. The points are fitted in a range  $0.4 < p_T < 4.5$  GeV/c with a functional form that well-describes the shape.

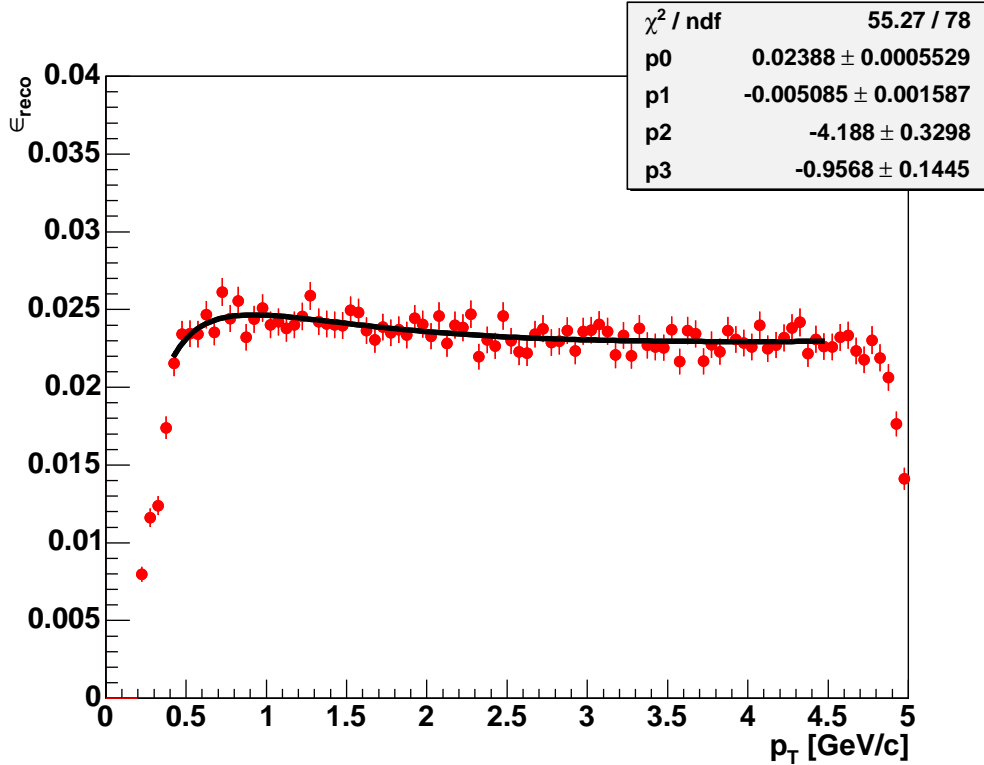


Figure 4.22: Correction function  $\epsilon_{reco}(p_T)$  for  $e^+ + e^-$  (full electron ID cuts).

The correction function indicates that we register  $\approx 2.5\%$  of the simulated particles in our acceptance almost independent on  $p_T$ . The apparent drop of  $\epsilon_{reco}(p_T)$  at  $p_T > 4.8$  GeV/c is non-physical and is caused by the high momentum cut-off  $p_{T\ Input} < 5.0$  GeV/c in the simulated particle sample.

Correction functions for electrons and positrons separately are shown in Fig. 4.23 4.24. The shape of the correction functions for different charges is different because of highly asymmetric acceptance of the TZR counter "shadow" cut (see Fig. 4.1).

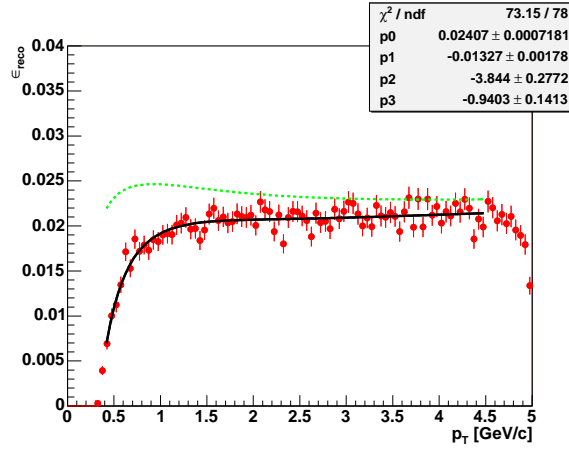


Figure 4.23: Correction function  $\epsilon_{reco}(p_T)$  for  $e^-$ . Total correction function (dashed curve) shown for comparison.

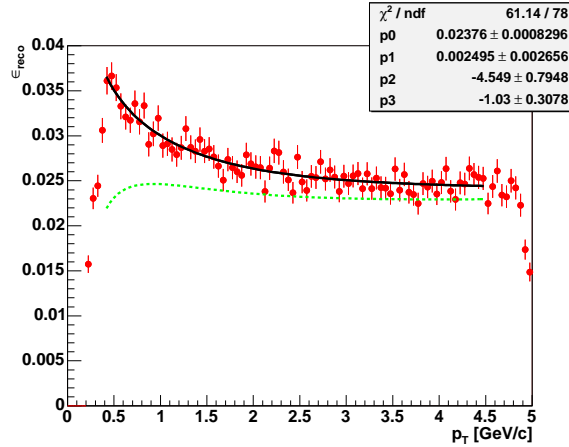


Figure 4.24: Correction function  $\epsilon_{reco}(p_T)$  for  $e^+$ . Total correction function (dashed curve) shown for comparison.

### 4.3.6 BBC Trigger Bias

The remaining unknown in Eq. 4.3 is the **BBC trigger bias**  $\epsilon_{bias}(p_T)$ . “BBC trigger bias” is PHENIX-specific term referring to the probability at which the BBC counter issues a Level 1 trigger decision for an event containing specific particle of interest. The overall BBC efficiency describes the fraction of the total  $p + p$  crosssection registered by the BBC and was measured by Vernier scan to be  $\epsilon_{BBC} = (0.516 \pm 0.031)$  [52]. It is obvious that events with a hard parton scattering are more likely to be registered because the track multiplicity in the BBC is higher for these events. As an example, soft partonic scattering or worse still single- or double-diffractive scattering produce far fewer tracks in the BBC and are more likely to fail in generating a trigger. This means that of all events that contain a hard scattering process, the fraction recorded will be higher than the “inclusive” BBC trigger cross section. The fact that the trigger cross section depends upon the physics process is what we term “Bias”.

$\epsilon_{bias}(p_T)$  was calculated [47] for  $\pi^0$  production using the following technique:

- An unbiased sample of events was selected to be ERT 4x4 trigger with no BBC requirements.
- $\pi^0$  was reconstructed through the  $\pi^0 \rightarrow \gamma + \gamma$  decay in the EMC using the formula  $M_{\gamma\gamma} = 4 \cdot E_1 \cdot E_2 \cdot \sin^2(\theta_{\gamma\gamma}/2)$ .
- The BBC trigger bias was calculated as a ratio of events with BBC vertex information reconstructed to the total number of ERT events.

Fig. 4.25 shows BBC trigger bias as a function of neutral pion  $p_T$ . One can see that the results agree with the value of  $\epsilon_{bias} = (0.75 \pm 0.02)$  independent of  $p_T$  [47] and, as expected, significantly higher than the inclusive BBC efficiency,  $\epsilon_{BBC} = (0.516 \pm 0.031)$ .

This measured value of the constant BBC trigger bias is in good agreement with PYTHIA calculations of the BBC efficiency for hard pQCD partonic scattering processes [52]. Fig. 4.26 shows the PYTHIA simulation results for the BBC trigger efficiency as a function of the collision vertex,  $Z_{vtx}$ , for different physical processes. One can see that the expected efficiency for pQCD hard processes is  $\approx 0.75$  independent on the vertex position. Open Charm production should use this value of trigger bias since any collision process that can generate the charm quark’s mass energy will certainly be a hard process.

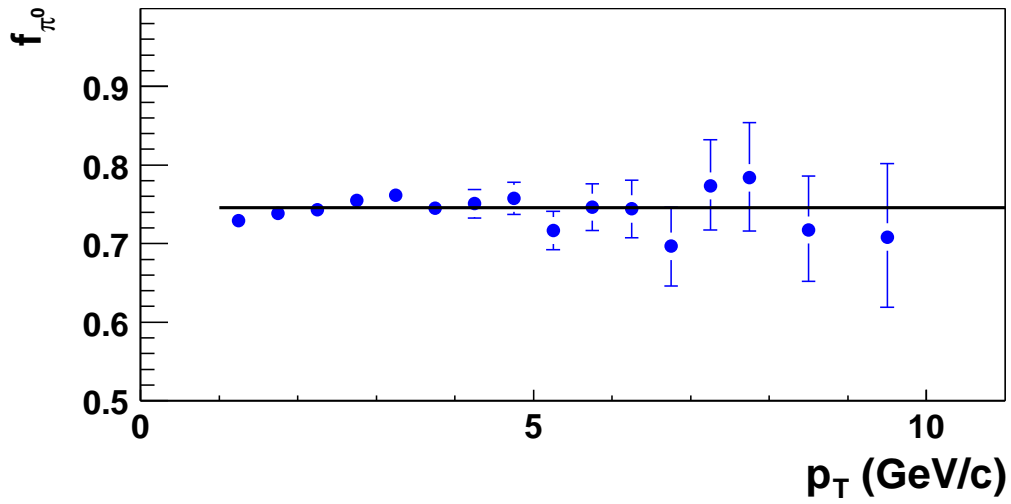


Figure 4.25: BBC trigger bias for neutral pions as a function of  $\pi^0$   $p_T$  with the constant fit to the data [47].

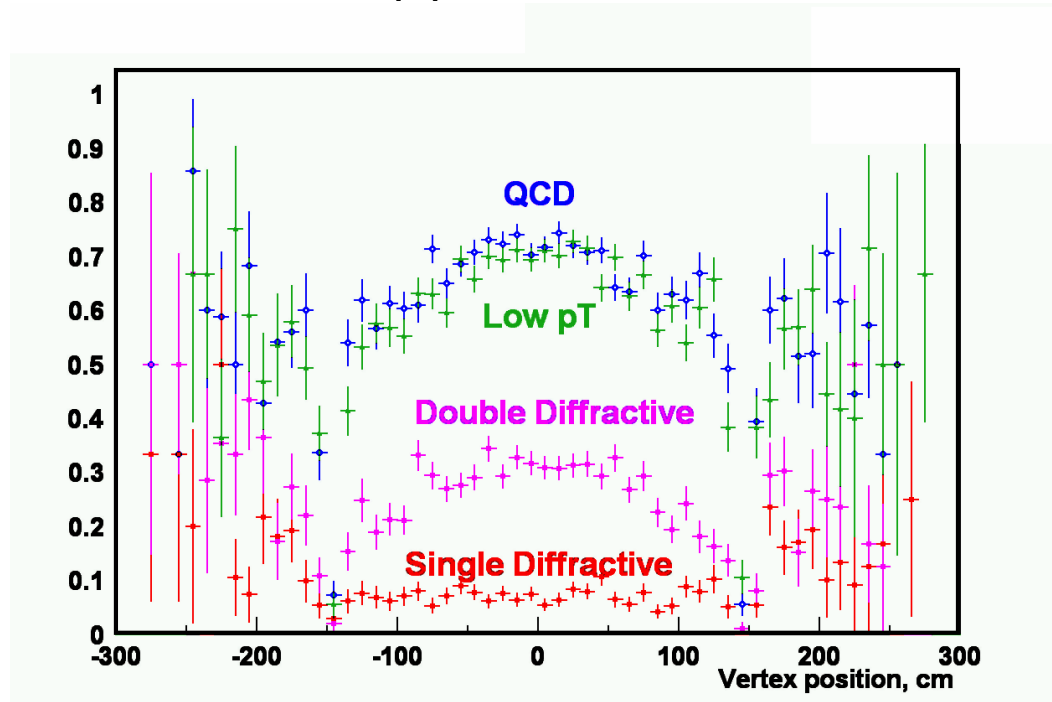


Figure 4.26: PYTHIA+PISA calculations for BBC efficiency as function of  $Z_{vtx}$  for different physical processes.